Fracture Toughness Measurements of Powder Bed EBM Additive and Subtractive (Hybrid) Titanium Alloy Ti6Al4V

Hayrullah Kaan Fero

A thesis

Submitted in partial fulfillment of the

requirements for the degree of

Master of Science in Mechanical Engineering

University of Washington

2022

Committee:

Ramulu Mamidala

John Kramlich

Dan Sanders

Program Authorized to Offer Degree:

Mechanical Engineering

University of Washington

Abstract

Fracture Toughness Measurements of Powder Bed EBM Additive and Subtractive (Hybrid) Titanium Alloy Ti6Al4V

Hayrullah Kaan Fero

Chair of Supervisory Committee:

Dr. Ramulu Mamidala

Department of Mechanical Engineering

Metal additive manufacturing (AM) is a fast growing field of technology, and electron beam melting is one of the few processes capable of producing functional metallic parts. AM method is a layer by layer manufacturing methodology which allows for building of nearly any complicated geometric design. Additionally, additive manufacturing offers customization and has the potential to drastically reduce material waste. However, there are some significant problems that must be addressed for metal additive manufacturing to become more widespread. Ensuring that mechanical performance requirements can be met by EBM-produced parts is essential. The mechanical properties of Ti6Al4V EBM are largely explored under monotonic stress in current metal AM research, with limited research on fracture resistance. Fracture toughness is a key property in damage tolerance and is the primary metric to define the resistance to fracture of a material. To assess the relative impacts of part position, geometry, and proximity on the metal's

fracture toughness properties, a design of experiments technique was used. The radial distance from the center of the build plate, as well as the thickness of the components and height had significant influence on the fracture toughness properties. The maximum results for fracture toughness can be obtained with an increase in height and a decrease in radial distance on the build plate. Even this understanding is crucial in advancing the effectiveness of EBM additive manufacturing for stress-sensitive components in aerospace and beyond. Nonetheless, additional efforts are required to improve the technology to the point where it can be adopted into aerospace manufacturing as a dependable manufacturing process.

Table of Contents

Table of Figures

Table of Tables

Acknowledgements

During my time at University of Washington, I have had the pleasure of working with many smart individuals. My time at University of Washington has help me grow as an individual and I am really proud to be part of this institution. Firstly, this research could not have been done without the support from my wife. In the academic realm, I would like to thank to Melody Mojib and Sayem Bin Abdullah for their supports and help throughout this research. I would not be completed this research without their help. Lastly, I sincerely appreciate all of the mentorship and knowledge that Dr. Ramulu Mamidala has provided for completion of this project.

Dedication

To my wife Burcu, my son Kayra and my niece Derin.

Chapter 1: Introduction

Overview

Metal additive manufacturing (AM) is a rapidly expanding manufacturing technology, and electron beam melting (EBM) using powder stock as the raw material is one of the new techniques capable of making functional metallic products. The aerospace industry is particularly interested in high-strength titanium alloy 6Al-4V (Ti6Al4V) components manufactured by electron beam melting. It is vital to understand the limitations of EBM and to demonstrate that the mechanical properties of EBM-produced parts meet the required design standards [1]. The existing published research on metal AM is mostly concerned with the mechanical properties of Ti6Al4V EBM under monotonic stress. Only a few research studies were found that examine fracture resistance. Material and build orientation, as well as machine settings, all affect the fracture characteristics of AM metals [2]. Additionally, mechanical properties, orientation dependency, and defects all have a significant role in fracture behavior. For the application of metal additive manufacturing to be applied to more highly structural aerospace applications, a better understanding of the metal's fracture toughness will be required.

The shape of the part is crucial for design since it has a substantial impact on the material's and fracture-critical properties. ASTM E399 specifies a suggested thickness for determining a material's plain-strain fracture toughness, K_{Ic}. When the specimen thickness is decreased, the material acts as if it were subjected to plane stress, and the fracture toughness value (K_c) becomes thickness dependent. Apart from the stress field changes caused by decreased thickness, thin parts generated by EBM cool faster and can form martensite microstructures [3].

During the fabrication process, the EBM build space has a temperature gradient with the greatest concentration of heat in the center which can be another key design consideration that can affect the material properties. This makes the location of components on the build plate critical [4]. During the EBM melting and solidification process, sagging can occur. To avoid distortion a part can be supported by the raw powder, a support post in the excess area, or by the build plate. These techniques can affect how heat is evacuated from the part. For example, powder supported parts will cool more slowly than build plate supported parts, and this variation in heat evacuation rate can be a cause for components with distinct microstructures.

The growing emphasis on aerospace applications in additive manufacturing necessitates a deeper understanding of the fracture toughness properties of Ti-6Al-4V. As previously stated, little data on the fracture toughness of metals generated using EBM have been recorded.

One of the most pressing challenges is to gain a better understanding of how to use post-build thermal heat treatment processing techniques to improve fracture characteristics and surface quality. As a result, the following study analyzes the impacts of part position, size, and the interaction of these parameters on the fracture toughness of EBM Ti-6Al-4V, as well as several post-processing techniques to increase fracture resistance.

Objectives

The objectives of this research are:

1. Building the 3-, 6- and 9-mm Compact Specimens (CT) according to the ASTM E399 standards with different radial distances and heights in the build chamber by utilizing ARCAM A2X Electron Beam Melting machine (54 CT specimens total).
2. Remove 0.325 mm from each surface of the 6- and 9-mm CT specimens and 0.2 mm from each surfaces of 3mm CT specimens by utilizing CNC-Mill and collect forces by using a dynamometer.
3. Measure the surface roughness of all 54 specimens.
4. Heat treating 27 of the CT specimens in the furnace at 550 C for 2 hours.
5. Polish the heat-treated specimens and measure the surface roughness.
6. Experimentally test the fracture toughness of 3-, 6- and 9-mm CT specimens that were built with different radial distances and heights.
7. Analyze the data and show trends.

Chapter 2: Background and Literature Review

Additive Manufacturing

Additive manufacturing is defined by ASTM as a process of joining materials to make objects from 3D model data, usually layer upon layer, as contrast to subtractive manufacturing approaches. All kinds of materials, including metals, ceramics, polymers, composites, and biological systems, are included by this definition [5]. While AM has arguably been around for over three decades as a technique of treating materials, it has just lately begun to emerge as a significant commercial manufacturing technology. The recent surge in interest and investment in AM technologies is not surprising, as this layer-by-layer powder melting additive process is an elegant concept that can create complicated shapes from a range of materials. In terms of industrial machinery, assembly processes, and supply chains, AM technologies have the potential to have a considerable impact on existing manufacturing models. Many companies are engaging in research to commercialize metal-based AM technologies for remanufacturing of worn or damaged parts. These technologies can help to simplify the manufacturing value chain by removing the need for third-party suppliers, improving performance, and extending the product's useful life [6].

Traditionally, AM is recognized as a method for fusing plastics, however industry has recognized that this process can be applied to metal alloys such as Ti-6Al-4V. The powder bed fusion technique is the most common AM method used in the industry to utilize titanium to create functional parts. It uses either a laser or an electron beam to melt and fuse material powder together. Titanium is known for superior mechanical properties such as strength to weight ratio, fracture toughness, biocompatibility, corrosive resistance, and creep resistance.

Machining titanium with traditional manufacturing methods is time consuming and expensive process due to multiple parameters based on the energy required for high cutting forces, specialty, and replacement tools necessary for tool life and adequate cooling based on heat generated. Based on raw material costs, machining time required and significant base thermal properties, conventional machining of titanium costs more than conventional machining of steel or aluminum [7]. Therefore, additively manufactured titanium parts could provide industry a viable option to reduce the cost of machined components that lasts longer than steel or aluminum.

Benefits and Barriers of Additive Manufacturing

AM methods are distinguished by their individual layering methodology, which allows for the building of very complicated geometric design. In contrast, subtractive methods limit design freedom owing to the requirement for cutting tool geometry, fixturing, different equipment characteristics, the danger of part to spindle collisions, and the difficulties of the cutters to reach deep and unseen zones when creating complicated shapes. Current AM technologies give designers the most creative freedom when it comes to creating complicated geometric designs. When utilizing AM, this complexity comes at very little additional expense since there is no requirement for extra equipment, re-fixturing, greater operator experience, or even fabrication time. Manufacturing via AM technologies allows for the fabrication of complex geometrical shapes that would otherwise necessitate the assembly of several pieces if manufactured traditionally [6].

One of the main barriers to the progress of AM in industry has been the cost. AM is viable for low volume and high geometric complexity parts but the relative cost for mass manufacturing

of a standardized part geometry using AM is significantly larger than injection molding due to the discrepancy in cycle time, which is slow in comparison to other processes. Another key issue is the resolution of the printed parts. A higher layer resolution will provide a better surface finish, but it greatly increases the total build time as more layers are needed to create the desired geometry. Furthermore, AM is currently limited to a certain number of materials. Because of the interlayer bonding deficiencies, AM systems suffer from anisotropic mechanical properties [6]. Lastly and most importantly, AM processes need standardization to ensure part quality, repeatability, and consistency across builds. It is crucial that AM industries develop more materials and improve the process, calibration and testing but the variety of the machines and processes make the development of a uniform standard challenging

Electron Beam Melting

Electron Beam Melting (EBM) additive manufacturing is a patented technology by Arcam® AB (now a part of GE Additive). This technology uses thermal energy to selectively consolidate the metal powder into a metal part. The energy source is an electron beam that heats and starts phase change of the metal powder under vacuum.

Principle of Operation

The electron beam is generated using a wire filament in a glass bulb and the system has 3 coils that manipulate the beam. The chamber is maintained at high vacuum 10^{-4} millibar and temperature around 700 $^{\circ}$C. Printing of parts is achieved layer by layer, in which powder is swept across the build plate or the recently printed layer by a rake. The electron beam sinters the whole build layer and performs selective melting and consolidation of the specific regions of interest and this process continues until the whole part is printed.

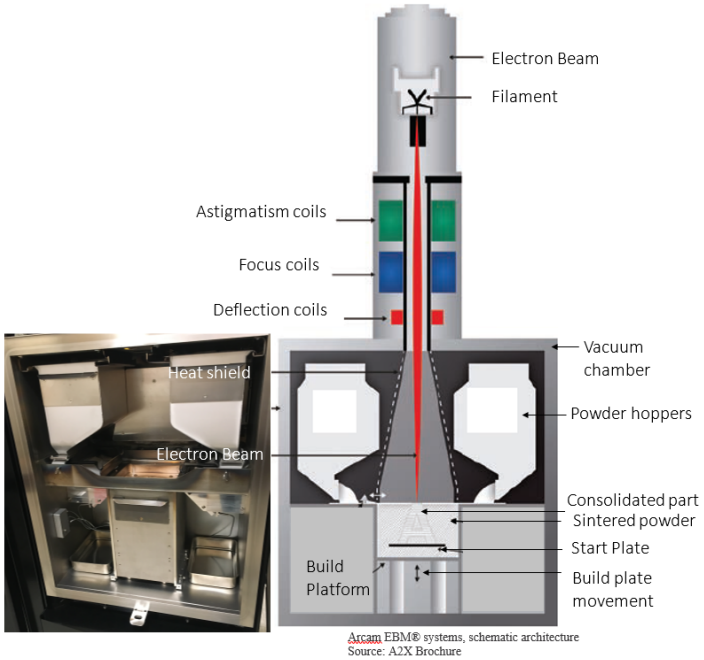

Figure 1: Schematic representation of the Arcam A2X

The Arcam A2X EBM additive manufacturing equipment is shown in Figure 1. The control and build chambers are where process parameters are defined, and printing occurs. Lanthanum hexaboride filament is employed in this system and has an estimated life of around 100 hours. One significant drawback of the EBM is the short life of the filament due to its long process time. Two production runs of 40 hours with one filament is a major issue.

Figure 2: Key components in Arcam A2X 3D Metal printer

Table 1: Technical specifications provided by the manufacturer.

Parameter/Response/Feature	
Build tank volume	250 x 250 x 400 mm (W/D/H)
Actual build envelope	200 x 200 x 380 mm (W/D/H)
Model-to-Part accuracy, long range	+/- 0.20 mm (3σ)
Model-to-Part accuracy, short range	+/- 0.13 mm (3σ)
Surface finish (vertical & horizontal)	Ra= 25 µm / 35 µm
Beam Power	50–3000 W (continuously variable)
Beam spot size (FWHM)	0.2 mm – 1.0 mm (continuously variable)
EB scan speed	up to 8000 m/s
Build rate	55/80 cm^3/h (Ti6Al4V)
No. Of Beam spots	up to ~100
Vacuum base pressure	$<1x10^{-4}$mbar

Other important build parameters used for printing in this project are listed in Table 2.

Table 2: Build parameters as defined in melt theme

Melt theme	
Beam Speed	4530 mm/s
Beam Current	15 mA
Max current	20 mA
Focus offset	25 mA
Speed function	45
Snake	True
Line order	1
Line offset	0.2 mm
Randomized hatch	False
Hatch depth	0.05 mm
Speed factor	1.5 mm
Thickness factor	0 mm
Exponent factor	0.5 1/mm

Once the part is printed and the temperature reaches the notification level (corresponding to a safe level for operator access), the build is extracted. Powder that is not integral to the built part is recovered from the surrounding sintered block of partially sintered powder and from the build envelope using vacuum cleaners. The Powder Recovery System (PRS) separates the fines (particles <45 μm) and any metallic foreign impurities. The powder is then sifted using a vibratory (Russell) sieve to separate the impurities and lumps of sintered powder.

Raw Material

In this investigation, Ti6Al4V powder was obtained from a General Electric (GE) company subsidiary Advanced Powders & Coatings (AP&C). The chemical composition of the fresh unused powder, as provided by the manufacturer, along with the permissible limits are

listed in Table 3. The powder is delivered in sealed canisters labeled with batch number and the associated technical specification sheet. 100 kg of powder was obtained for this study.

Table 3: Technical specifications provided by the manufacturer.

Element	Required		Measured	Testing method
	ASTM F2924	**UAC065-170510**		
Carbon (C)	< 0.08	< 0.08	0.02	ASTM E1941
Oxygen (O)	< 0.20	0.11-0.20	0.14	ASTM E1409
Nitrogen (N)	< 0.05	< 0.05	0.02	ASTM E1409
Hydrogen (H)	< 0.015	< 0.015	0.002	ASTM E1447
Iron (Fe)	< 0.30	< 0.30	0.20	ASTM E2371
Aluminum (Al)	5.50-6.75	6-6.75	6.37	ASTM E2371
Vanadium (V)	3.50-4.50	3.50-4.50	4.01	ASTM E2371
Yttrium (Y)	< 0.005	< 0.005	< 0.001	ASTM E2371
Others	< 0.40	< 0.40	< 0.40	ASTM E2371
Titanium (Ti)	Balance	Balance	Balance	ASTM E2371

Figure 3a and 3b show the SEM micrograph and particle size distribution (count %) of the virgin powder, corresponding to Batch P1143 The powder distribution (mass %) reported by Arcam is listed in Table 4. More than 90% of the particles were in the range of 45-106 µm. In addition, the flow rate reported according to ASTM B213 is 26 sec/50g with a maximum permissible limit of 29 sec/50g. The apparent and tap density was 2.49 g/cc and 2.8 g/cc as per ASTM B212 and ASTM B527 respectively. The minimum required values for apparent density and tap density are 2.4 and 2.7 g/cc respectively.

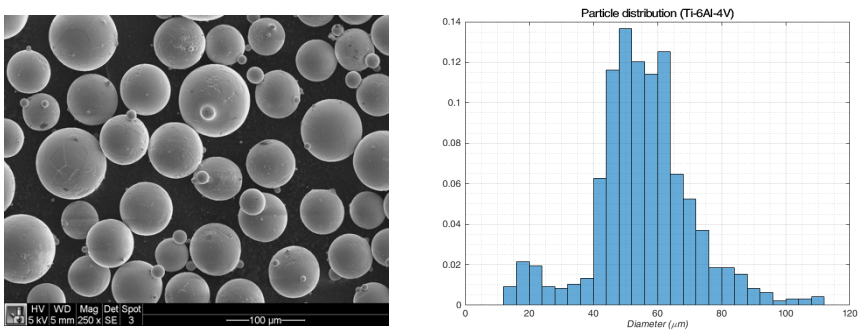

(a) (b)

Figure 3: Details of the Ti6Al4V powder obtained from AP&C for this program. (a) SEM micrograph of virgin powder, (b) Particle size distribution

Table 4: Powder size distribution (Batch P1143) as measured per ASTM B214

Particle size	Required	Measured
< 25 µm	< 0.7	0.0
25-45 µm	Report	3.8
45-106 µm	> 90	94
106-150 µm	Report	2.2
> 150 µm	< 0.2	0.0
< 45 µm	< 5.0	3.8
> 106 µm	< 5.0	2.2

Fracture Mechanics

Typically, the word "fracture toughness" refers to a property of a material's resistance to crack growth. Experimental determination and standardization of fracture toughness are critical for applying fracture mechanics methods to structural integrity assessment, damage tolerance design, fitness-for-service evaluation, residual stress analysis of individual engineering components and structural assemblies. Additionally, the fracture toughness values may be used

to characterize, evaluate, and ensure the quality of commercial engineering structures, such as nuclear pressure vessels and pipes, petrochemical vessels and tanks, oil and gas pipelines, car, ship, and aircraft structures. Thus, testing and evaluating fracture toughness has been a critical aspect of the development of the fracture mechanics approach and its engineering applications [8]. Since many industries hold a significant interest in high strength titanium alloys (Ti6AL4V), it is critical to understand the limitations of EBM and to demonstrate that the mechanical properties of parts produced with EBM match the design requirements.

Limited published work was found on resistance to fracture for metal additive manufacturing that is focused on process variability vs. material property characterization. Seifi et al suggested that changes in the microstructure, texture, and flaws due to orientation contribute to part of the tensile property differences but become more significant for fracture-critical parameters. Post-processing such as HIP or peening can be used to create more acceptable microstructures and decrease or remove process-induced flaws. However, isolated internal porosity that remains after HIP can have a negative impact on the part life. Additionally, most published fracture data on EBM reported K_Q values since the thickness criteria for valid fracture toughness measurements are not satisfied in Ti6Al4V EBM, and there are only a few published studies that offer legitimate K_{Ic} (plane-strain) measurements. This limits direct comparisons of toughness values between distinct works due to the inflated toughness values caused by the plane stress conditions [2].

One of the significant published studies worked on determining the orientation dependence of fracture toughness values [9]. Figure 4 below illustrates the specimen build orientation according to the ARCAM build plate that was used. There are 5 different orientations and directions considered in this study. L denotes as longitudinal, S denotes as short and T

denotes as transverse. All tested samples reported K_Q values due to the violated ASTM thickness criteria for valid K_{Ic}. Obtained fracture toughness values from this study are shown in Table 5 [9].

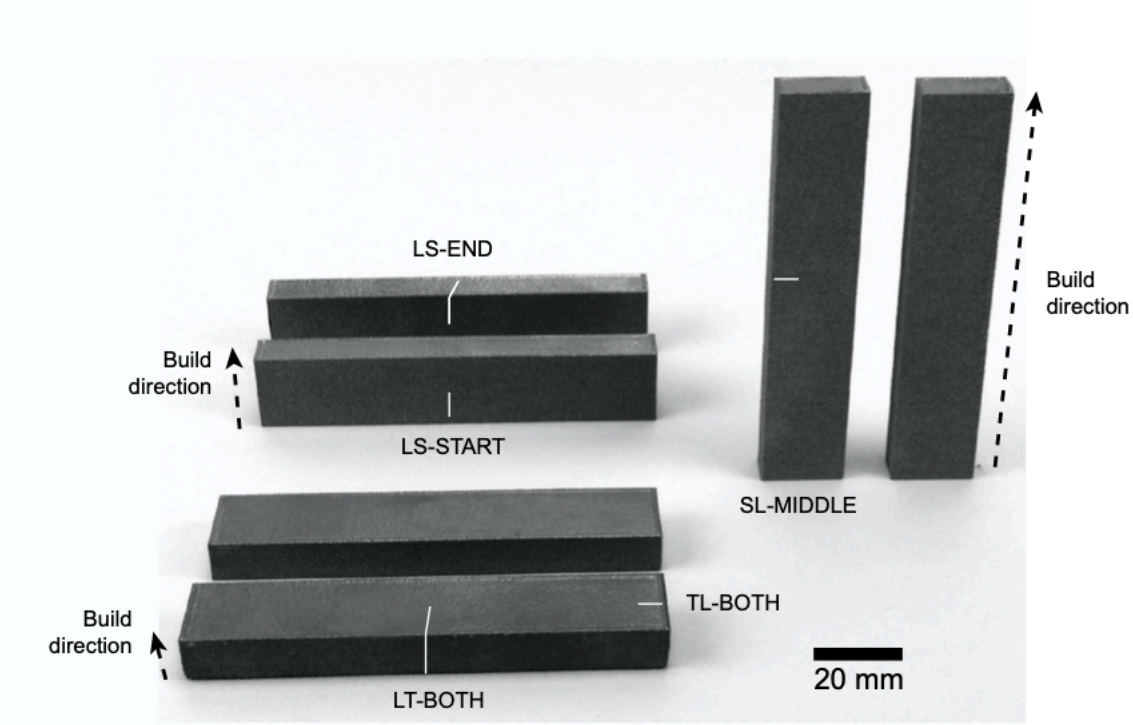

Figure 4: Specimen's orientations illustrating crack growth directions with respect to the build direction. Initial notches shown in white [9]

Table 5: Summary of fracture toughness results for orientations [9]

Specimen orientation	Thickness, B (mm)	Span, S (mm)	Fracture toughness K_q (MPa √m)
LT-BOTH	9	40*	68, 80
LS-END	10	40*	76
TL-BOTH	9	18*	67
SL-MIDDLE	10	80	65

Additionally, Edwards et al. achieved fracture toughness values for compact specimens that were built horizontally and vertically using EBM [10]. The findings revealed that the fracture toughness values were superior to those of annealed Ti6Al4V. Due to a failed specimen geometry validity check, apparent fracture toughness is provided instead of K_{ic}, as indicated in Table 6. To acquire reliable K_{ic} values, the prior study suggests using thicker specimens.

Table 6: Summary of fracture toughness results [10]

	Kq (MPa√m)	
Orientation	**Ave**	**Stdev**
Horizontal	110	8.9
Vertical	102	7.4

Chapter 3: Experimental Methods

Experimental Design

This testing was carried out to assess the impact of component thickness and position within the build chamber on the fracture resistance of EBM Ti6Al4V. A multi-factor design approach was used to create the compact tension (CT) specimens, which included three different levels of thickness, height, and radial distance as shown schematically in Figure 5. Three different levels of thickness were chosen to investigate the plane-strain condition according to ASTM E399. The two location factors addressed in this study are radial distance and height. Table 7 shows the three factor levels for the fracture toughness DOE. The use of a three-level factorial design in this study allows for the use of polynomial regressions to investigate the many combinations and interactions that affect fracture toughness.

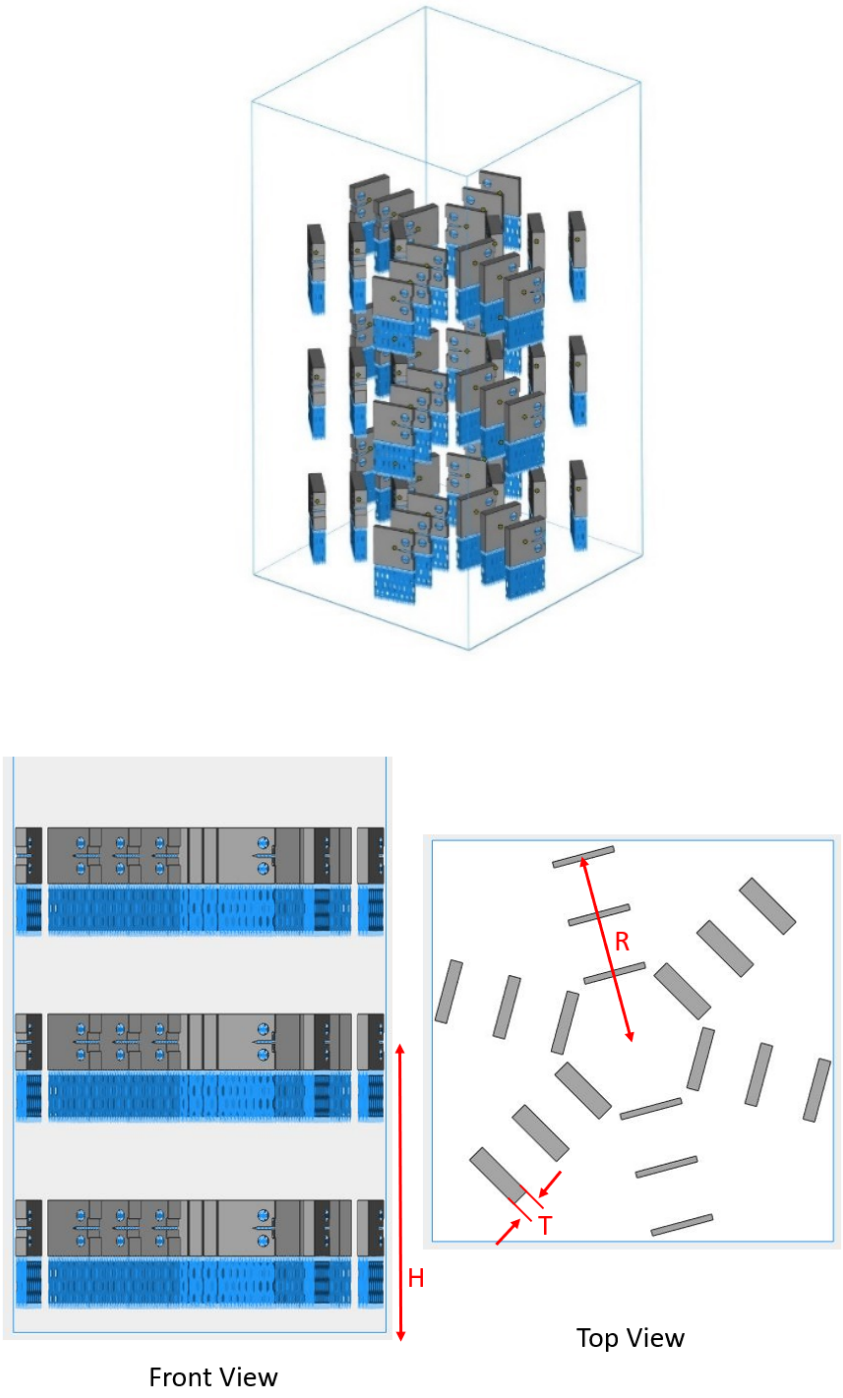

.

Figure 5: Fracture Toughness Build Layout. Shown are the oblique, front and top views, respectively.

The specimens used in this study were printed with recycled Grade 5 Titanium alloy (Ti6Al4V), which was obtained from the EBM machine manufacturer (ARCAM: Batch P1143, Part #430944). The original build began with 100 kg of fresh unused powder, which was recycled using the Arcam Powder Recovery System (PRS), sieved, and mixed with the powder left in the hoppers. Table 2 of Chapter 2 lists the build parameters for the melt theme. To explore the impact of part geometry and location on material properties, the default suggested machine parameters for Ti6Al4V were employed.

As shown in Table 8, a total of 54 compact tension (CT) specimens were printed, with six specimens of the same thickness at each level of height and two for each radial position. Figure 6 depicts the dimensions of the CT specimens, with varying thickness values as specified in Table 7. To analyze the fracture growth behavior along the beam scan route, all specimens were produced vertically with the crack plane perpendicular to the build direction with the intended crack surface oriented parallel to the build plate. The specimens were given three letters to provide orientation indication, according to ASTM E399 [11]. Since all the specimens were built vertically with the crack plane perpendicular to the build direction, the three letter orientation identification scheme was not used in this study. T means thickness, R denotes radial distance, and H denotes height in this work. The radial distance is the distance between the build space's central axis and the specimen's center. The height describes the height from the build plate at which the specimens' centers were created. Following the printing procedure, all of the specimens were machined in the manner described in the following section. A naming convention was followed to identify each specimen by thickness, height and radial distance and it is illustrated in Table 9.

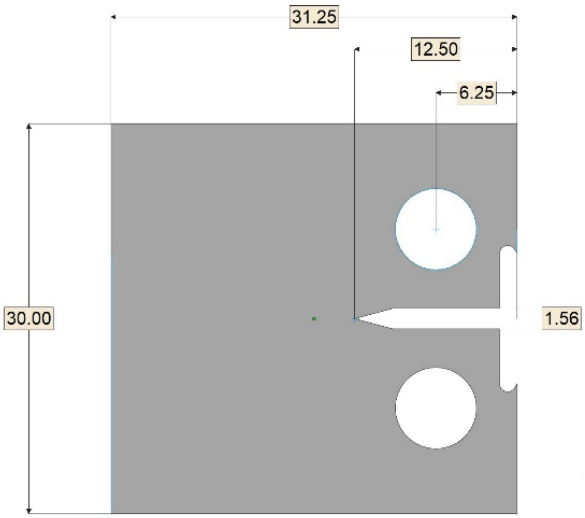

Figure 6: ASTM E399 CT fracture toughness specimen size, units in mm

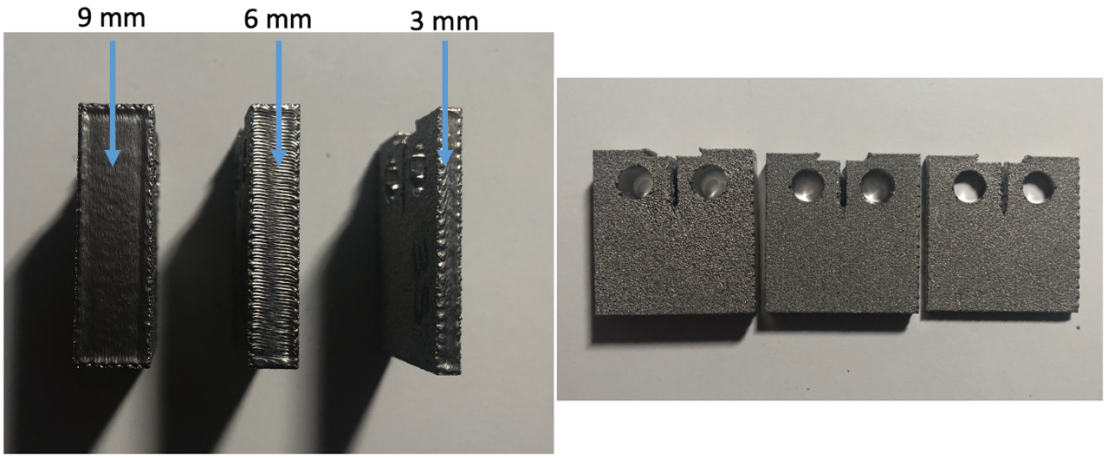

Figure 7: As Build Compact Tension Specimens

Table 7: Overview of Fracture Toughness specimen size and location

Specimen Summary	
Thickness (T, mm)	3, 6, 9
Radial Distance (R, mm)	35, 65, 95
Height (H, mm)	56, 156, 256

Table 8: Summary of number of specimens for each designation

Each Thickness	18
Each Radial Distance	18
Each Height	18
Total	54

Table 9: Summary of specimen naming convention

Specimen Identification Code	Thickness (mm)	Height (mm)	Radial Distance (mm)
3_56_35	3	56	35
6_156_65	6	156	65
9_256_95	9	256	95

Machining (Milling), Cutting Forces and Tool Wear

Following the printing process, all specimens were machined to reduce surface roughness and its potentially bad influence on fracture toughness test results. A CNC-Mill (Haas) was used to machine all 54 specimens of varying heights, radial distances, and thicknesses. The milling procedure was performed on the specimen's largest face, where the crack would propagate. Additionally, machining was performed parallel to the crack direction. Machining operation was accomplished dry and no additional cutting fluid was utilized. A certain quantity of material was removed from each layer to ensure that the plane strain criteria are still met while the roughness of the outside is minimized. For the specimens that were 6 and 9 mm thick, roughly 0.325 mm of material was removed from each surface, resulting in a 0.65 mm drop from the printed

dimension. In addition, 0.20 mm of material was removed from each surface of the 3 mm thick specimens, resulting in a 0.40 mm material removal from the printed dimension. Table 10 shows the final thicknesses of the specimens. Milling operations were performed with titanium-specific cutting process settings, as shown in Table 11. Additionally, cutting forces were gathered using a Kistler 9123 dynamometer to determine the amount of force imparted to the specimen in the x, y, and z directions during milling. Lastly, an optical microscope was utilized to demonstrate the tool wear on the carbide end mill.

Figure 8: Haas CNC mill: spindle shown cutting a CT specimen

Table 10: Overview of Fracture Toughness specimen size

Specimen Thickness	
As Build (mm)	After Machining (mm)
3	2.60
6	5.35
9	8.35

Table 11: Machining Parameters

Cutting Tool	Carbide End Mill
Tool Diameter (in)	0.5
Cutting Speed (in/min)	3
Spindle Speed (rpm)	500

Figure 9: Kistler 9123 dynamometer

Heat Treatment

Half of the 54 machined specimens were subjected to heat treatment in order to eliminate residual stresses caused by the machining process and examine the impact of heat treating on the resistance to crack formation. Heat treatment was carried out in a furnace (Nabertherm) at 550 C for 2 hours, and the samples were cooled in argon for 24 hours to limit microstructural change during cooling. The specimens were then polished with a 600-grit sandpaper to eliminate any oxidation that had built up on their surfaces after cooling.

Figure 10: Inside view of Nabertherm Furnace

Surface Roughness

Contact type profilometer MarSurf XR20 was utilized to obtain the surface quality of the machined and machined+HT specimens before fracture toughness testing. The XR20 is equipped with a 2.5µm conical diamond tip with a 5nm resolution. Surface roughness measurements were collected perpendicular to the crack direction.

Fracture Toughness Testing

Fracture toughness tests are performed to quantify the resistance of a material to failure by cracking. To determine fracture toughness qualities, the specimens were evaluated in machined and machined+HT states.

The apparent fracture toughness was determined using the plane-strain method as per ASTM 399. To carry out the test, Instron Model 8511 universal testing machine with a capacity of 20 kN were utilized. All tests were carried out in a quasi-static linear-elastic state. The specimens were produced utilizing straight-through wide notch compact tension (CT) specimens in

accordance with ASTM E399. To ensure that specimen thicknesses conformed to the ASTM E399 geometry limits, equation 1 was utilized.

Following that, a sharp pre-crack is formed from the existing notch using cyclic loading at a frequency of 10 Hz and a stress ratio of 0.1, as specified by ASTM E399. The fatigue pre-cracking load was computed using Ti6Al4V plane-strain fracture toughness data from the literature [16]. To guarantee the material performs linear-elastically during testing, a fatigue pre-crack length of about 12-mm was produced as specified by Equation 2 [11]. The fracture toughness tests were carried out under tension at a constant rate of 0.08 kN/s for 3mm thick specimens and 0.15 kN/s for 6- and 9-mm specimens. The crack mouth opening displacement (CMOD) was monitored and recorded using a displacement gauge, as indicated in Figure 2.4's load-displacement curves. All testing was conducted at room temperature. The specimens were subjected to increasing ΔK conditions until total breakage occurred.

$$2 < \frac{W}{B} < 4 \tag{1}$$

$$0.45W \leq a \leq 0.55W \tag{2}$$

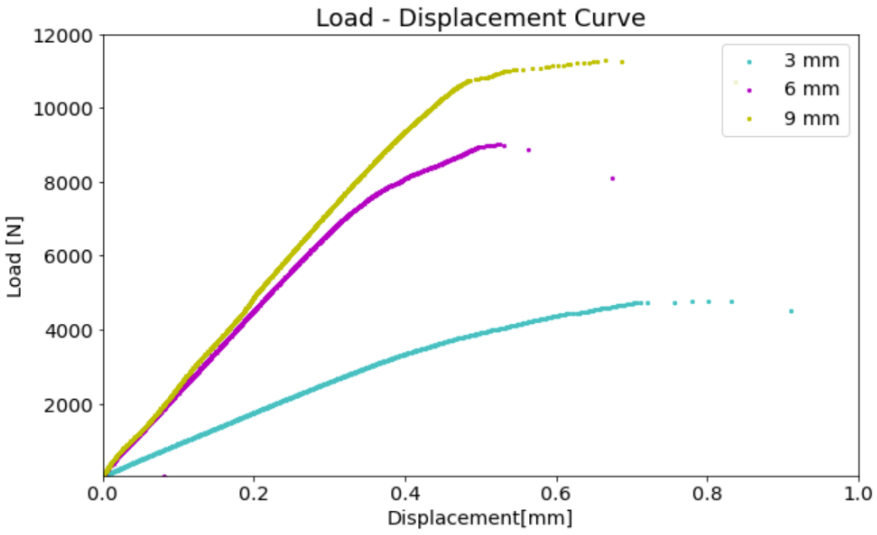

Figure 11: ASTM E399 CT fracture toughness specimen size, units in mm

Following the conclusion of the test, the conditional fracture toughness KQ is calculated as follows. The force at a 5% secant offset (PQ) is calculated using the initial linear slope of the recorded applied load and CMOD. Three samples of load displacement curves are illustrated in Figure 12 for each thickness with linear slope and 5% secant offset drawn. Equation 3 is used to compute the conditional fracture toughness K_q from the value of P_q, where P is the applied load, a is the crack size, W is the frontal width, B is the thickness and f(a/W) is the size correction factor [11].

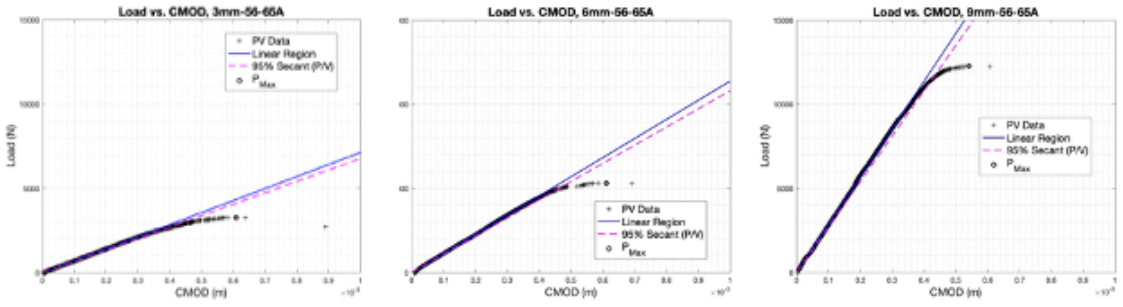

Figure 12: Load vs CMOD for various thicknesses

$$K = \frac{P}{B\sqrt{W}} f\left(\frac{a}{W}\right) \tag{3}$$

$$f\left(\frac{a}{W}\right) = \frac{(2+\frac{a}{W})\left[0.886+ 4.64\frac{a}{W}-13.32\left(\frac{a}{W}\right)^2+14.72\left(\frac{a}{W}\right)^3 - 5.6\left(\frac{a}{W}\right)^4\right]}{(1-\frac{a}{W})^{3/2}} \tag{4}$$

According to the ASTM E399 standard, two distinct equations must be utilized to verify that each test meets the plane-strain criteria. The fracture toughness values are validated using Equations 5 and 6 [11]. If both validity equations are satisfied, the stress intensity value K_Q can be given to the material property KIc, indicating that the plane-strain condition is satisfied, and the test is valid.

$$\frac{P_{max}}{P_Q} \leq 1.10 \tag{5}$$

$$W - a \geq 2.5 \left(\frac{K_Q}{\sigma_{ys}}\right)^2 \tag{6}$$

Additionally, because the 3 mm specimens did not fulfill the ASTM E399 thickness criteria, they were analyzed using the ASTM E561 R-curve technique [13]. Using Equation 7, normalized compliance was calculated by utilizing CT specimen geometry and effective crack size [13]. After that, normalized crack size was calculated from the normalized compliance in the CT specimen by utilizing Equations 8 and 9 [13]. A plot of compliance calibration curve was established and then K_R curve was plotted in terms of effective crack extension [13]. The critical stress intensity K_c is measured at the point at which unstable crack propagation begins and the slope becomes flat, or at tangency, as illustrated in Figure 13. This K_c value is reliant on the form of the curve, as well

as the size and geometry of the specimen fracture, and hence cannot be regarded a material property. he previously determined K_{Ic} values, on the other hand, are not reliant on the thickness or size of the fracture and are thus regarded as a material property.

$$EB\frac{\Delta v}{\Delta P} = 120.7 - 1065.3\left(\frac{a}{W}\right) + 4098\left(\frac{a}{W}\right)^2 - 6688\left(\frac{a}{W}\right)^3 + 4450.5\left(\frac{a}{W}\right)^4 \quad (7)$$

$$\frac{a}{W} = 1.001 - 4.6695\,U + 18.46\,U^2 - 236.82\,U^3 + 1214.9\,U^4 - 2143.6\,U^5 \quad (8)$$

(9)

$$U = \frac{1}{1 + \sqrt{EB\frac{\Delta v}{\Delta P}}}$$

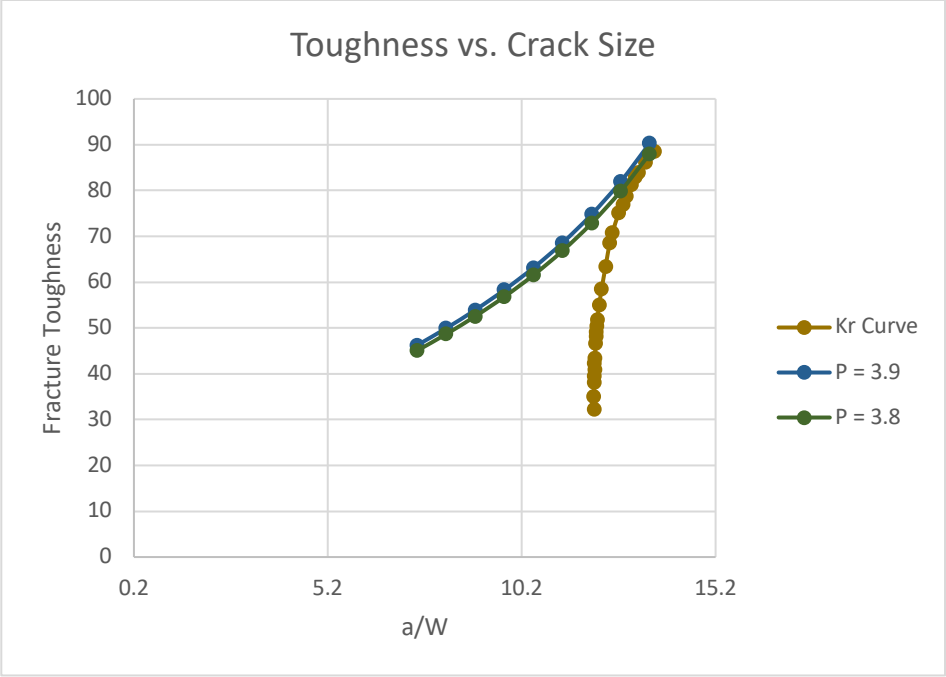

Figure 13: K_R (yellow) and driving force curves (blue & green) for a select 3mm specimen

Because it is critical to understand the effects of surface roughness and post-processing treatments on the fracture behavior of EBM-created parts, 27 specimens were fracture tested immediately after CNC-Milling. The remaining 27 specimens were CNC-Milled, heat treated, polished, and fracture tested. As previously indicated, all calculations for 3, 6, and 9mm specimens were tested under the plane-strain condition following ASTM E399. Additionally, due to the invalid thickness, calculations on 3mm specimens were also performed under plane-stress circumstances according to ASTM E561.

Fractography

Olympus SC30 optical microscope and Olympus SZX16 stereo microscope were used to observe the fracture surface, confirm the crack length prior to fracture and identify mechanisms associated with crack growth. The overall fracture surface and determination of crack length was performed using the optical microscope.

Internal Defect Analysis

Internal defect analysis was carried out by another member of the University of Washington's EBM research team to support this effort. Defect distributions of select fracture toughness specimens were obtained prior to testing using an X-ray Computed Microtomography (µCT) using a commercial system (X5000, North Star Imaging, Rogers, MN, USA). Two of the 6 and 9mm specimens and four of the 3 mm specimens were scanned at a time to reduce scan time, and cost without compromising resolution, and the parameters adjusted based on the thickness of the specimens, as shown in Table 12. With an increase in thickness, the voltage was increased to increase penetration of the x-ray through the specimens. In addition, only the area ahead of the crack tip was scanned to reduce scan time. The scans were reconstructed using the

manufacturer's commercial software (efX CT), which exports the scanned volume as a stack of TIFF images. The images are then imported into VGStudio MAX (Volume Graphics Inc., Charlotte, NC, USA) for evaluation.

Table 12: Scan Parameters using for 3, 6 and 9 mm specimens

Scan Parameter	3 mm	6 mm	9 mm
Voltage	210 kV	210 kV	210 kV
Current	85 µA	80 µA	90 µA
Geometric Zoom	x11.67	x11.67	x11.67
Projections	2400	2400	2400
Frame Average	2	2	2
Frames per second	2	2	
Gain Maps	7	7	7
Resolution	17.85 µm	16.75 µm	15.44 µm
Filter	.005 in brass	.005 in brass	.005 in brass

Hardness

Following fracture toughness testing, Vickers microhardness of select machined and machined+HT treated specimens were obtained using a commercial micro- indenter (LM247AT, LECO Corp, MI, USA) per ASTM E92 [4]. Hardness testing was carried out by another member of the University of Washington's EBM research team. The average hardness of the 9 mm specimens that were built in various locations within the build chamber was derived from seven (7) different indentations. For each indentation, a 500 gf was applied for a duration of 13 seconds in the vertical, horizontal, and diagonal directions. Per the ASTM E92 requirement, a minimum distance of 2.5 times the indentation diagonal was maintained between each indent. During the hardness

measurement process, each indent was verified for accuracy and non-compliant indents were omitted from the average hardness calculation.

Chapter 4: Results

Surface roughness

Prior to fracture testing, the surface roughness of all machined and machined+HT specimens were measured. To better understand the influence of surface roughness on crack growth, the average surface roughness (Ra) and ten-point height (Rz) were measured in the area perpendicular to the fracture plane. Figures 13 and 14 show the surface profile of the machined and machined+HT specimens and Table 13 contains a summary of the values. With machining, the surface roughness, Ra values of the surface perpendicular to the fracture route, were considerably reduced. Furthermore, owing to oxidation, machined+HT specimens were polished with 600-grit sandpaper after the heat treatment, resulting in a superior surface quality than only machined specimens. The percent difference between the machined and machined+HT specimens was found to be 38.8 %. The impacts of the rough surface exterior on fracture toughness were mitigated when surface roughness was reduced.

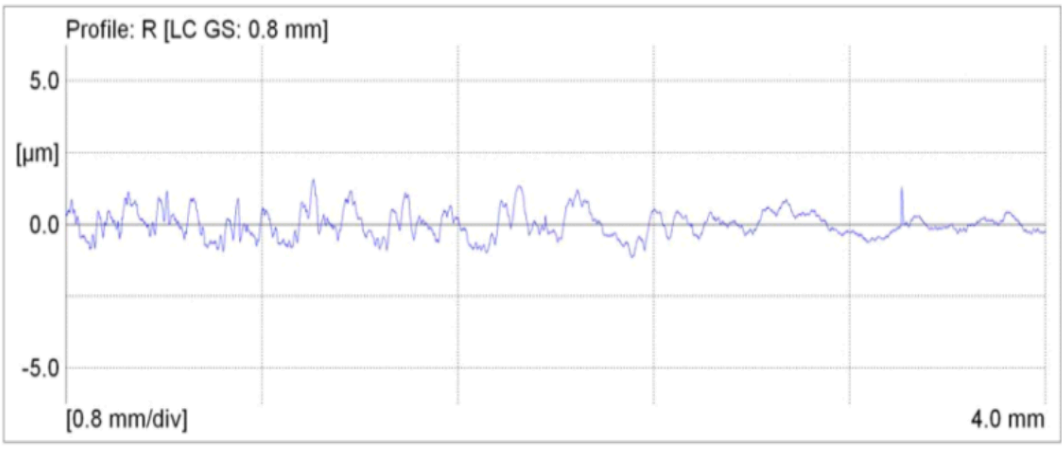

Figure 14: Surface profile of machined specimen (6mm thick, 256mm heigh, 95mm radial distance)

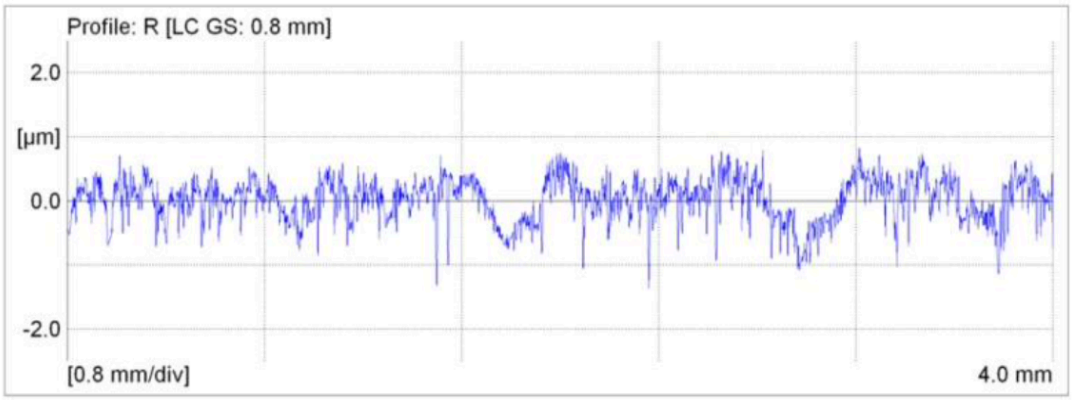

Figure 15: Surface profile of machined+HT specimen (6mm thick, 256mm heigh, 95mm radial distance)

Table 13: Summary of surface roughness of machined & machined+HT specimens

Machined R_a (µm)	Machined R_z (µm)	Machined+HT R_a (µm)	Machined+HT R_z (µm)
0.4 ± 0.11	2.4 ± 0.94	0.27±0.12	2.1±1.2

Force Analysis and Tool Wear

Cutting forces are used to describe the mechanical stresses that the cutting edge and the workpiece endure. These pressures grow when the tool's sharp cutting edge wears down and the material on the workpiece clings to the cutting edge, generating a built-up edge. Tool wear and the creation of a built-up edge result in a rougher surface finish. Additionally, the cutting force is a function of the temperature at the interface between the chip-tool and work-tool. Thus, the cutting and thrust forces acquired during the machining process may be utilized to determine the material's machinability [14]. As mentioned in methods, machining operations were performed dry and no additional cutting fluids were used. Cutting forces were obtained for 3-, 6- and 9-mm

CT specimens in x, y and z directions to determine the amount of force imparted to the specimens during machining and displayed in Figure 16. Table 14 displays the amount of removed surface on each side of the specimens, machining parameters such as cutting and spindle speeds and the average forces for each specimen for different thickness in x, y and z direction. The results indicate that the driving cutting force is F_y and the main cutting force direction is in y direction. Additionally, As the amount of removed surface reduces, the amount of force in the z direction decreases, implying that the depth of cut is directly proportional to the force in the z direction.

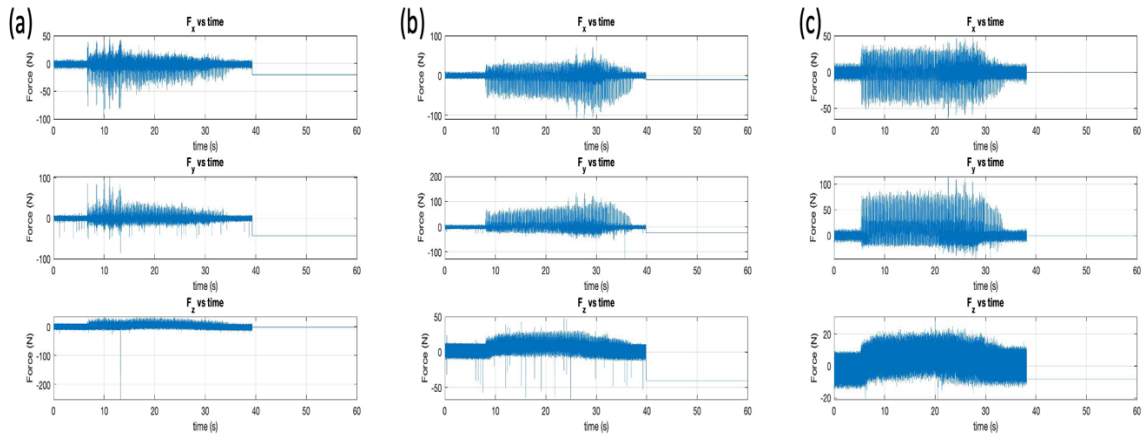

Figure 16: Force plot in x, y and z direction for 3(a), 6(b)- and 9(c)-mm thick CT specimens

Table 14: Summary of machining parameters & average forces

Thickness (mm)	Removed surface (mm)	Cutting Speed (in/min)	Spindle Speed (rpm)	Ave. F_X (N)	Ave. F_Y (N)	Ave. F_Z (N)
3	0.2	3	500	0	20	9
6	0.325	3	500	0	40	14
9	0.325	3	500	0	40	15

To exhibit tool wear, images were taken from the top and flank sides of the tools and illustrated in Figure 17 by utilizing an Olympus SC30 optical microscope. Two identical carbide end mills were employed in this study. The first tool was used on a total of 36 specimens. There are 18 specimens with a thickness of 6mm and 18 specimens with a thickness of 9mm. 0.325 mm of material was removed from each surface of the 36 specimens using tool 1. Tool 2 is used for 18 specimens with a thickness of 3mm. Each specimen's surface was reduced by 0.20 mm using tool 2. It is obvious from the collected images that both tools have some tool wear, with tool 1 being the most damaged due to its increased usage and greater depth of cut.

Table 15: Summary of tool usage

Tool #	# of specimens machined	Specimen Thickness (mm)	Amount of material removed (mm)
Tool 1	36	6 & 9	0.325
Tool 2	18	3	0.20

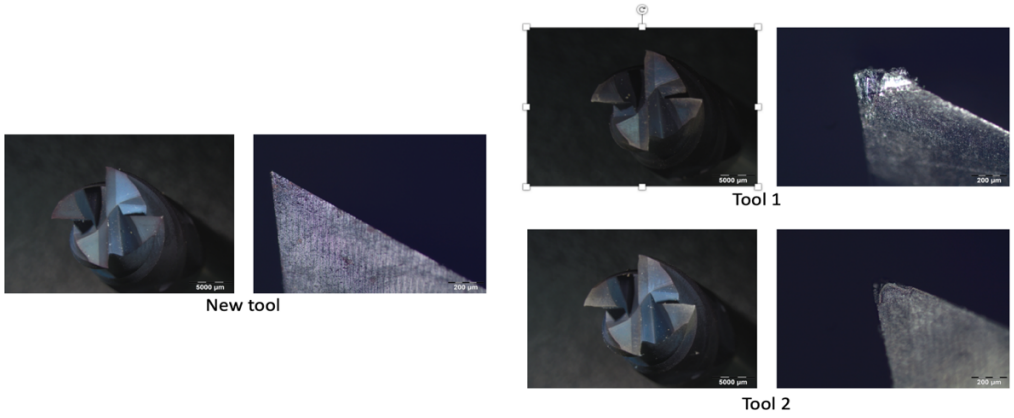

Figure 17: Tool wear images

µCT - Defect analysis

As mentioned in the methods section, defect analysis was carried out by another member of the UW EBM research team. Prior to testing, representative specimens of the build space were scanned using a computed tomography (CT) scanner to assess the presence and distribution of flaws along the crack growth path as shown in Figure 18. A total of fourteen (14) examples were chosen, varying in geometry and position from low to high. To gain a better understanding of the distribution of flaws in the build area, polynomial regression models are applied. To accomplish this, the Seaborn (SNS) statistical library with FacetGrit function was utilized in Python. The goal of the Seaborn library is to explore and understand the data. Its plotting functions operate on data frames and arrays containing the chosen data set and internally perform the necessary semantic mapping and statistical aggregation to produce informative plots. As mentioned above, 14 examples were chosen with different thicknesses, heights and radial distances to see the distribution of the pore size and sphericity.

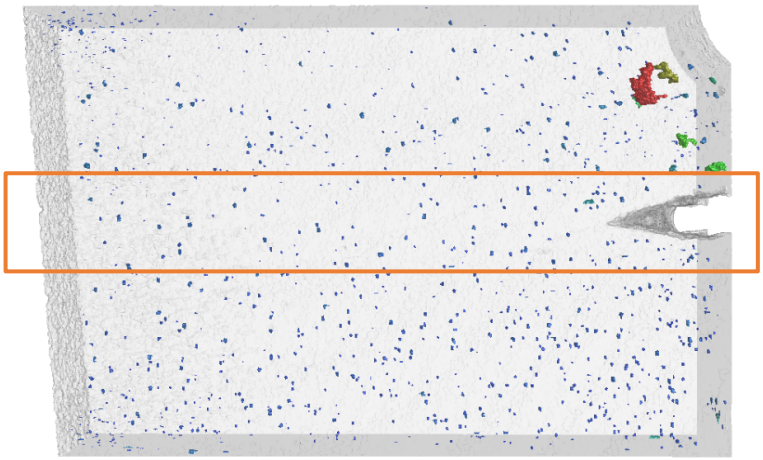

Figure 18: 3D reconstruction of a 6 mm thick specimen. The rectangular area indicates the area of interest, ahead of crack tip.

Figure 19 and 20 depicts the general distribution of pore size and sphericity at various sites. The diameter of the pores is defined as the largest diameter possible for the defect, while sphericity indicates the probability that the defect is a sphere, with zero (0) being the least probable and one (1) being the most likely.

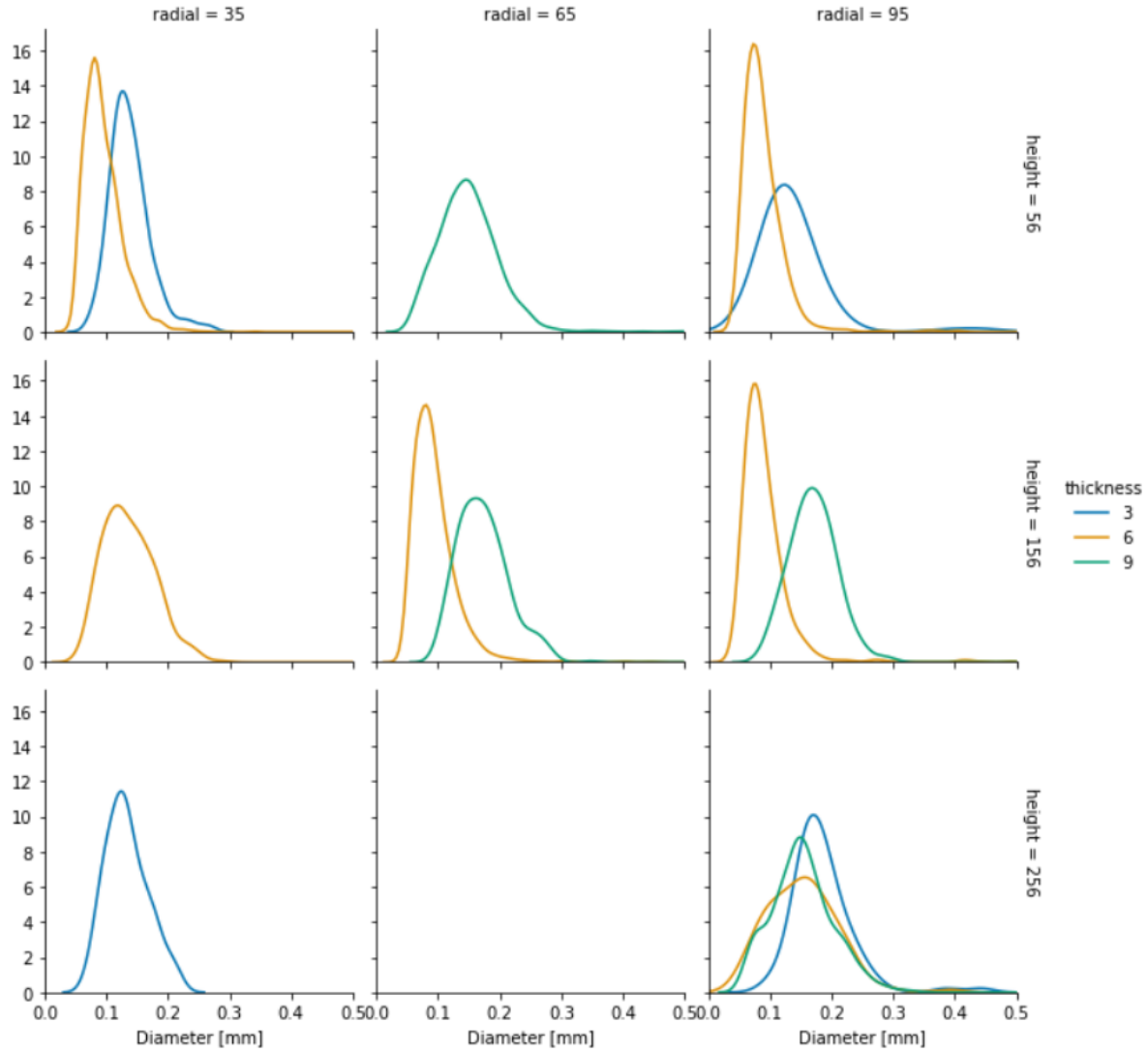

Figure 19: General Distribution of pore size

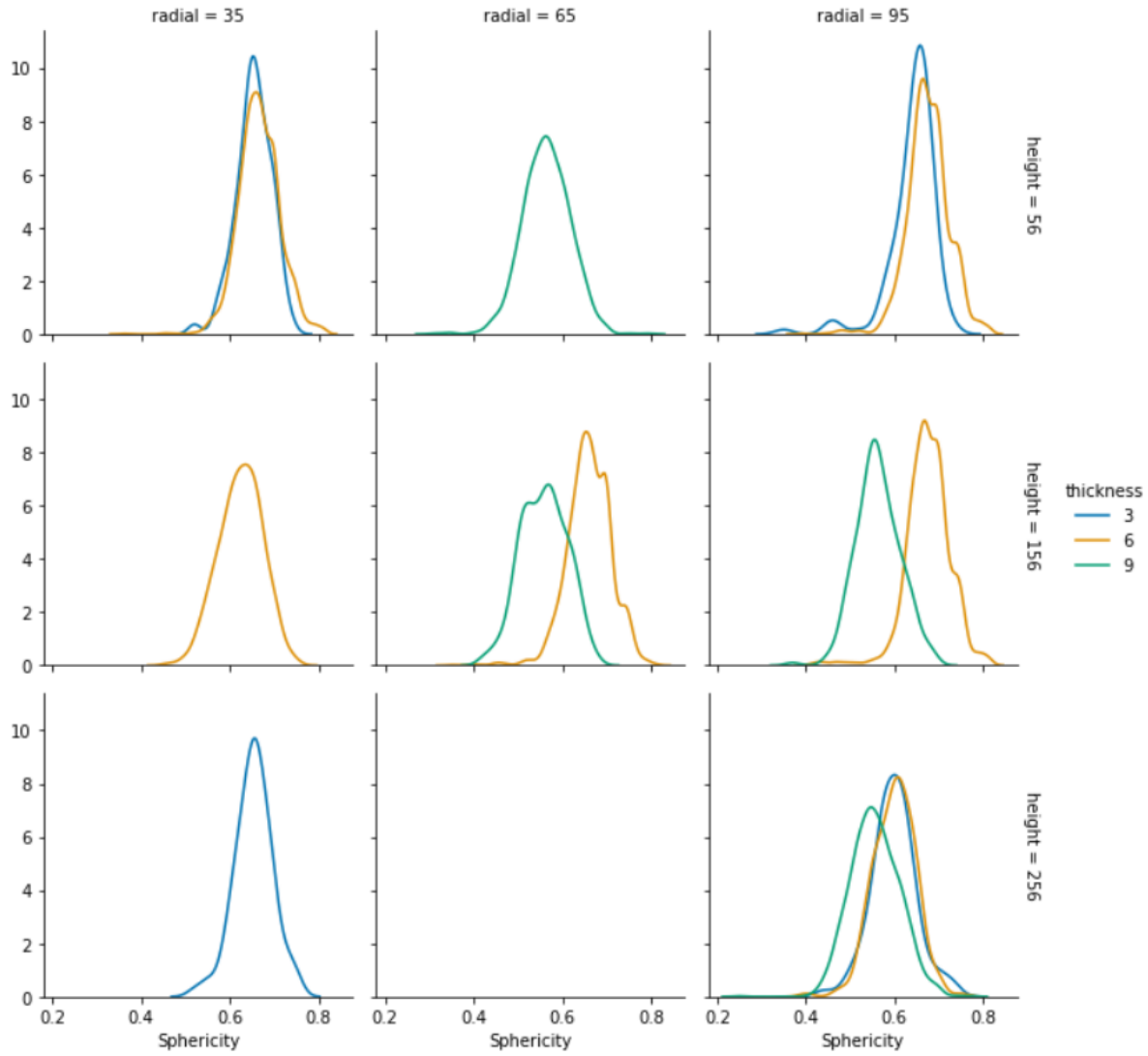

Figure 20: General distribution of sphericity

To gain a better understanding of the link between pore size and position within the build space, the diameters of the greatest 100 pores in 6 mm specimens are compared using a boxplot. The 6 mm specimens were chosen for comparison because the scans were done on a larger sample size, catching abnormalities in all three height and radial positions. When the overall diameter trend sizes are compared, the mean diameter size grows as the radial distance increases. Additionally, a rise in height at the lowest and highest radial sites results in a corresponding increase in pore diameter.

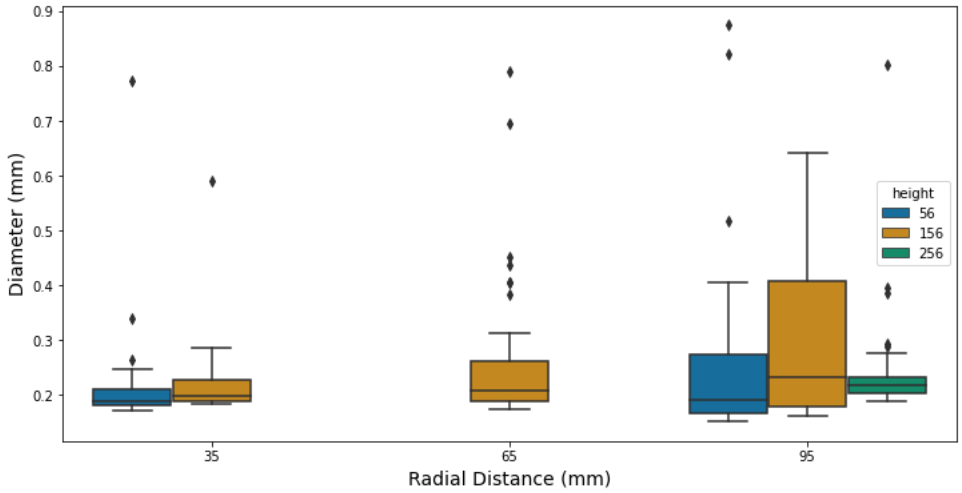

Figure 21: Spread of pore diameter for 6 mm specimens throughout the build space

Fracture toughness

The critical load and measured crack length were used to assess the fracture toughness of the machined and machined+HT samples, as described in the preceding chapter. The validity conditions put out by ASTM E399 were not fulfilled by some of the 6- and 9-mm specimens and all of the 3mm specimens [11]. The 3mm specimens failed the validity check due to P_{max} over P_Q values slightly higher than 1.10 and the obtained results from the validity check are illustrated in Table 16. In addition, K_c values were estimated to account for increased stresses inside the material due to the small thickness of 3-mm specimens [13]. Table 17 shows a summary of fracture toughness values for each thickness. The 6- and 9-mm machined and machined+HT samples' plane strain fracture toughness (K_{Ic}) values were reassuringly close to each other. The stated K_{Ic} values can be utilized as a material property reference for machined EBM Ti6AL4V with compliant thickness. As shown in Table 16, the machined specimens were found to have a slightly higher fracture toughness value than the machined+HT specimens. The K_c values obtained for the 3 mm specimens are greater than the K_Q values, as expected, since they account for the plane

stress conditions induced inside the specimen, and the machined 3 mm specimens have higher K_c values than the machined+HT specimens.

Table 16: Failed Pmax/PQ results for 3mm specimens

Specimen Location	Machined	Machined+HT
3_56_35	1.2	1.19
3_56_65	1.2	1.22
3_56_95	1.19	1.22
3_156_35	1.2	1.37
3_156_65	1.2	1.2
3_156_95	1.26	1.17
3_256_35	1.21	1.3
3_256_65	1.2	1.29
3_256_95	1.3	1.25

Table 17: Summary of fracture toughness values obtained for each thickness

Type	Thickness (mm)	Kq (MPa√m)	Kc (MPa√m)	Kic (MPa√m)	Ref
Machined	3	73.1 ± 6.3	104.7 ± 13.2		
	6	67.0 ± 11.5		66.0 ± 3.4	
	9	76.3 ± 4.5		66.4 ± 3.9	
Macined+HT	3	61.07±5.2	92.5±8.1		
	6	66.4		64.0±5.9	
	9	68.8±6.7		63.1 ±2.9	
Wrought, air cooled				67.5	[Boyer]
Cast, annealed		77 ± 12.5			[Eylon]

An overall distribution of fracture toughness values along the build space is presented to help comprehend the general distribution of the data in Figure 22 and 23. This was achieved by utilizing the Seaborn (SNS) statistical library with FacetGrit function in Phyton. Twenty seven (27) machined and 27 machined+HT specimens' fracture toughness data were used. The numbers for each thickness and location follow a normal distribution overall and the distribution of the machined and machined+HT fracture data is relatively close to matching. The distribution is symmetrical around its mean and most of the observed results cluster around a central peak. Furthermore, as the height grows, the 6 and 9mm machined specimens both indicate only K_Q values. The machined+HT specimens do not follow the same pattern because all 6mm machined+HT specimens report K_{Ic} values as the height increases.

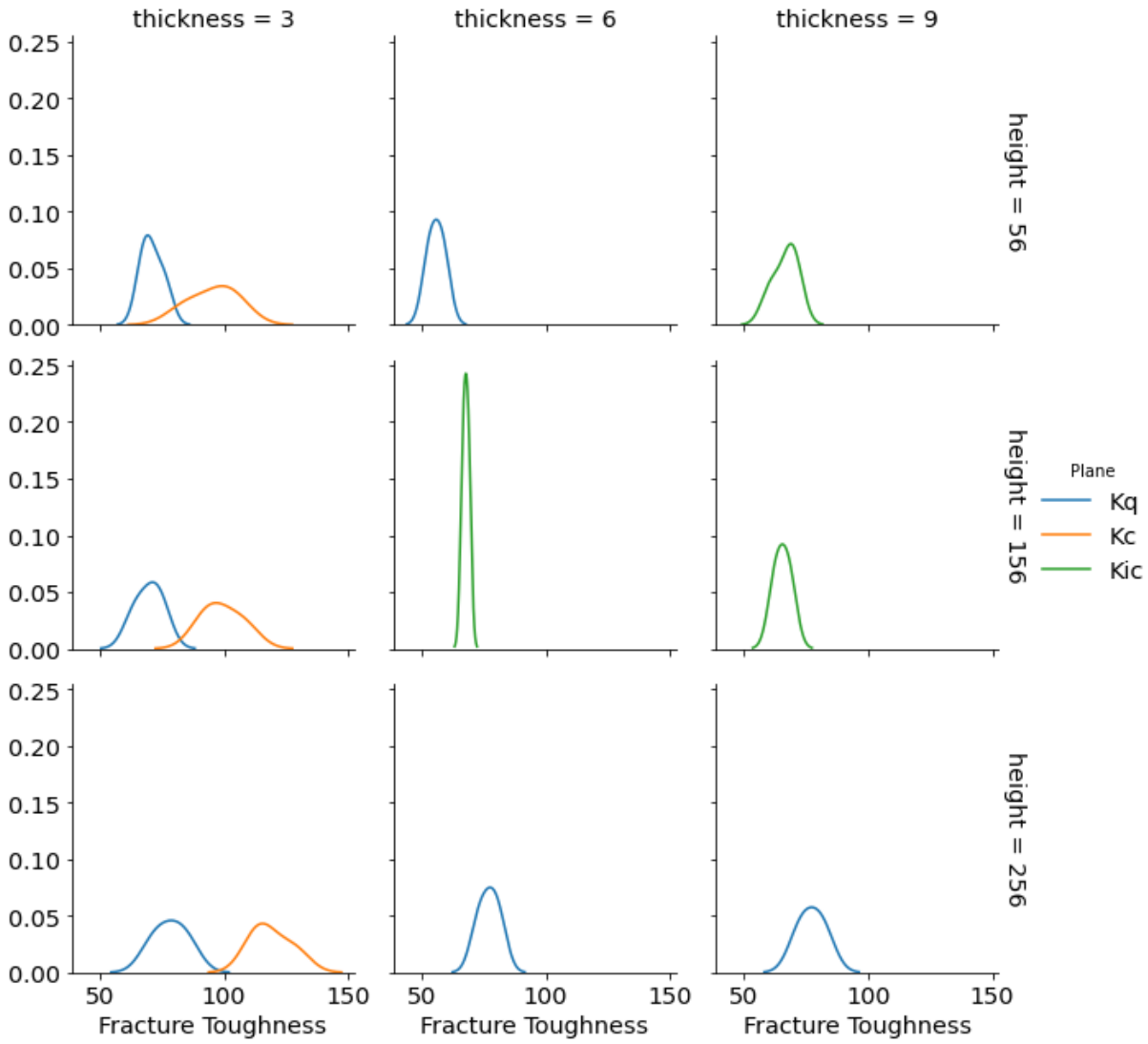

Figure 22: Fracture toughness values, Kc/KQ/KIc for the machined 3-, 6- and 9-mm specimens

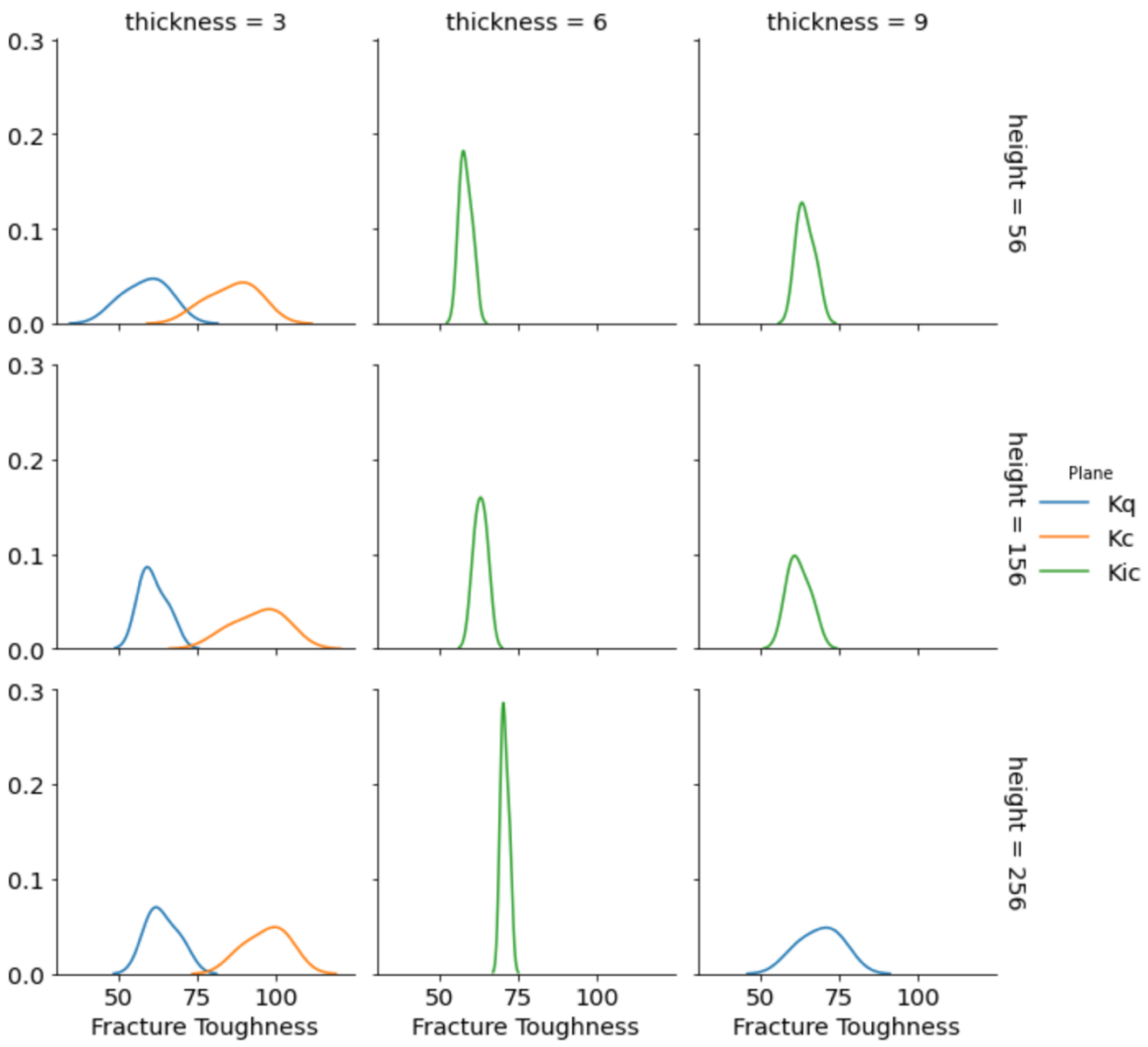

Figure 23: Fracture toughness values, Kc/KQ/KIc for the machined+HT 3-, 6- and 9-mm specimens

Figures 24 and 25 illustrate the fracture toughness values as a function of thickness, height, and radial distance for machined and machined+HT specimens, respectively. When the entire trend is considered, a decline in fracture toughness values is evident as the radial distance increases, particularly on machined specimens.

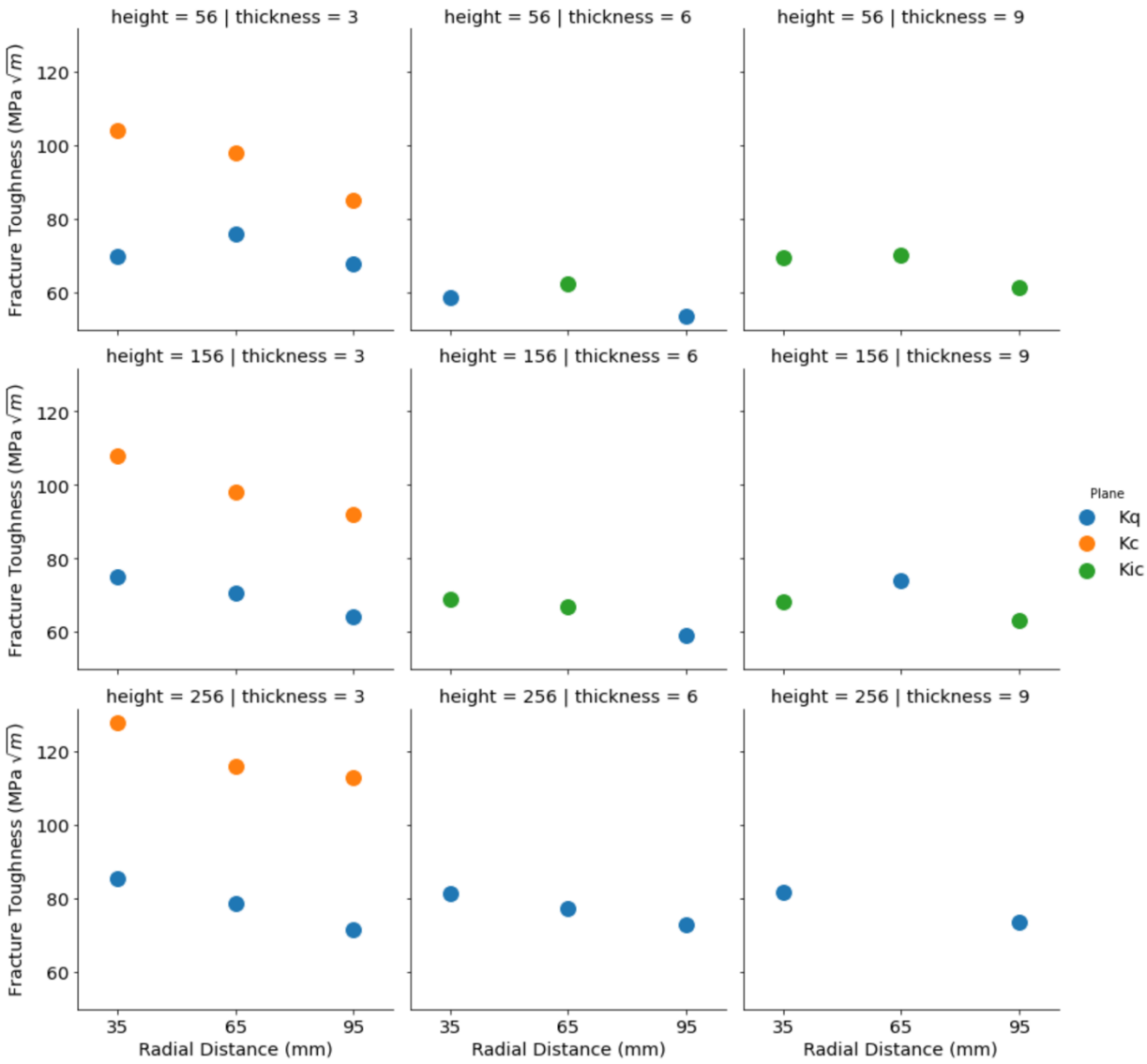

Figure 24: Overall summary of fracture toughness values (Machined)

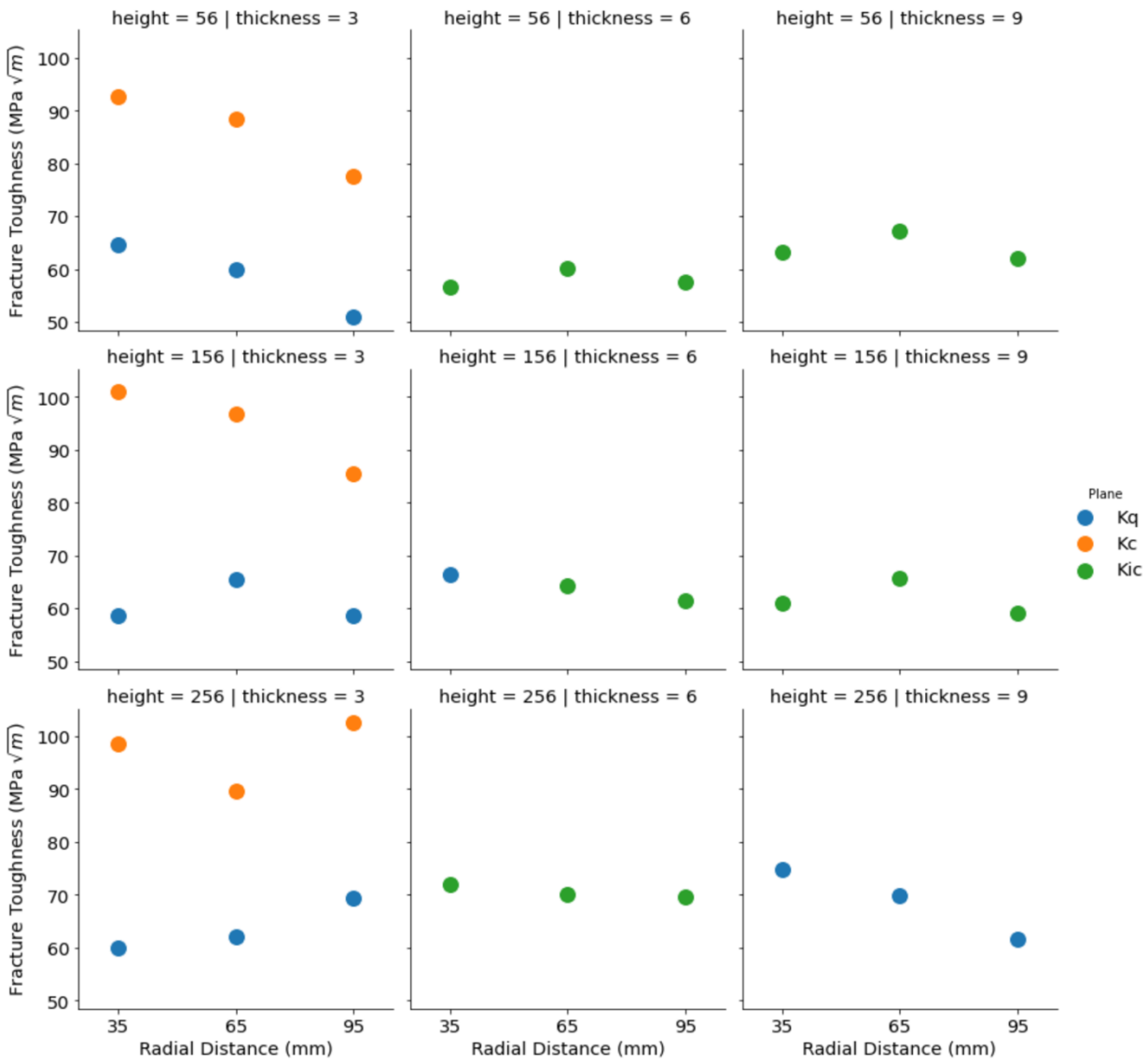

Figure 25: Overall summary of fracture toughness values (Machined+HT)

To gain a better understanding of the correlations between the parameters (thickness, radial distance, and height), the relative influence of the factors and their interactions were examined using polynomial regressions. The machined sample model was determined to be significant ($p \leq 0.05$), and the p-values for the three parameters are listed in Table 18. The thickness, height,

and radial distance all showed significant trends, with thickness having the major effect due to the lower thickness of the 3-mm specimens. Figure 26 illustrates the effect of each parameter on fracture toughness. Thickness followed a quadratic relationship, with a significant decreasing trend from 3 to 6 mm. This is due to the plane stress behavior of 3mm specimens; inflated K_c values caused this significant drop between 3- and 6-mm thicknesses. Height was the second most important factor in the positive linear trend in the fracture toughness values; there is an increase in fracture toughness as height increases. With reference to radial distance, a modest negative trend was seen, with an increase in radial distance resulting in a drop in fracture toughness.

Table 18: Results of the ANOVA statistical significance test for machined specimens

	p-value
Thickness	< 0.0001
Height	< 0.0001
Radial Distance	< 0.0001

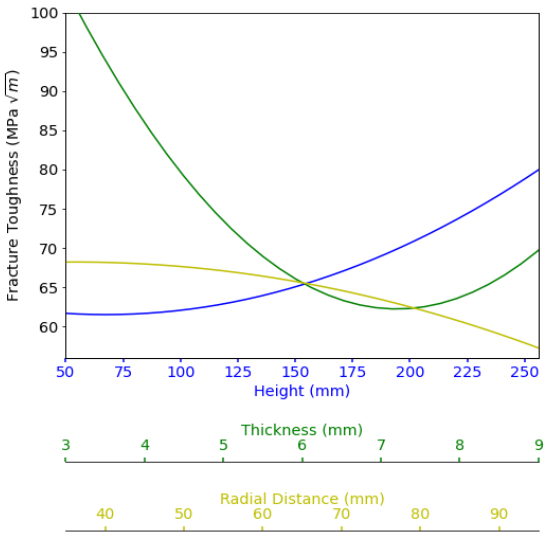

Figure 26: Build space interactions on fracture toughness. The lines correspond to the regression model with the other factors held at the middle level.

Fractography

The fracture surfaces of all specimens were analyzed using an optical microscope to obtain an image record of the pre-crack region. Specimens exhibited ductile fracture characteristics, with a reduction in total shear lip area with increase in thickness. Shear lips are the ledges on the side of the specimen that make a 45 degree to the plane of fracture. Porosity and lack of fusion defects were also observed in the pre-crack and fracture region, as shown in Figure 29.

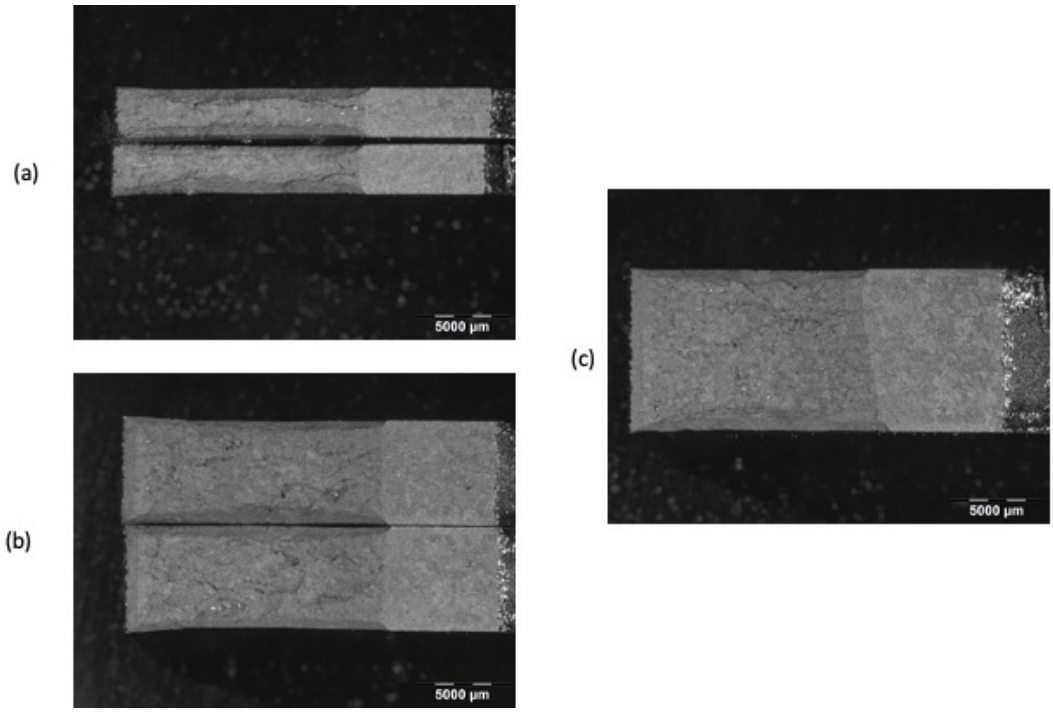

Figure 27: Fracture surfaces for representative CT specimens of each thickness. Shown are specimens with 3(a), 6(b) and 9(c)mm thickness.

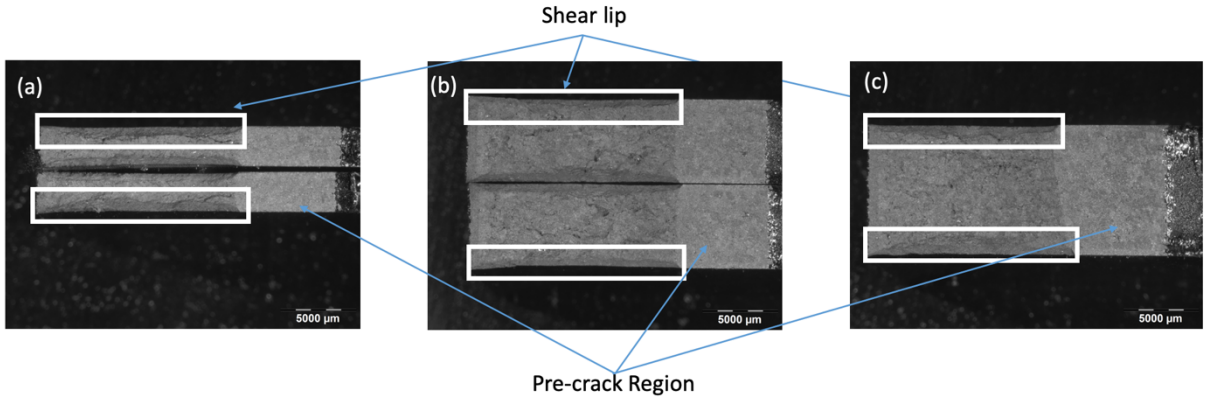

Figure 28: Detailed fracture surface for 3mm(a), 6mm(b) and 9mm(c) CT specimen (Shear lip & pre-crack region)

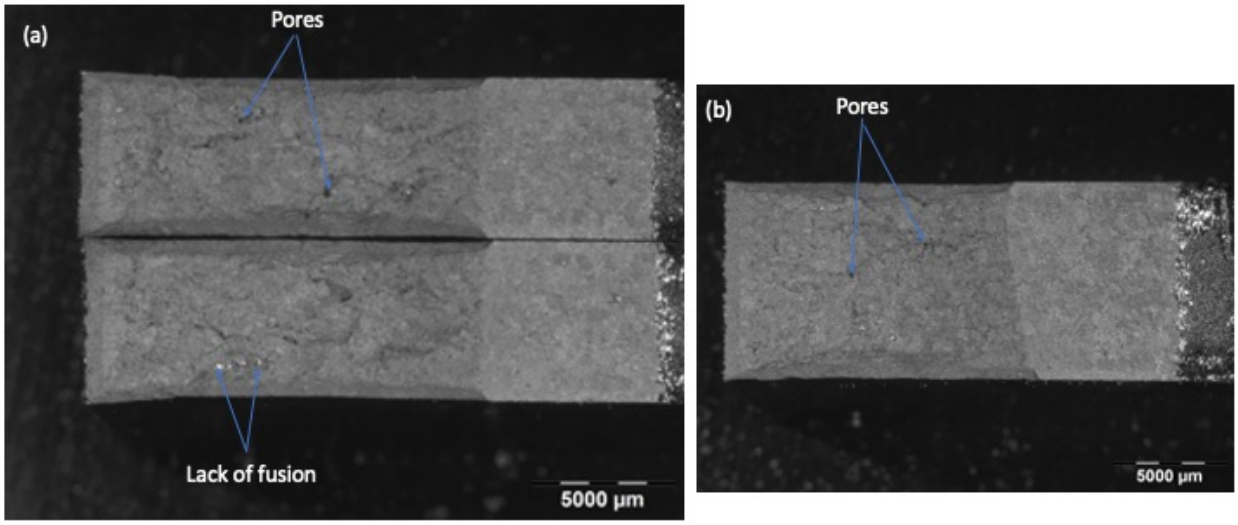

Figure 29: Example of porosity and lack of fusion defects

Hardness

Like µCT analysis, hardness analysis was carried out by a different member from the UW EBM research group. Micro-hardness measurements of chosen 9 mm specimens were acquired to map the material characteristics of the metal within the build area to address one source of possible variability with the machined and machined+HT specimens. A total of 11 specimens were chosen, ranging in height and radial distance from the highest to the lowest, and 7 measurements were taken from each specimen. The average values obtained from the specimens are shown in Table 19 and were slightly higher than the 323 HV obtained from the EBM process of similar thickness [15]. There was no apparent variation in hardness across the build space or between the two samples.

Table 19:Vickers microhardness properties of treated samples

Machined	Machined + HT
366.5 ± 10.0	368 ± 5.2

Chapter 5: Discussion

As previously stated, there are a small number of published studies focused on fracture toughness in EBM AM processed Ti6Al-4V material. However, these studies were unable to report valid K_{Ic} values. Seifi et al. reported that orientation-dependent changes in microstructure, texture, and defects result in considerable variances in fracture toughness properties. In his study, 5 different orientations and directions were considered, and the obtained fracture toughness values ranged between 65 to 80 MPa√m. However, the obtained results from this study reported all K_Q values due to the violation of ASTM thickness criteria [9]. Furthermore, Edwards et al. reported fracture toughness values higher than 100 MPa√m for specimens built in vertical and horizontal direction. Despite the specimens' higher fracture toughness values, plane-strain criteria were not satisfied due to the thickness requirements, which may have contributed to the inflated fracture toughness values [10]. It is evident that thickness is the key factor to obtain fracture toughness values as a material property (K_{Ic}) in plane-strain conditions. In this study, different thicknesses were investigated (3, 6 and 9mm) and K_{Ic} values are reported roughly at 65 MPa√m as a material property for 6 and 9mm specimens. However, 3mm thick specimens violated the ASTM E399 thickness requirement for plane strain condition and they were investigated in plane stress condition according to ASTM E561. Machined 3mm specimens reported significantly higher K_c values than the machined+HT specimens and this trend is seen on all fracture toughness values that were reported in this study. Machined specimens exhibit higher fracture toughness values than machined+HT specimens, which is most likely the result of the machining process's produced compressive residual stresses. Due to the fact that annealing substantially reduces residual stresses and achieves a balance between tensile and compressive

residual stresses, the measured fracture toughness values for machined +HT specimens are lower than those obtained from machined specimens.

Castings or machined renderings of wrought metal plates and bars are the traditional manufacturing processes for Ti6Al4V components used in aerospace. Since castings have significantly decreased material properties compared to wrought products, the objective of printed metal is to obtain a comparable performance to that of the wrought metal and thereby offer an alternative solution to both of the traditional processes. Thus, it was necessary to obtain comparison DOE fracture toughness data from cast and wrought form sources. As seen in Table 19, The average K_{ic} results obtained from this study to be around 65 MPa√m which is like the wrought air cooled Ti6Al4V. Furthermore, specimen location was also found to be significant in the fracture toughness properties. An increase in radial distance causing a decrease in fracture toughness values. Additionally, an increase in fracture toughness was noted with an increase in height and a decrease in radial distance.

The size and distribution of defects were analyzed using μCT analysis to better understand the decrease in machined fracture toughness parameters inside the build space. Specimens with varying thicknesses, radial distances, and heights were scanned, and a positive linear association between defect size and radial distance was discovered. With an increase in defect size and count, fracture toughness values are projected to decrease. As a result, the radial dependence on fracture toughness may be due to increased pore size.

A 3D response model for the fracture toughness of the metal with respect to radial distance and height is provided in Figure 30 for machined and Figure 31 for machined+HT

specimens. Similar trends existed for each thickness and both models presented are for the 6 mm specimens. This model describes the behavior of material built within the build chamber and can serve as a recommendation for optimal properties.

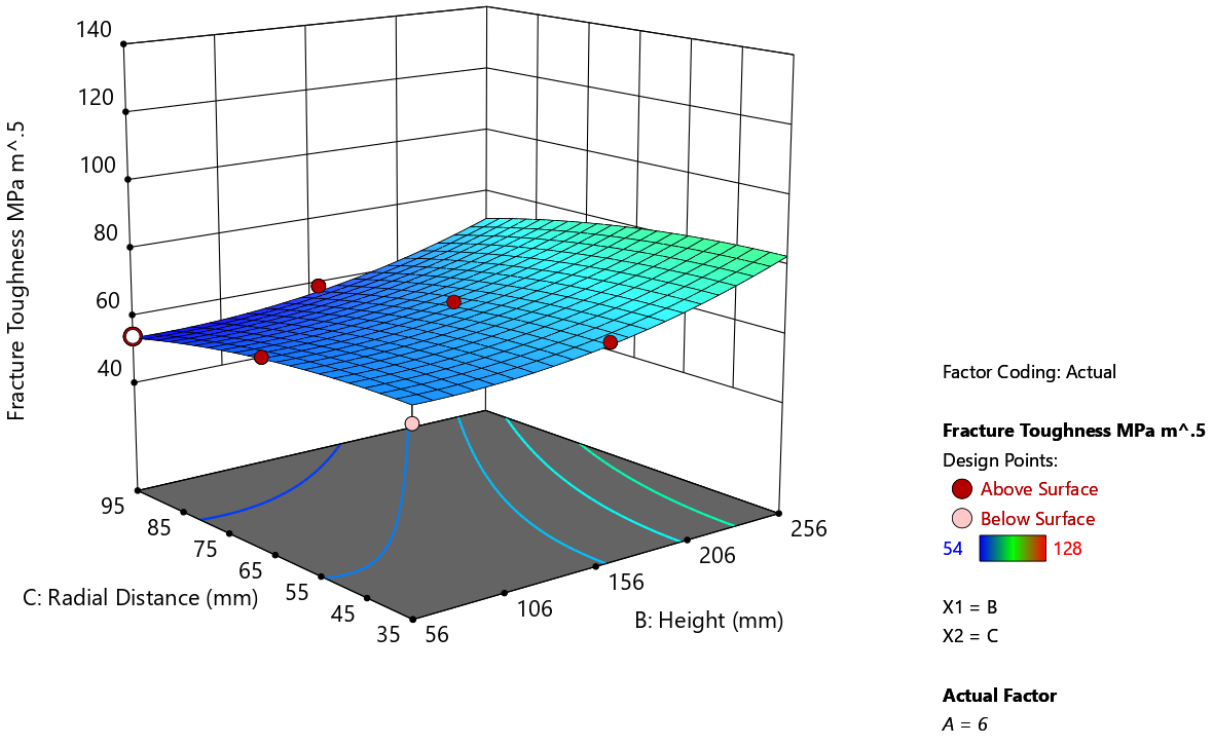

Figure 30: 3D Response model for machined specimens

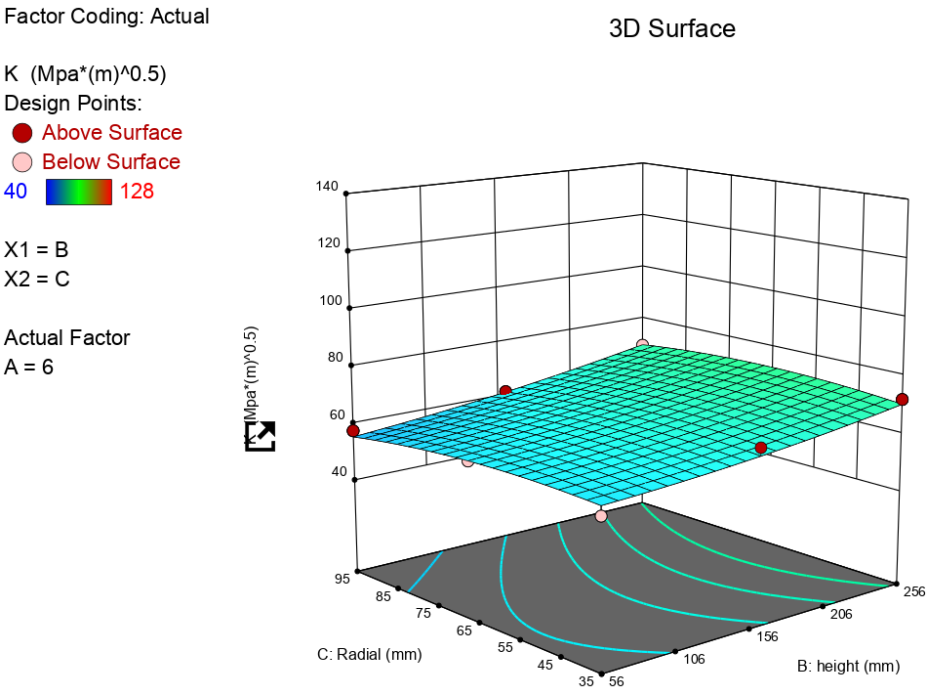

Figure 31: 3D Response model for machined+HT specimens

To gain a better understanding on thickness dependency and get a consistent plane-strain fracture value that doesn't violate the ASTM E399 thickness requirements, additional specimens thicker than 9 mm would need to be printed and tested. Additionally, a more precise understanding of the location variances may be achieved by restricting the design parameter to one thickened specimen each of the zones of the build space.

Chapter 6: Conclusion and Recommendations for Future Work

Conclusion

Fracture toughness testing of machined and heat treated Ti6Al4V specimens produced by EBM is conducted to understand the influence of surface roughness, thickness, and location on the material's resistance to fracture. The average results of the materials fracture toughness properties are measured around 65 MPa√m. Thickness contributed greatly to the fracture toughness. With an increase in thickness valid plane strain values were obtained. Radial distance and height also contributed to variation on the fracture toughness values. Increased radial distance decreased the fracture toughness values on the other hand increased in height increased the fracture toughness properties. Additionally, the percentage difference in K_{Ic} values between machined and machined+HT is 4%, which is not statistically significant for experimental data. This is most likely because EBM produces components with little or no residual stresses, which translates into a nearly insignificant change in fracture toughness values. Moreover, surface roughness difference seemed to have almost no effect on fracture toughness values; the percentage difference between machined and machined+HT surface roughness values was 38%, but this large difference did not cause a significant difference in machined and machined+HT fracture toughness values.

Finally, one use of AM components manufactured with EBM is to add fittings to wrought plates. Thus, the final section would have portions of wrought material and features created using printed materials. If the printed AM material has a low fracture toughness and the wrought material has a high fracture toughness, the crack should propagate rapidly once it enters a region containing AM metal. This results in quick failure of the component, making this technology

undesirable. However, the findings of this investigation suggested that the fracture toughness values of printed and wrought materials are relatively similar, which makes this technology attractive.

Recommendations for Future Work

In this study, fracture toughness properties of material were shown to be dependent on thickness and build location. It was established that the difference in properties with thickness was caused by internal stresses inside the specimens. On the other hand, a better correlation between the fracture toughness properties and build location must be established by studying micromechanics of fracture. To have a complete understanding of the micromechanics of fracture, two areas must be investigated further: defects and microstructure. The existing body of research does not fully explain the fracture toughness behavior at various heights. The fracture trends may be better explained by evaluating the microstructures and flaws on each specimen with variable thickness, radial distance, and height.

Additionally, the impact of various post-treatments such as HIP and shot peening should be explored. These post-treatments can be applied to both as-built and machined CT specimens to observe how the fracture toughness properties behave differently. The HIP process can assist in sealing internal pores and inducing compressive residual stresses on the surface of the specimens, respectively. This can result in a greater fracture toughness rating for EBM AM Ti6Al-4V produced material.

Heat treatment was utilized in this study just for the purpose of annealing the specimens following machining, but in future research, heat treatment might be used to alter the microstructure of the specimen to observe the behavior of the fracture toughness values.

Moreover, in the current study, all machining parameters, such as feed rate and spindle speed, were maintained at constant values. These factors may be changed to observe what influence they have on the surface finish, tool wear, and fracture toughness results for future study.

The joint between the as-printed and wrought material is a very important topic to consider for future research since the results from this study indicated that the fracture toughness of Ti6Al4V is similar between as-printed and wrought material. Creating a half of a CT specimen from a wrought Ti6Al4V and adding the other half by utilizing EBM technology can allow us to investigate the effects of fracture toughness behavior of a hybrid specimen. A successful investigation in this area may open the way for building new features on an existing part by utilizing EBM technology.

Furthermore, in this study, three different thicknesses of specimens were used: 3, 6, and 9 millimeters (mm). The results showed that the 3mm specimens violated the plane strain conditions according to the ASTM E399 test method because of their smaller thickness and they performed as if they were behaving in the plane stress condition, resulting in artificially inflated results. For additional study, larger specimen sizes must be considered. Instead of using a 3 mm specimen thickness, a 12mm specimen thickness could be utilized to ensure that the plane strain condition is not violated during the test. It is possible to develop a more accurate fracture toughness relationship between various thicknesses in this manner.

Finally, alternative experimental designs can be developed. The building direction of the crack path was vertical in this study, however the specimens' building directions were shifted roughly 15 degrees on the X-Y (build plane) plane from the origin. For future study, having a vertical and horizontal building direction for the crack route, as well as constructing the

specimens parallel to the X and Y axes of the build plate, can alter the microstructure, which in turn affects the fracture toughness performance of the specimens.

References

1. Chern, Andrew H, Nandwana, Peeyush, Yuan, Tao, et al. A review on the fatigue behavior of Ti-6Al-4V fabricated by electron beam melting additive manufacturing. *International journal of fatigue*. 2019;119(C):173-184. doi:10.1016/j.ijfatigue.2018.09.022
2. M. Seifi, A. Salem, J. Beuth, O. Harrysson, J.J. Lewandowski, Overview of Materials Qualification Needs for Metal Additive Manufacturing, JOM. 68 (2016) 747 – 764.https://doi.org/10.1007/s11837-015-1810-0.
3. Murr, L. E. (2018). Additive manufacturing of biomedical devices: an overview. Materials Technology, 33(1), 57–70. https://doi.org/10.1080/10667857.2017.1389052
4. Landau, E., Tiferet, E., Ganor, Y. I., Ganeriwala, R. K., Matthews, M. J., Braun, D., Chonin, M., & Ziskind, G. (2020). Thermal characterization of the build chamber in electron beam melting. https://doi.org/10.1016/j.addma.2020.101535
5. Franchitti S, Pirozzi C, Borrelli R. Influence of hot isostatic pressing and surface finish on the mechanical behaviour of Ti6Al4V processed by electron beam melting. Fatigue & fracture of engineering materials & structures. 2020;43(12):2828-2841. doi:10.1111/ffe.13295
6. Gao W, Zhang Y, Ramanujan D, et al. The status, challenges, and future of additive manufacturing in engineering. Computer aided design. 2015;69:65-89. doi:10.1016/j.cad.2015.04.001
7. Khanna N, Zadafiya K, Patel T, Kaynak Y, Rahman Rashid RA, Vafadar A. Review on machining of additively manufactured nickel and titanium alloys. Journal of materials research and technology. 2021;15:3192-3221. doi:10.1016/j.jmrt.2021.09.088
8. Zhu XK, Joyce JA. Review of fracture toughness (G, K, J, CTOD, CTOA) testing and standardization. Engineering fracture mechanics. 2012;85:1-46. doi:10.1016/j.engfracmech.2012.02.001
9. Seifi M, Dahar M, Aman R, Harrysson O, Beuth J, Lewandowski JJ. Evaluation of Orientation Dependence of Fracture Toughness and Fatigue Crack Propagation Behavior of As-Deposited ARCAM EBM Ti-6Al-4V. JOM (1989). 2015;67(3):597-607. doi:10.1007/s11837-015-1298-7
10. Edwards P, O'Conner A, Ramulu M. 2013. Electron beam additive manufacturing of titanium components: properties and performance. J. Manuf. Sci. Eng. 135(6):061016
11. ASTM Standard E399-20: Standard Test Method for Linear-Elastic Plane-Strain Fracture Toughness of Metallic Materials. 2020. DOI: 10.1520/E0399-20.
12. Teixeira Óscar, Silva FJG, Ferreira LP, Atzeni E. A Review of Heat Treatments on Improving the Quality and Residual Stresses of the Ti–6Al–4V Parts Produced by Additive Manufacturing. Metals (Basel). 2020;10(8):1006. doi:10.3390/met10081006
13. ASTM Standard E561-20: Standard Test Method for KR Curve Determination. 2020.
14. Anandan N. Study of Machinability of Metal Matrix Composites and Its Effect on Surface Integrity. Published online 2020.

15. Kok Y, Tan X, Tor S, Chua CK. 2015. Fabrication and microstructural characterisation of additive manufactured Ti-6Al-4V parts by electron beam melting. Virtual Phys. Prototyp. 10(1):13–21
16. Boyer, R.: Welsch, G.: and Collings, E. W.: 1994, Materials and Properties Handbook Titanium Alloys, ASM International, Materials Park, OH, pp.517–548

Appendix A: Machined Fracture Toughness Data

Load vs Displacement Curves & Optical Microscope Fracture Surface pictures

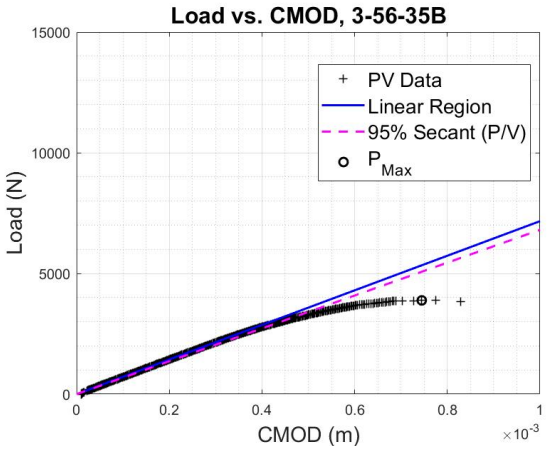

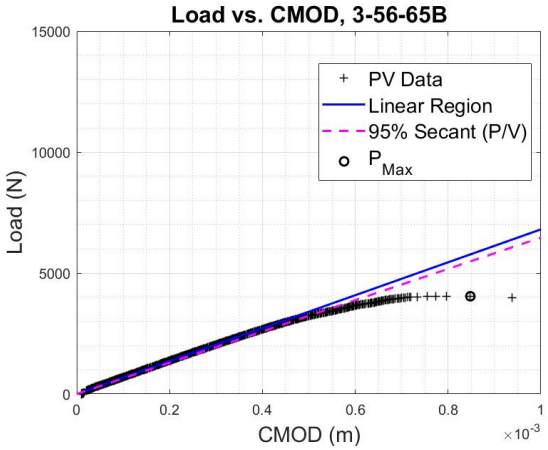

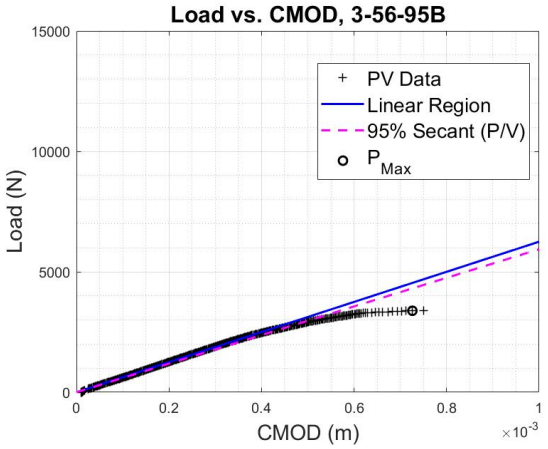

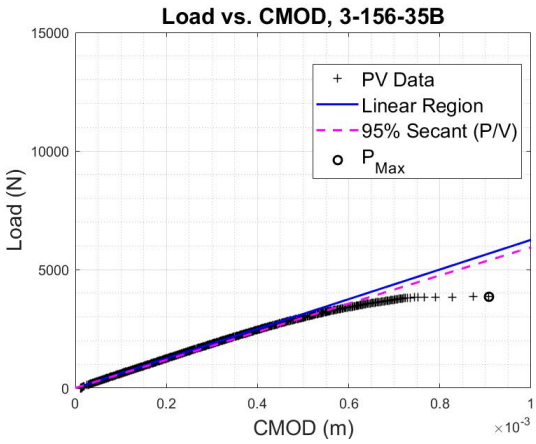
Load vs. CMOD, 3-156-35B
PV Data
Linear Region
95% Secant (P/V)
P Max
Load (N)
CMOD (m)
15000
10000
5000
0
0.2
0.4
0.6
0.8
1
×10-3

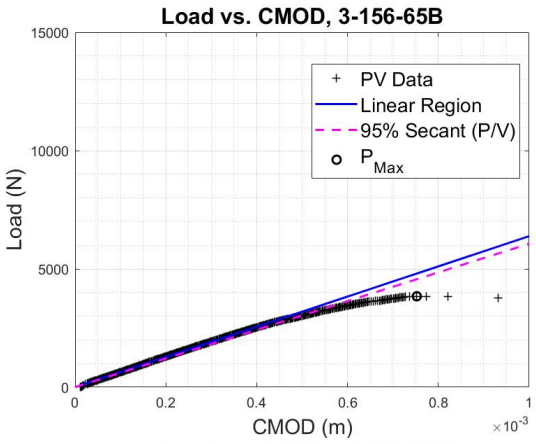
Load vs. CMOD, 3-156-65B
PV Data
Linear Region
95% Secant (P/V)
P Max
Load (N)
CMOD (m)
15000
10000
5000
0
0.2
0.4
0.6
0.8
1
×10-3

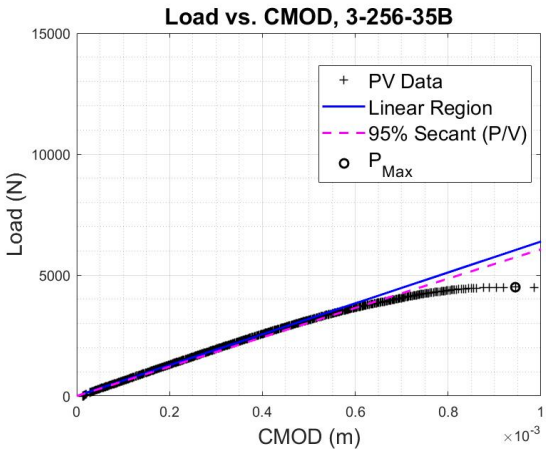
Load vs. CMOD, 3-256-35B
PV Data
Linear Region
95% Secant (P/V)
P Max
Load (N)
CMOD (m)
15000
10000
5000
0
0.2
0.4
0.6
0.8
1
×10-3

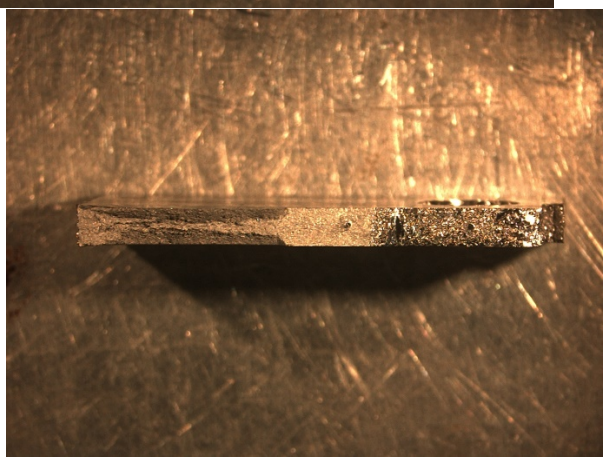

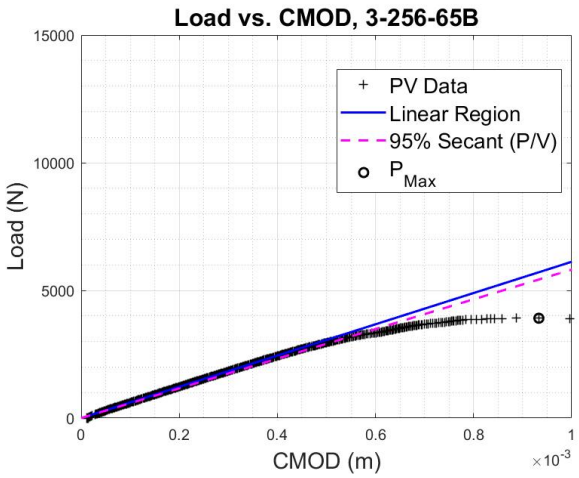
Load vs. CMOD, 3-256-65B
PV Data
Linear Region
95% Secant (P/V)
P Max
Load (N)
CMOD (m)
×10-3

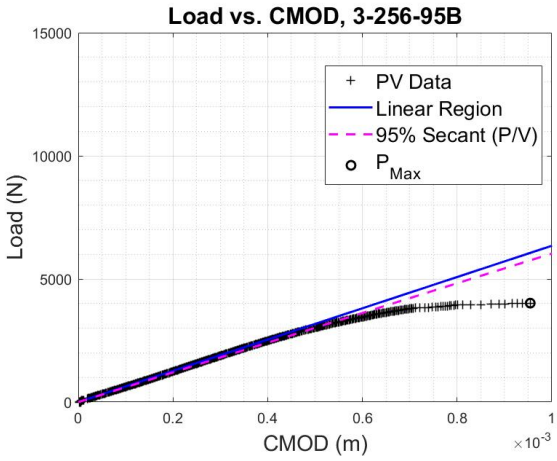
Load vs. CMOD, 3-256-95B
PV Data
Linear Region
95% Secant (P/V)
P Max
Load (N)
CMOD (m)
×10-3

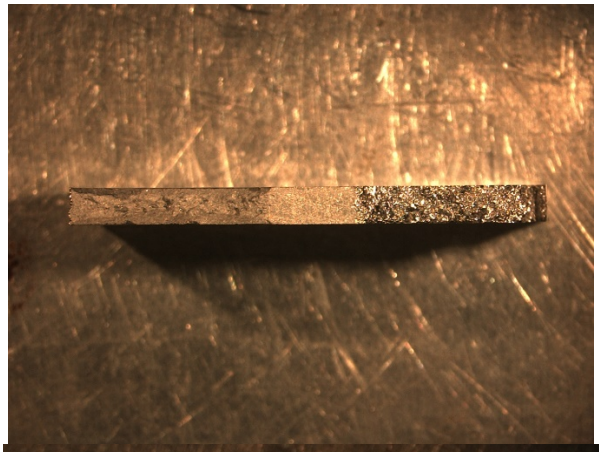

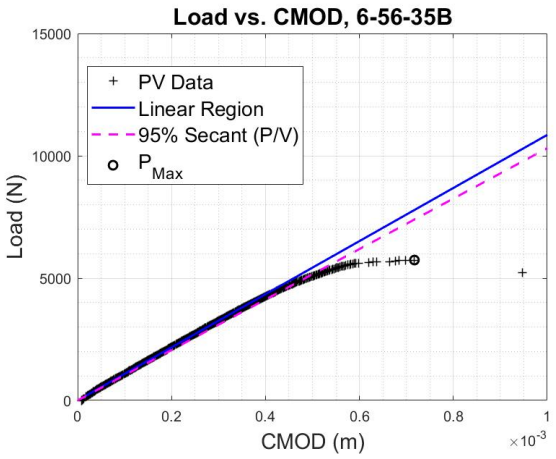
Load vs. CMOD, 6-56-35B
PV Data
Linear Region
95% Secant (P/V)
P Max
Load (N)
CMOD (m)
×10-3

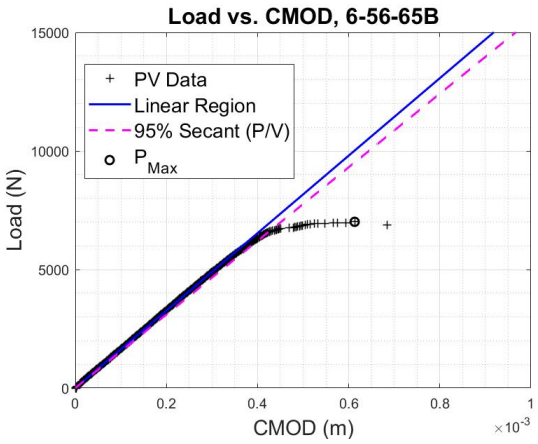
Load vs. CMOD, 6-56-65B
PV Data
Linear Region
95% Secant (P/V)
P Max
Load (N)
CMOD (m)
×10-3

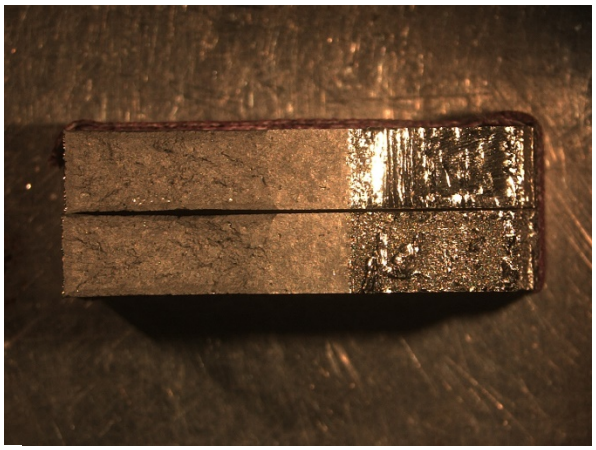

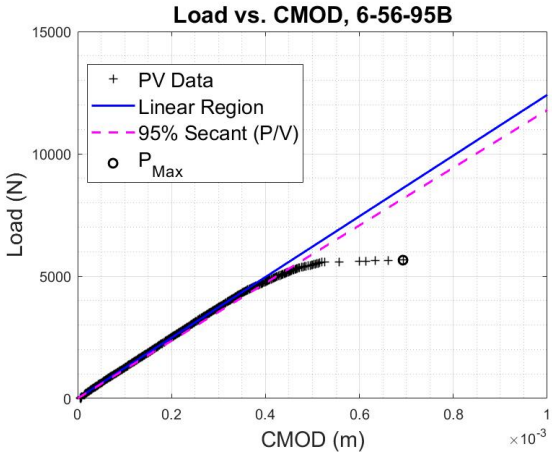
Load vs. CMOD, 6-56-95B
PV Data
Linear Region
95% Secant (P/V)
P Max
Load (N)
CMOD (m)
×10-3

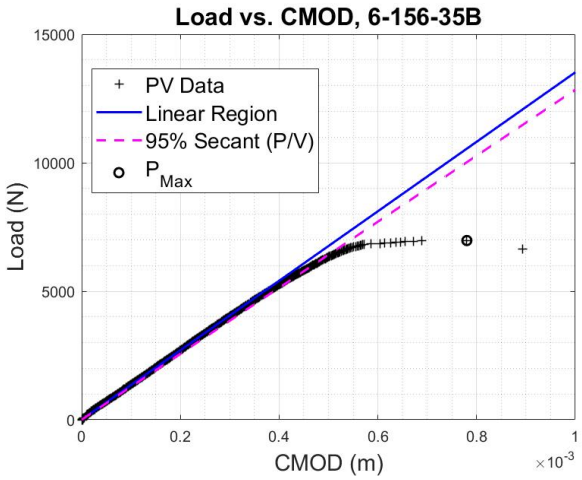
Load vs. CMOD, 6-156-35B
PV Data
Linear Region
95% Secant (P/V)
P Max
Load (N)
CMOD (m)
×10-3

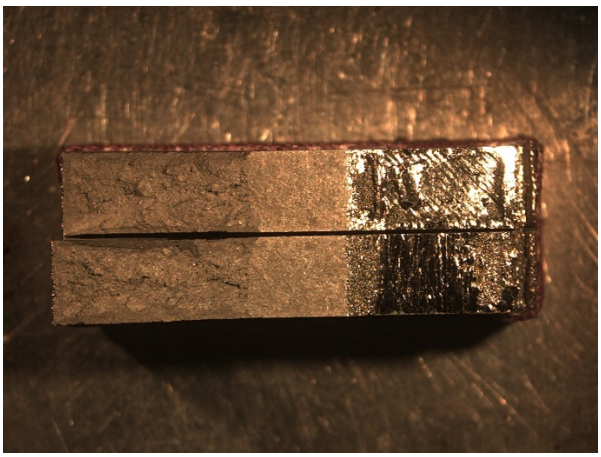

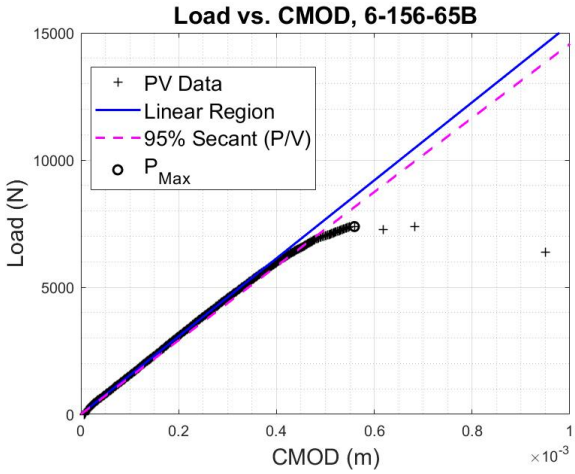
Load vs. CMOD, 6-156-65B
PV Data
Linear Region
95% Secant (P/V)
P Max
Load (N)
CMOD (m)
15000
10000
5000
0
0
0.2
0.4
0.6
0.8
1
×10-3

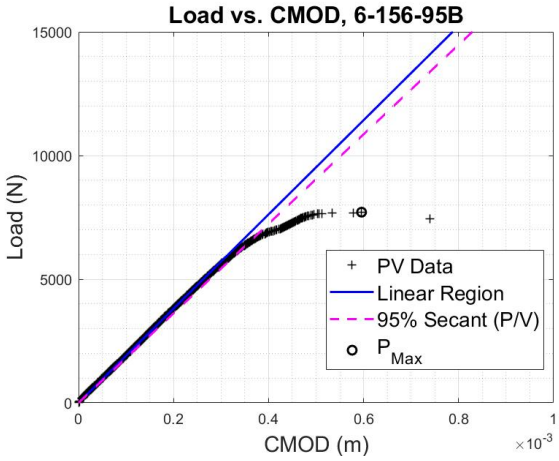
Load vs. CMOD, 6-156-95B
PV Data
Linear Region
95% Secant (P/V)
P Max
Load (N)
CMOD (m)
15000
10000
5000
0
0
0.2
0.4
0.6
0.8
1
×10-3

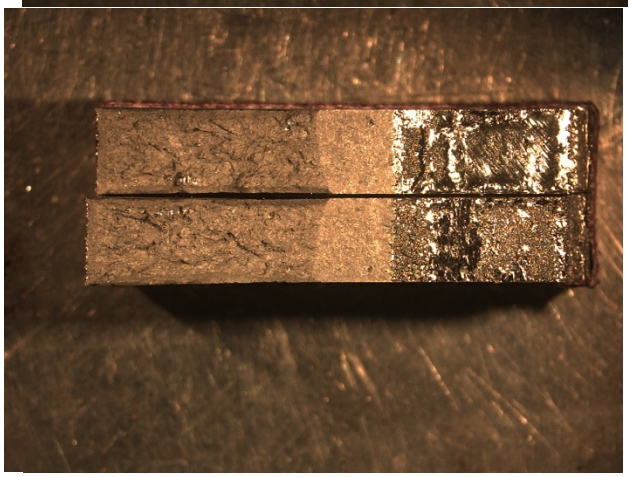

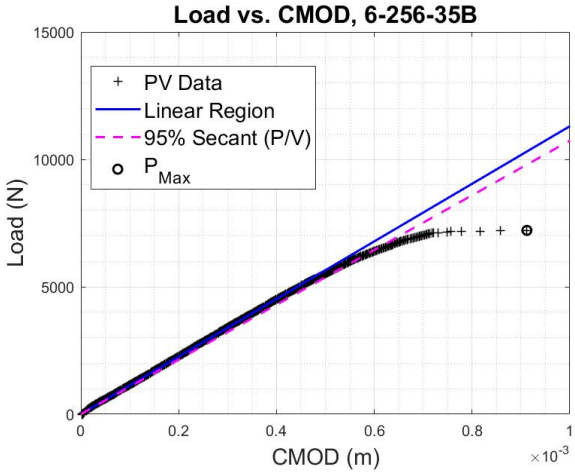
Load vs. CMOD, 6-256-35B
PV Data
Linear Region
95% Secant (P/V)
P Max
Load (N)
CMOD (m)
15000
10000
5000
0
0
0.2
0.4
0.6
0.8
1
×10-3

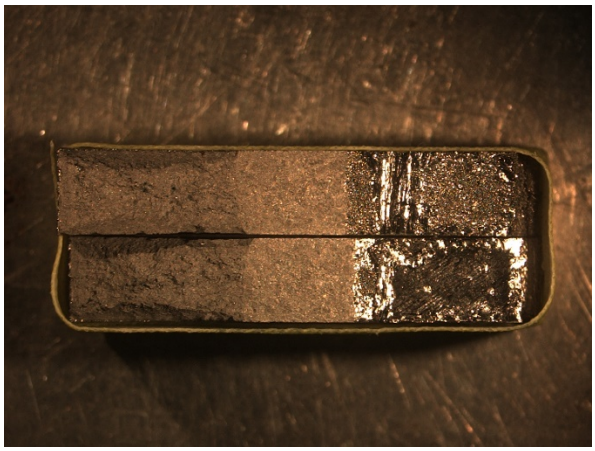

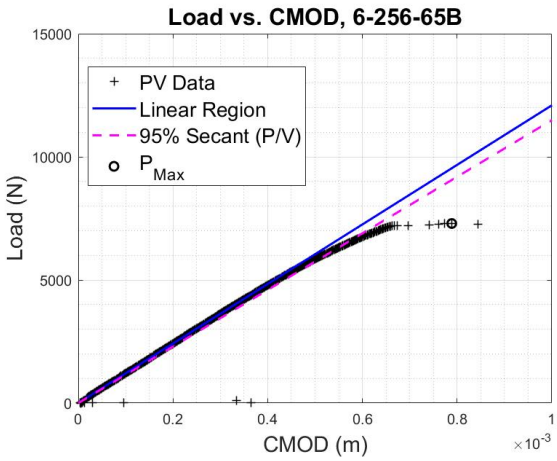
Load vs. CMOD, 6-256-65B
PV Data
Linear Region
95% Secant (P/V)
P Max
Load (N)
CMOD (m)
×10-3

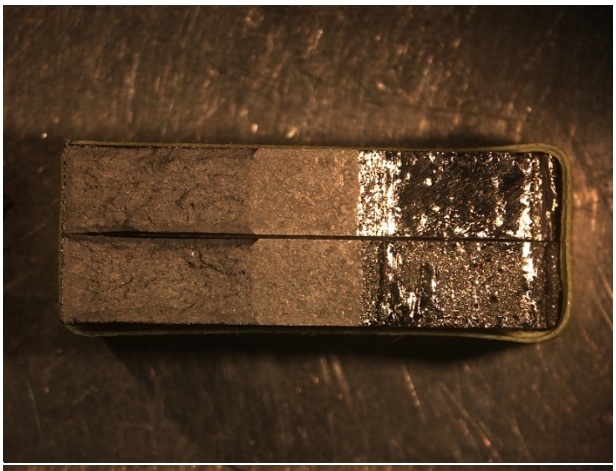

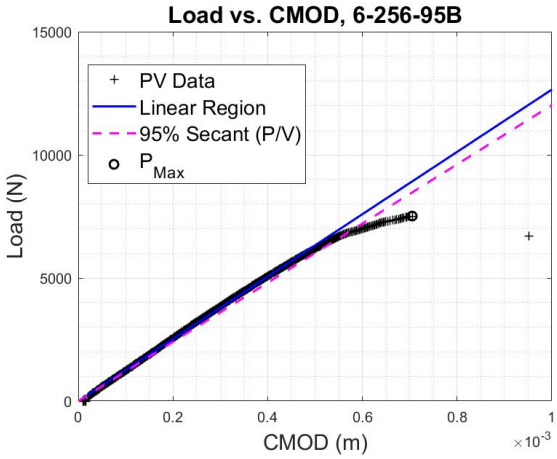
Load vs. CMOD, 6-256-95B
PV Data
Linear Region
95% Secant (P/V)
P Max
Load (N)
CMOD (m)
×10-3

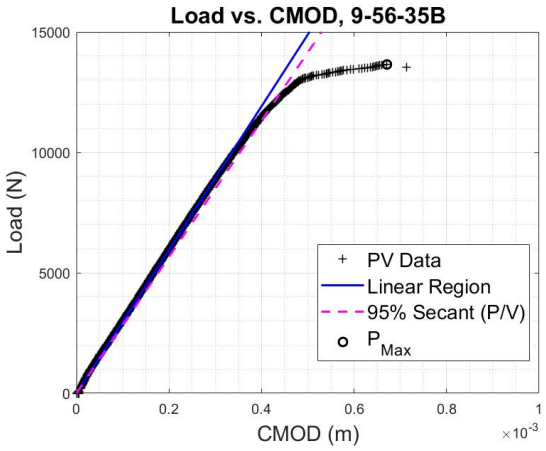
Load vs. CMOD, 9-56-35B
PV Data
Linear Region
95% Secant (P/V)
P Max
Load (N)
CMOD (m)
×10-3

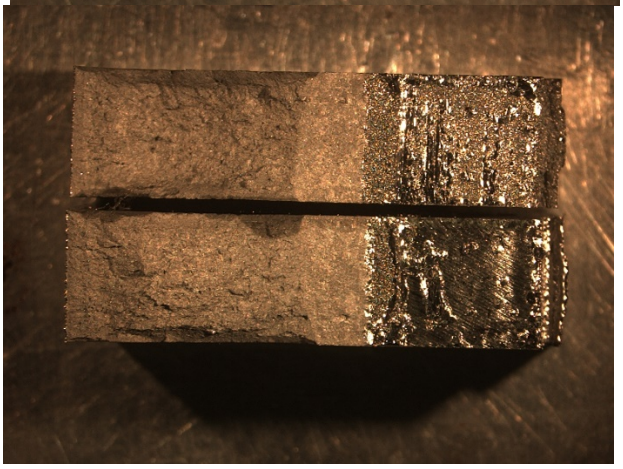

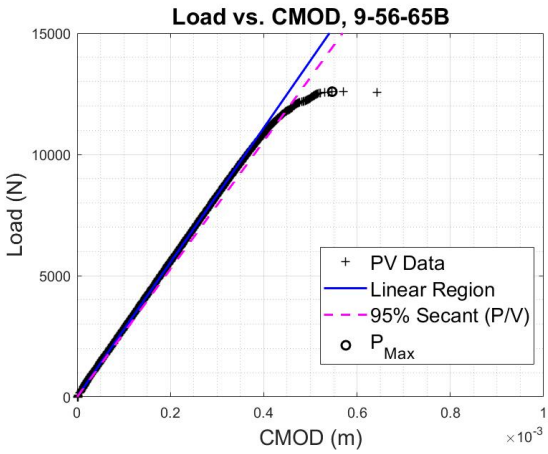
Load vs. CMOD, 9-56-65B
Load (N)
CMOD (m)
×10^-3
PV Data
Linear Region
95% Secant (P/V)
P Max

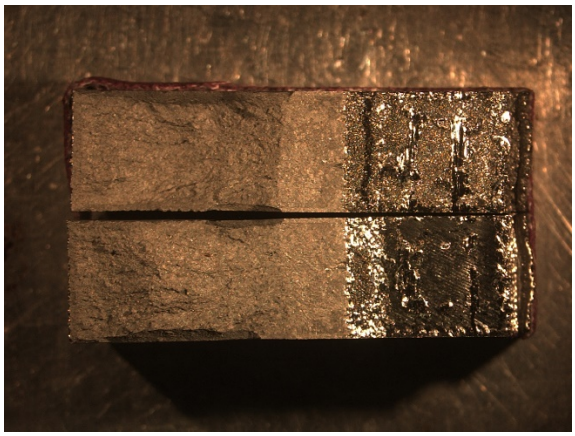

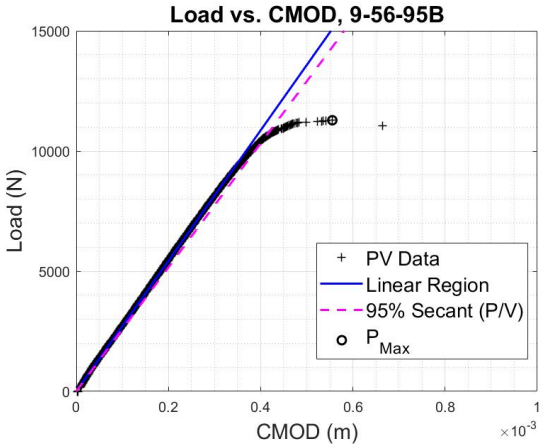
Load vs. CMOD, 9-56-95B
Load (N)
CMOD (m)
×10^-3
PV Data
Linear Region
95% Secant (P/V)
P Max

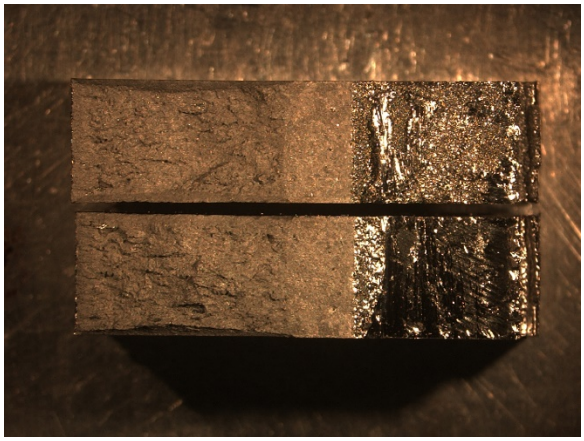

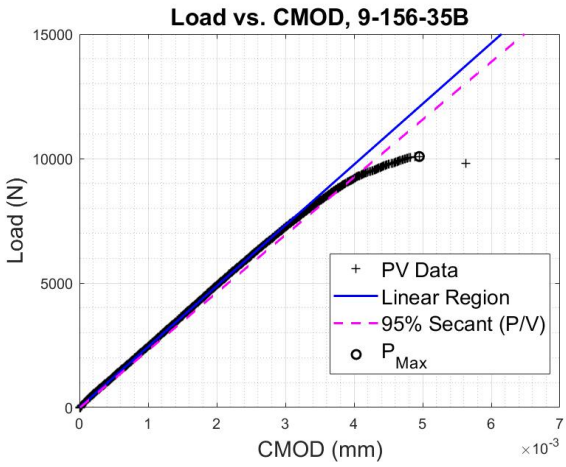
Load vs. CMOD, 9-156-35B
Load (N)
CMOD (mm)
×10^-3
PV Data
Linear Region
95% Secant (P/V)
P Max

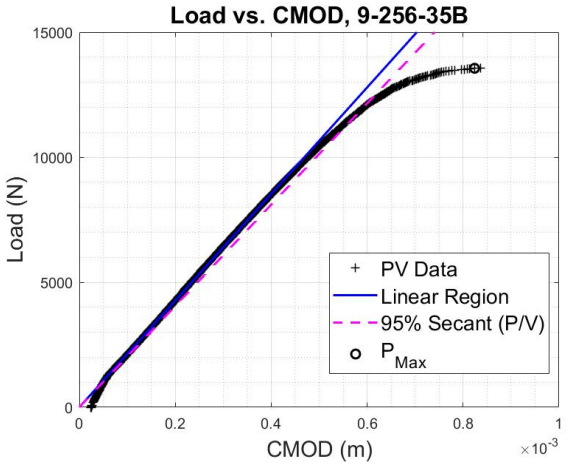
Load vs. CMOD, 9-256-35B
Load (N)
CMOD (m)
×10^-3
PV Data
Linear Region
95% Secant (P/V)
P Max

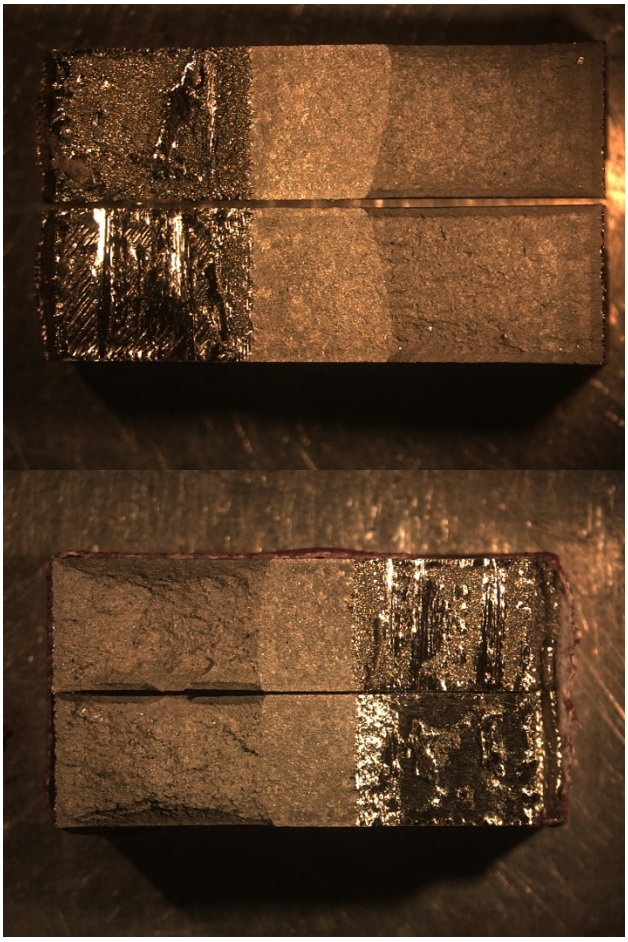

Kr Curves (Machined)

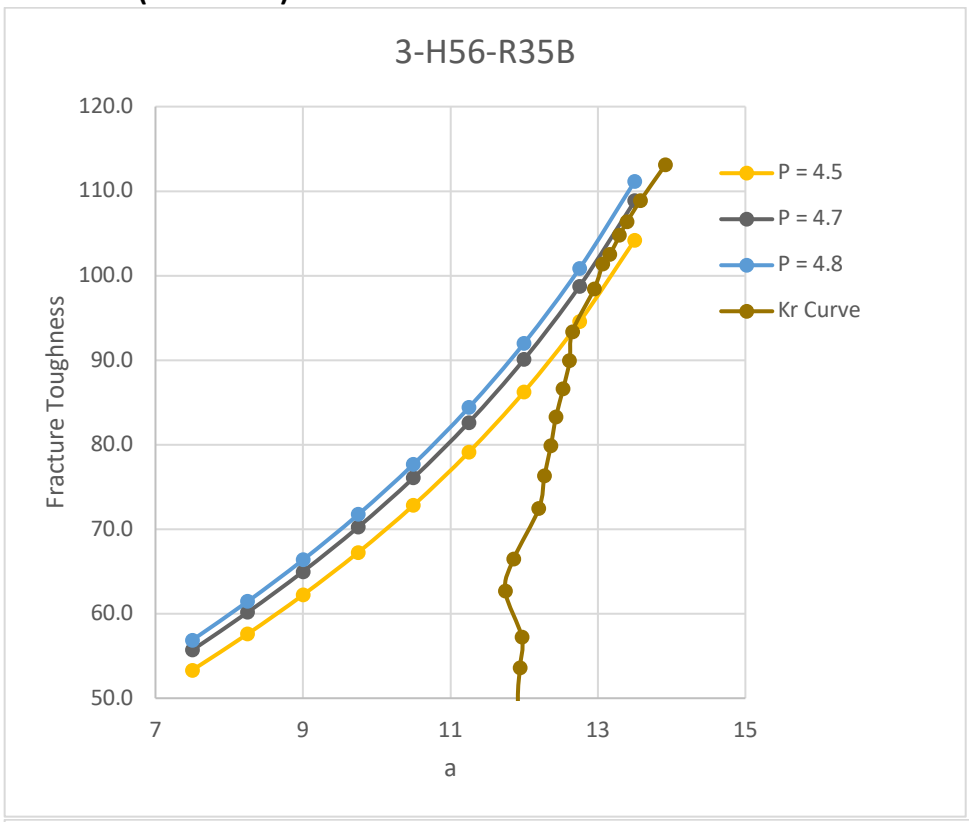

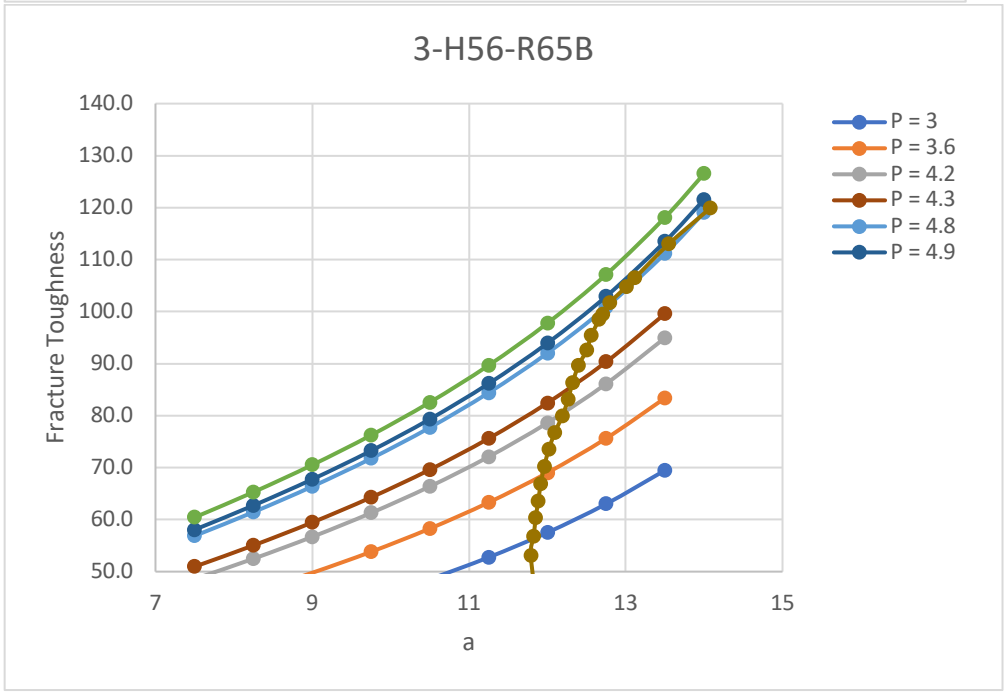

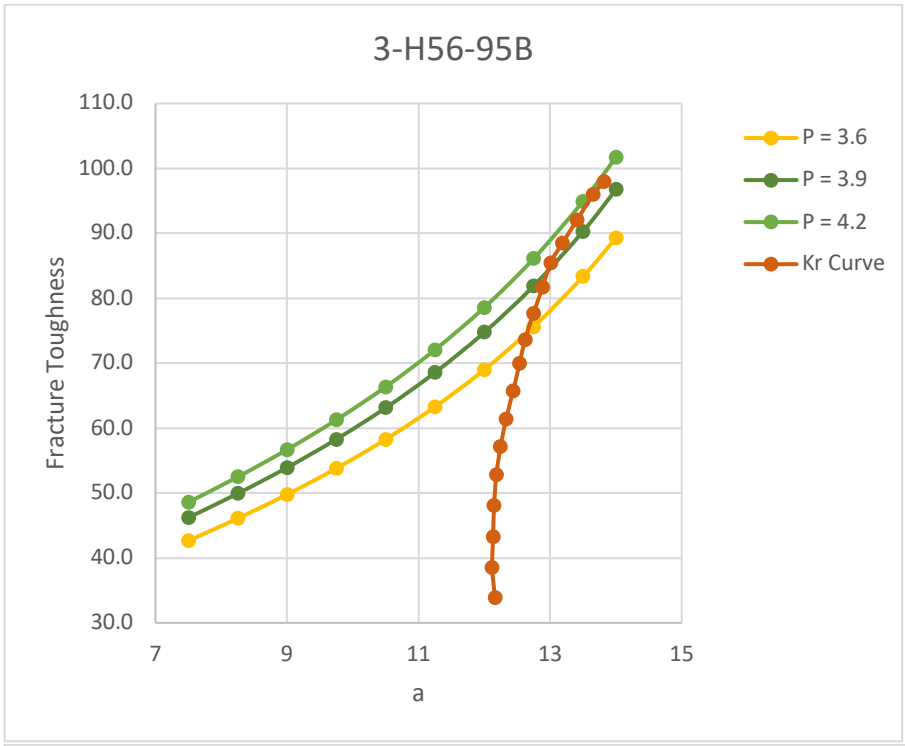
3-H56-95B
Fracture Toughness
110.0
100.0
90.0
80.0
70.0
60.0
50.0
40.0
30.0
7
9
11
13
15
a
P = 3.6
P = 3.9
P = 4.2
Kr Curve

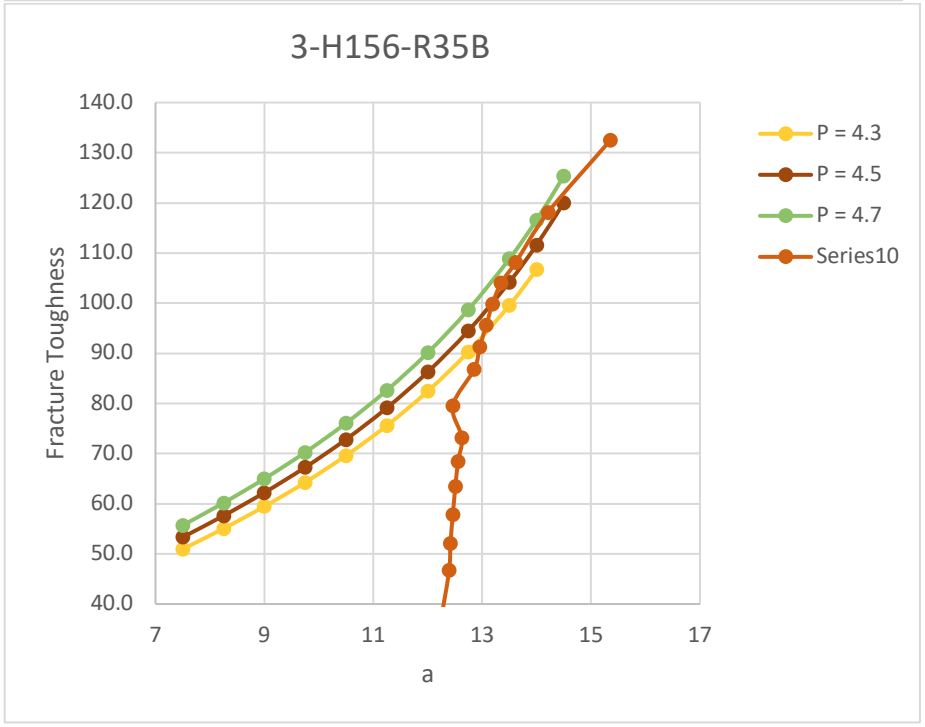
3-H156-R35B
Fracture Toughness
140.0
130.0
120.0
110.0
100.0
90.0
80.0
70.0
60.0
50.0
40.0
7
9
11
13
15
17
a
P = 4.3
P = 4.5
P = 4.7
Series10

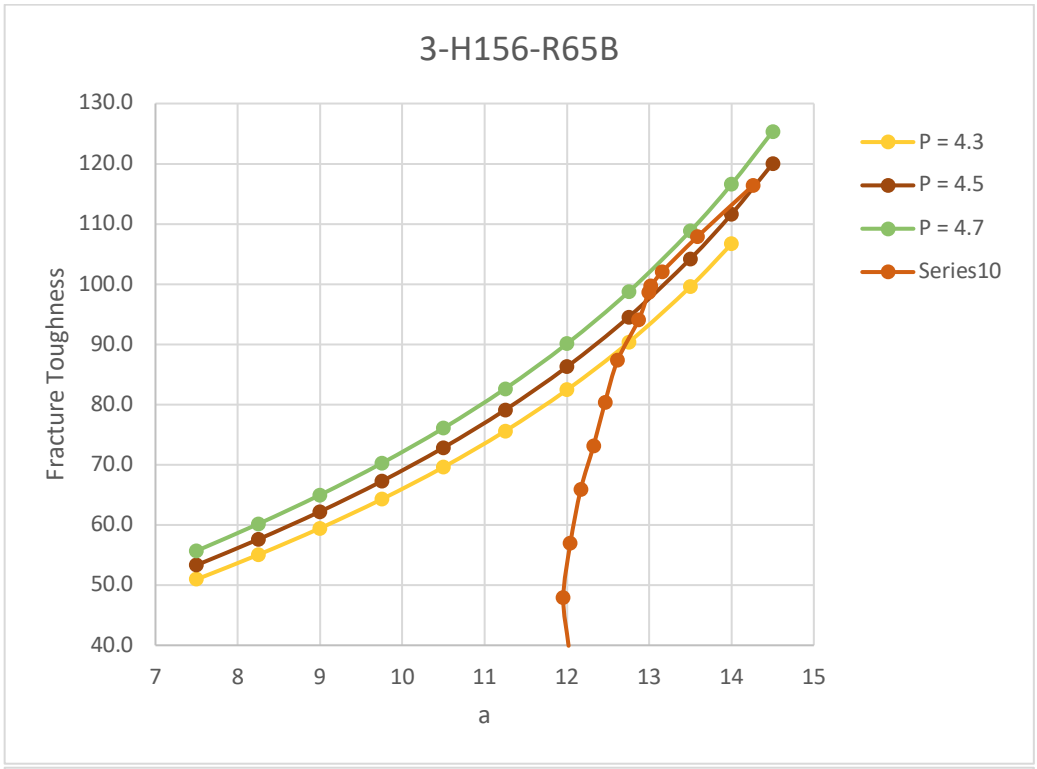
3-H156-R65B
Fracture Toughness
a
130.0
120.0
110.0
100.0
90.0
80.0
70.0
60.0
50.0
40.0
7
8
9
10
11
12
13
14
15
P = 4.3
P = 4.5
P = 4.7
Series10

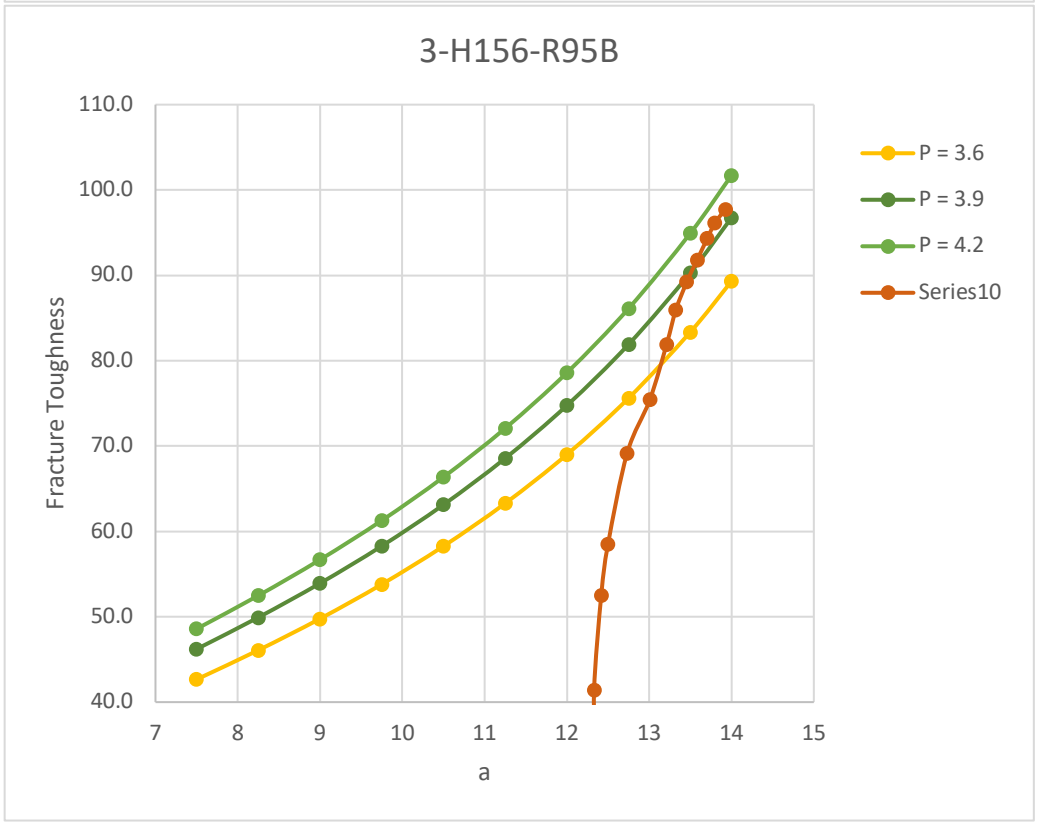
3-H156-R95B
Fracture Toughness
a
110.0
100.0
90.0
80.0
70.0
60.0
50.0
40.0
7
8
9
10
11
12
13
14
15
P = 3.6
P = 3.9
P = 4.2
Series10

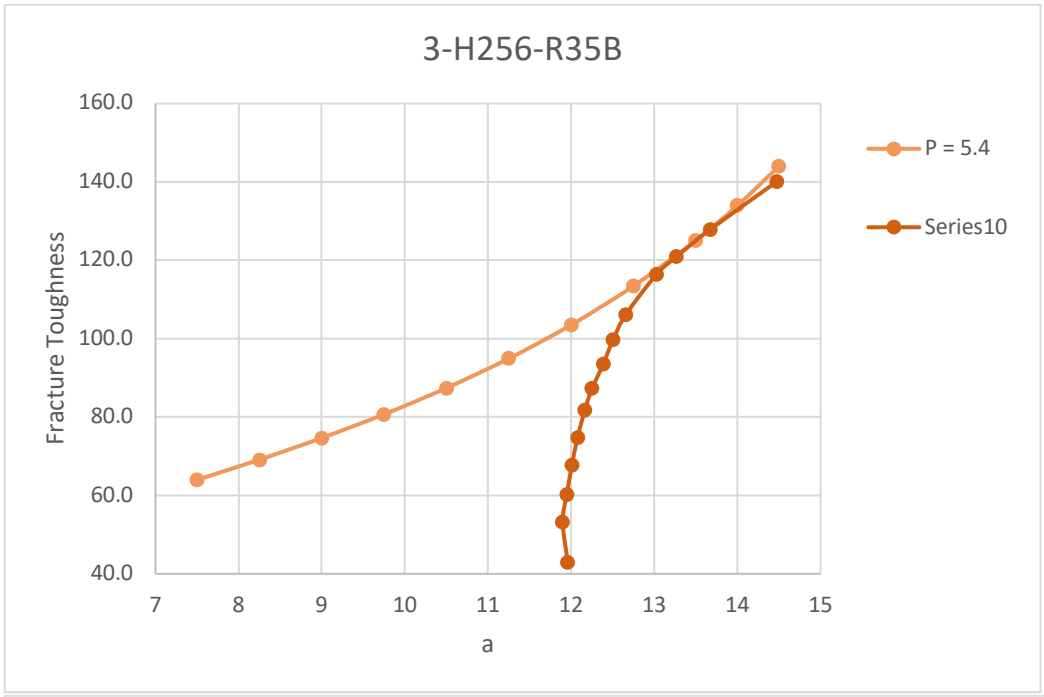
3-H256-R35B
160.0
140.0
120.0
100.0
80.0
60.0
40.0
Fracture Toughness
7
8
9
10
11
12
13
14
15
a
P = 5.4
Series10

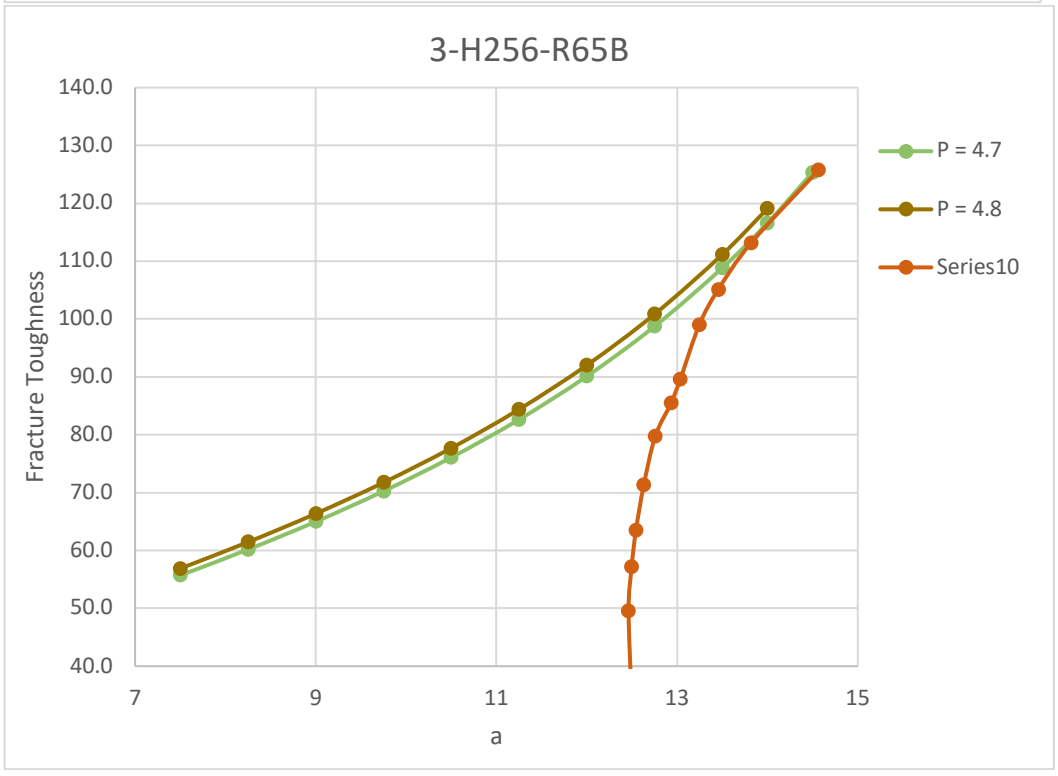
3-H256-R65B
140.0
130.0
120.0
110.0
100.0
90.0
80.0
70.0
60.0
50.0
40.0
Fracture Toughness
7
9
11
13
15
a
P = 4.7
P = 4.8
Series10

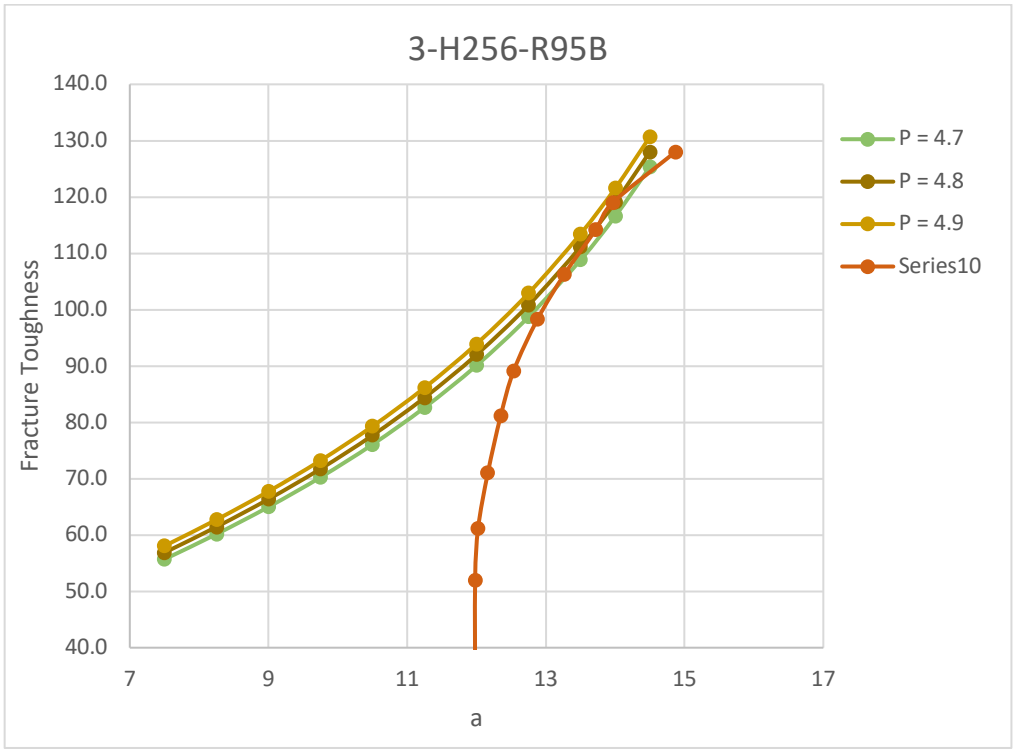
3-H256-R95B
140.0
130.0
120.0
110.0
100.0
90.0
80.0
70.0
60.0
50.0
40.0
Fracture Toughness
7
9
11
13
15
17
a
P = 4.7
P = 4.8
P = 4.9
Series10

Fracture Toughness Results Table (Machined)

Specimen (t_h_r)	Thickness before machining (mm)	Thickness after machining (mm)	radial	height	Crack Length (from notch)(mm	Crack Length from pin (mm)	a/W	Kq (Mpa(m)^0.5)	Kic(Mpa(m)^0.5)	Kc(Mpa(m)^0.5)
3_56_35B	3	2.6	35	56	18.21145125	11.96145125	0.47845805	69.86	-	104
3_56_65B	3	2.6	65	56	18.1513179	11.9013179	0.47605272	75.88	-	98
3_56_95B	3	2.6	95	56	18.41061498	12.16061498	0.4864246	67.64	-	85
3_156_35B	3	2.6	35	156	18.63981391	12.38981391	0.49559256	74.98	-	108
3_156_65B	3	2.6	65	156	18.2715311	12.0215311	0.48086124	70.59	-	98
3_156_95B	3	2.6	95	156	18.59760988	12.34760988	0.4939044	64	-	92
3_256_35B	3	2.6	35	256	18.20652174	11.95652174	0.47826087	85.3	-	128
3_256_65B	3	2.6	65	256	18.75	12.5	0.5	78.6	-	116
3_256_95B	3	2.6	95	256	18.22665056	11.97665056	0.47906602	71.43	-	113
6_56_35B	6	5.35	35	56	19.29695182	13.04695182	0.52187807	58.52	-	-
6_56_65B	6	5.35	65	56	17.27965135	11.02965135	0.44118605	-	62.2	-
6_56_95B	6	5.35	95	56	18.56527094	12.31527094	0.49261084	53.5	-	-
6_156_35B	6	5.35	35	156	18.83603736	12.58603736	0.50344149	-	68.86	-
6_156_65B	6	5.35	65	156	17.94038273	11.69038273	0.46761531	-	66.94	-
6_156_95B	6	5.35	95	156	16.97120039	10.72120039	0.42884802	58.93	-	-
6_256_35B	6	5.35	35	256	19.82994042	13.57994042	0.54319762	81.3	-	-
6_256_65B	6	5.35	65	256	19.44105691	13.19105691	0.52764228	77.34	-	-
6_256_95B	6	5.35	95	256	18.80980861	12.55980861	0.50239234	72.8	-	-
9_56_35B	9	8.35	35	56	16.79546941	10.54546941	0.42181878	-	69.27	-
9_56_65B	9	8.35	65	56	17.09063616	10.84063616	0.43362545	-	70.1	-
9_56_95B	9	8.35	95	56	16.80205302	10.55205302	0.42208212	-	61.27	-
9_156_35B	9	8.35	35	156	19.03548714	12.78548714	0.51141949	-	68.28	-
9_156_65B	9	8.35	65	156	18.53567277	12.28567277	0.49142691	73.95	-	-
9_156_95B	9	8.35	95	156	17.98978644	11.73978644	0.46959146	-	63.22	-
9_256_35B	9	8.35	35	256	18.28748783	12.03748783	0.48149951	81.55	-	-
9_256_65B	9	8.35	65	256	#DIV/0!	#DIV/0!	#DIV/0!	Broke	Broke	Broke
9_256_95B	9	8.35	95	256	17.68032668	11.43032668	0.45721307	73.45	-	-

Appendix B: Machined+HT Fracture Toughness Data

Load vs Displacement Curves (Machined+HT)

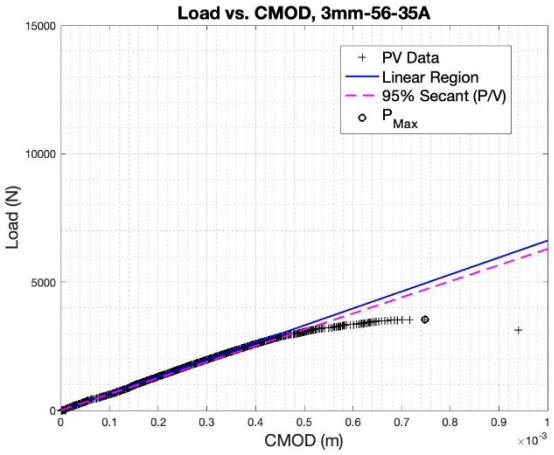

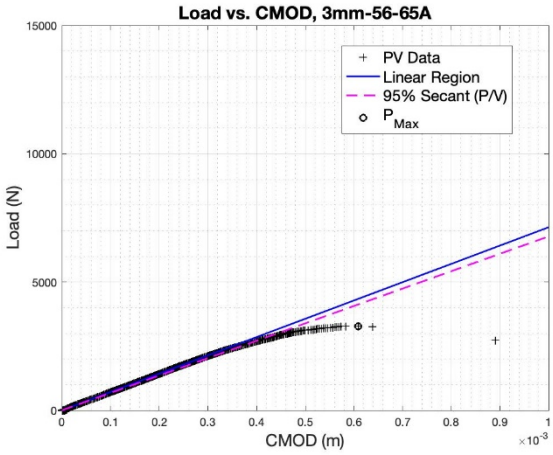

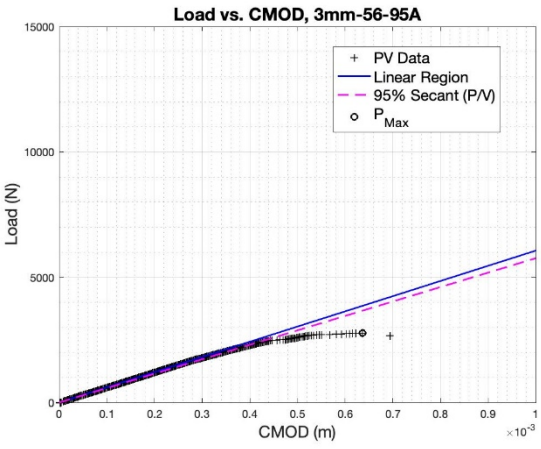

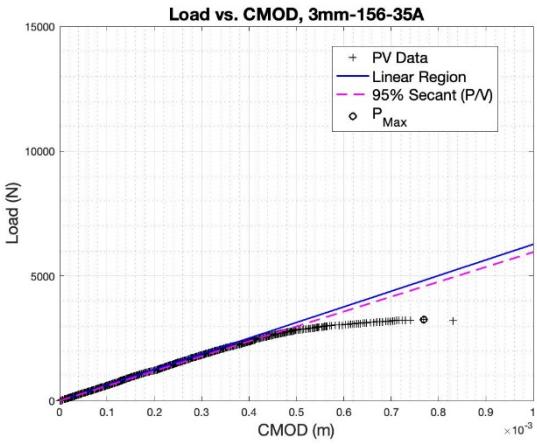

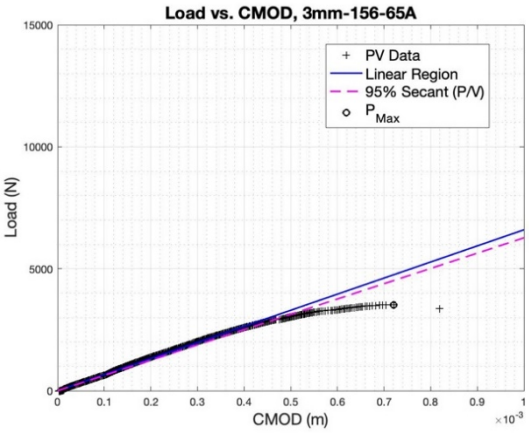

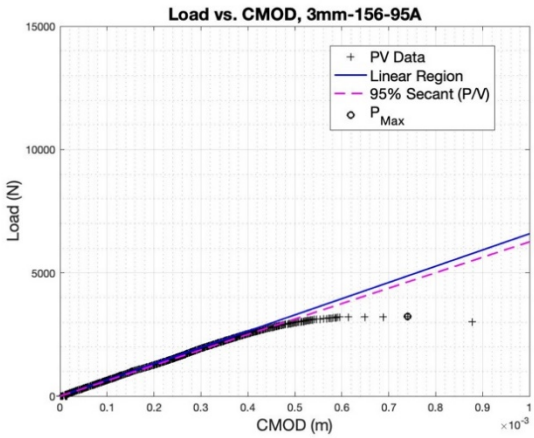
Load vs. CMOD, 3mm-156-95A
PV Data
Linear Region
95% Secant (P/V)
P Max
Load (N)
CMOD (m)
×10-3

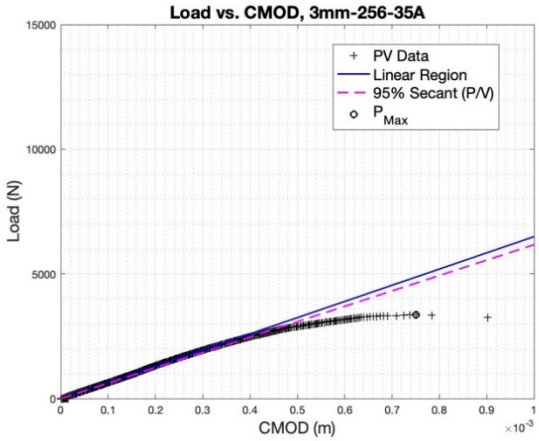
Load vs. CMOD, 3mm-256-35A
PV Data
Linear Region
95% Secant (P/V)
P Max
Load (N)
CMOD (m)
×10-3

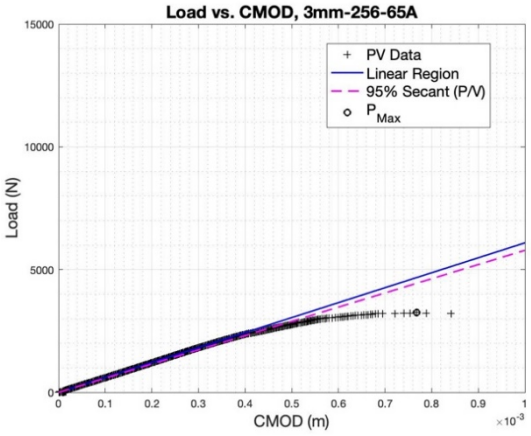
Load vs. CMOD, 3mm-256-65A
PV Data
Linear Region
95% Secant (P/V)
P Max
Load (N)
CMOD (m)
×10-3

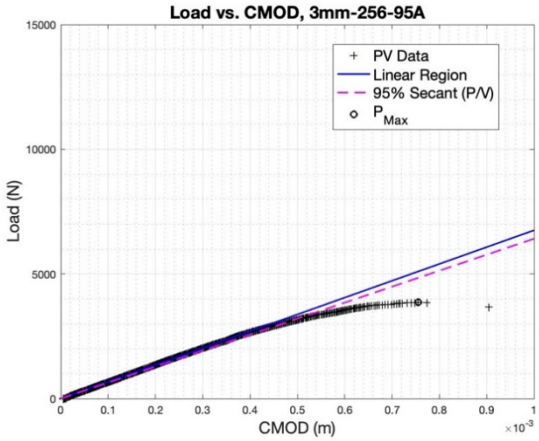
Load vs. CMOD, 3mm-256-95A
PV Data
Linear Region
95% Secant (P/V)
P Max
Load (N)
CMOD (m)
×10-3

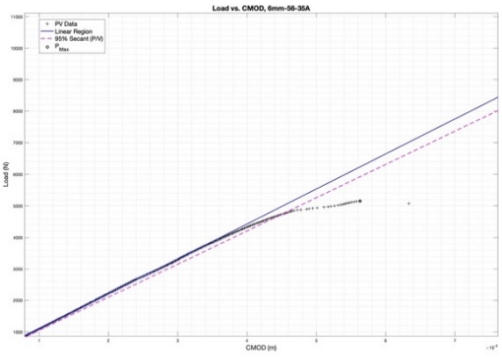
Load vs. CMOD, 6mm-56-35A

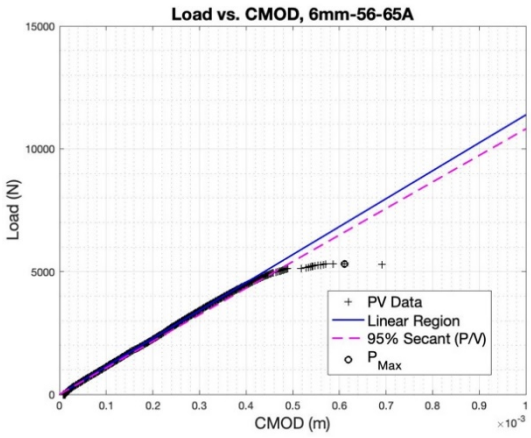
Load vs. CMOD, 6mm-56-65A
Load (N)
CMOD (m)
PV Data
Linear Region
95% Secant (P/V)
P Max

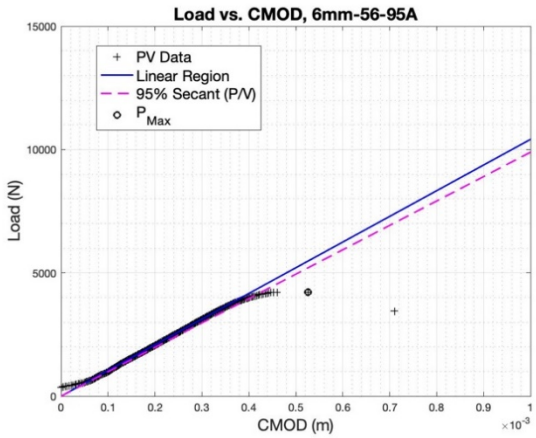
Load vs. CMOD, 6mm-56-95A
Load (N)
CMOD (m)
PV Data
Linear Region
95% Secant (P/V)
P Max

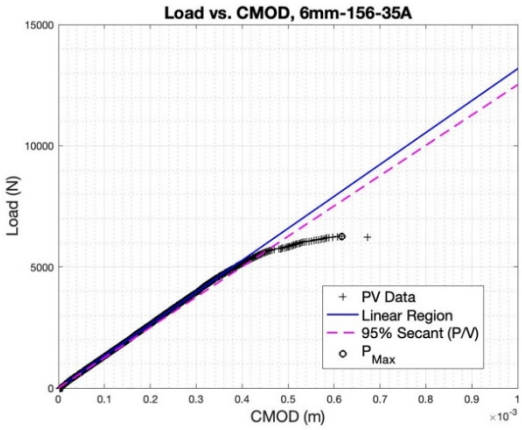
Load vs. CMOD, 6mm-156-35A
Load (N)
CMOD (m)
PV Data
Linear Region
95% Secant (P/V)
P Max

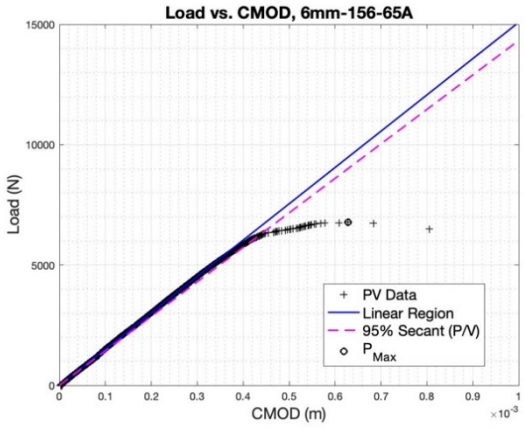
Load vs. CMOD, 6mm-156-65A
Load (N)
CMOD (m)
PV Data
Linear Region
95% Secant (P/V)
P Max

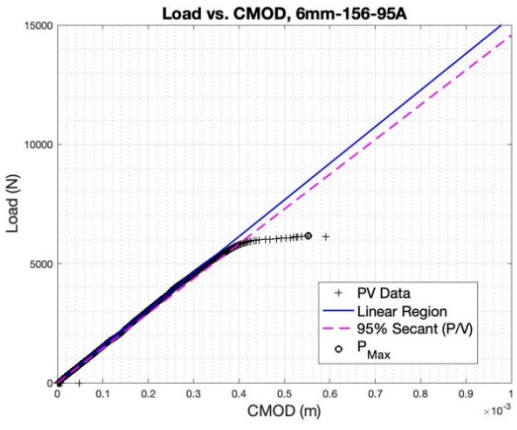
Load vs. CMOD, 6mm-156-95A
Load (N)
CMOD (m)
PV Data
Linear Region
95% Secant (P/V)
P Max

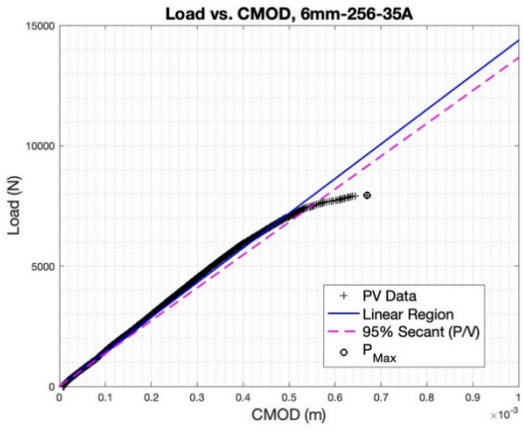
Load vs. CMOD, 6mm-256-35A
Load (N)
CMOD (m)
PV Data
Linear Region
95% Secant (P/V)
P Max

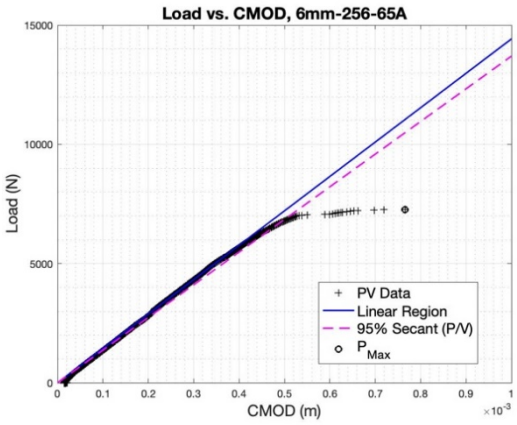
Load vs. CMOD, 6mm-256-65A
Load (N)
CMOD (m)
PV Data
Linear Region
95% Secant (P/V)
P Max

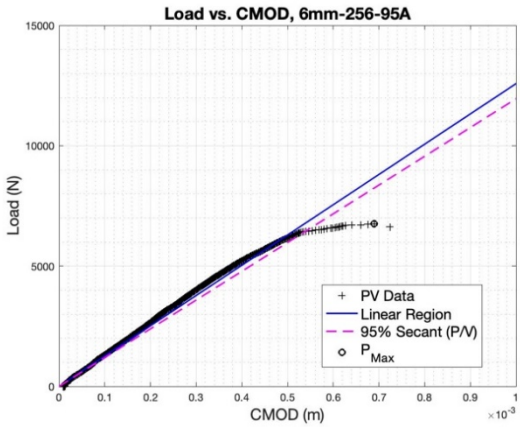
Load vs. CMOD, 6mm-256-95A
Load (N)
CMOD (m)
PV Data
Linear Region
95% Secant (P/V)
P Max

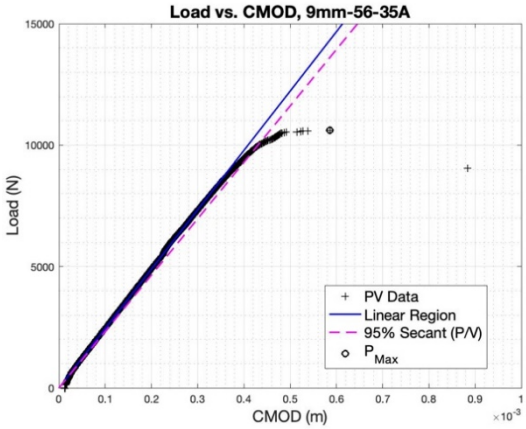
Load vs. CMOD, 9mm-56-35A
Load (N)
CMOD (m)
PV Data
Linear Region
95% Secant (P/V)
P Max

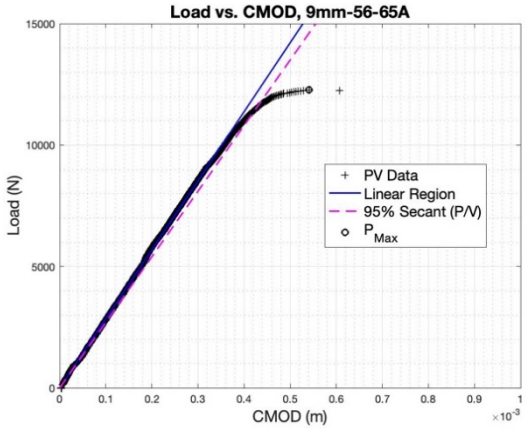
Load vs. CMOD, 9mm-56-65A
Load (N)
CMOD (m)
PV Data
Linear Region
95% Secant (P/V)
P Max

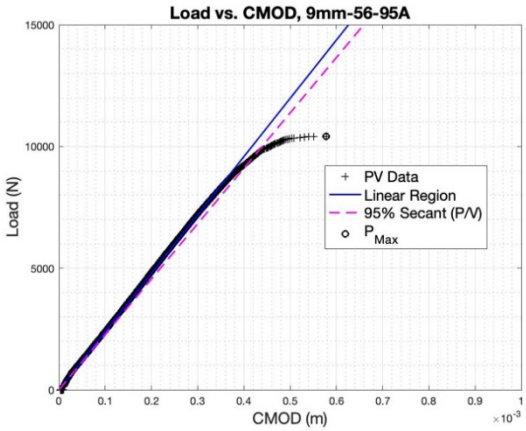
Load vs. CMOD, 9mm-56-95A
Load (N)
CMOD (m)
PV Data
Linear Region
95% Secant (P/V)
P Max

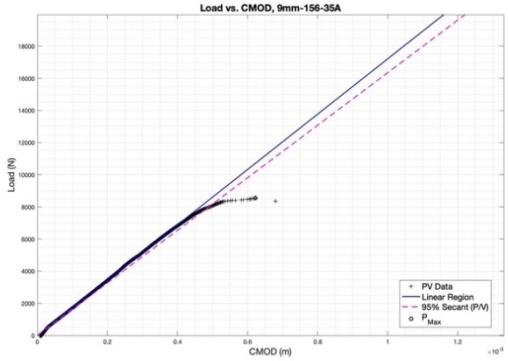
Load vs. CMOD, 9mm-156-35A
Load (N)
CMOD (m)
PV Data
Linear Region
95% Secant (P/V)
P Max

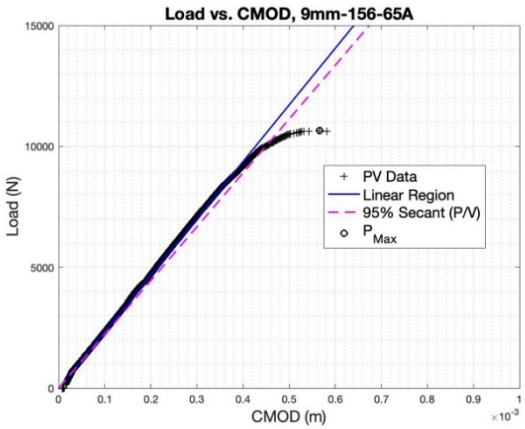
Load vs. CMOD, 9mm-156-65A
Load (N)
CMOD (m)
PV Data
Linear Region
95% Secant (P/V)
P Max

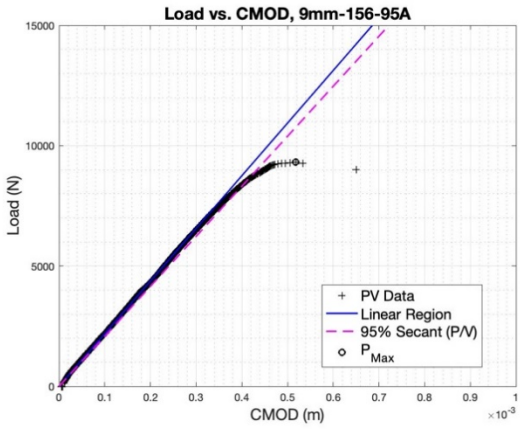
Load vs. CMOD, 9mm-156-95A
Load (N)
CMOD (m)
PV Data
Linear Region
95% Secant (P/V)
P Max

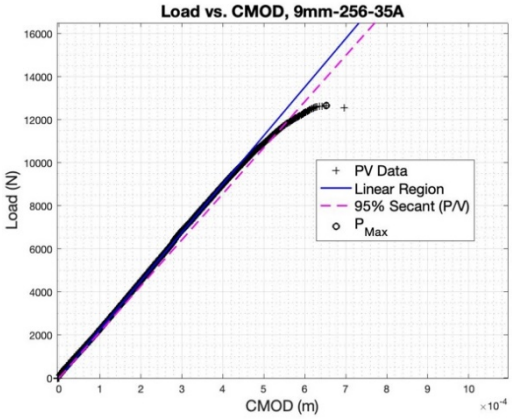
Load vs. CMOD, 9mm-256-35A
Load (N)
CMOD (m)
PV Data
Linear Region
95% Secant (P/V)
P Max

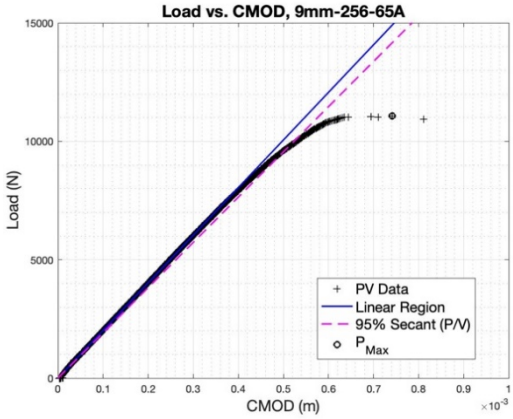
Load vs. CMOD, 9mm-256-65A
Load (N)
CMOD (m)
PV Data
Linear Region
95% Secant (P/V)
P Max

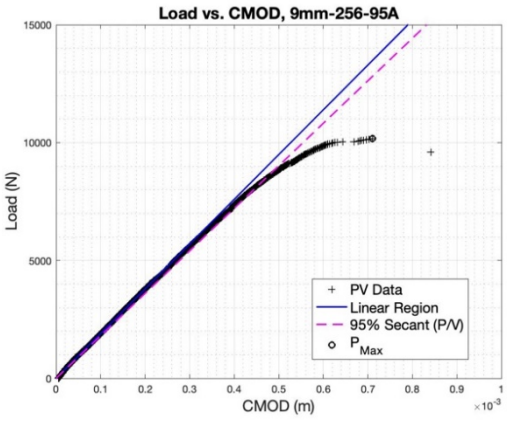
Load vs. CMOD, 9mm-256-95A
Load (N)
CMOD (m)
PV Data
Linear Region
95% Secant (P/V)
P Max

Kr Curves (Machined+HT)

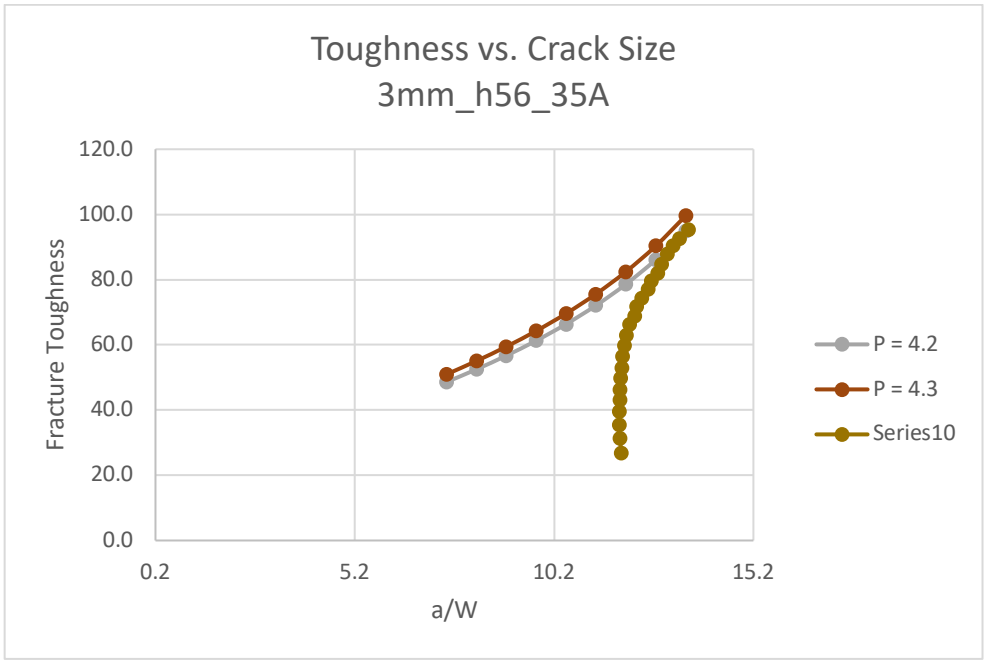

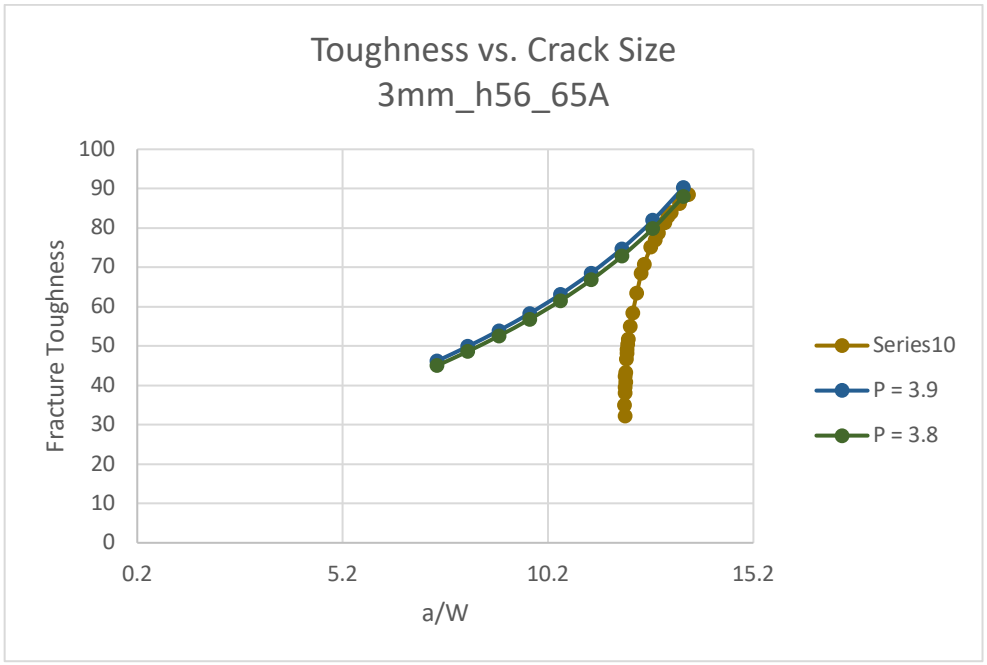

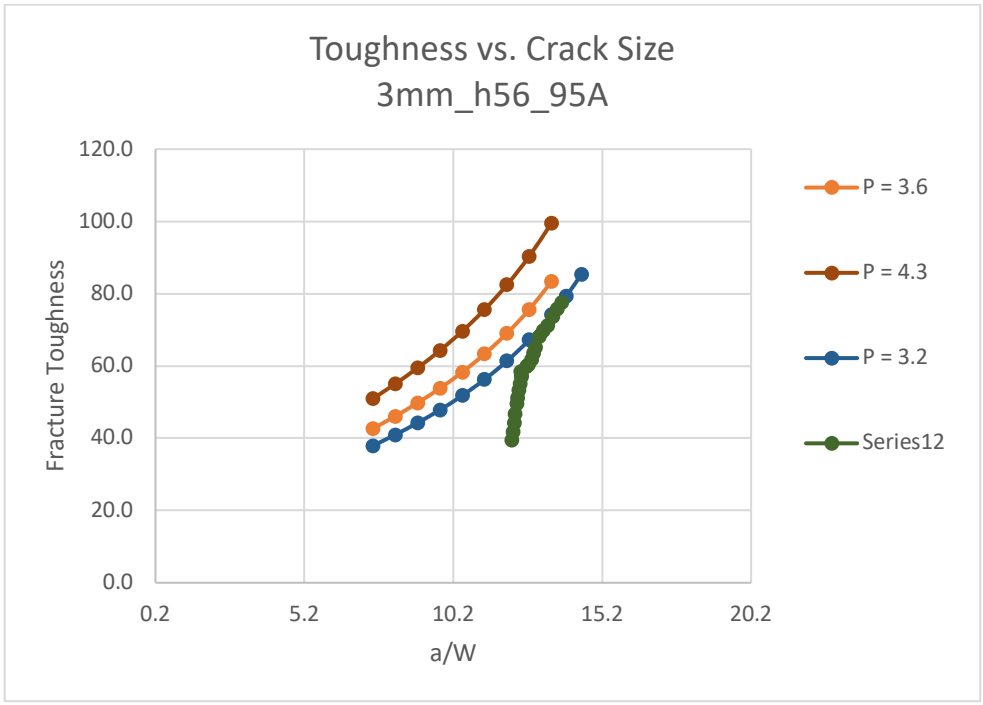
Toughness vs. Crack Size
3mm_h56_95A
Fracture Toughness
120.0
100.0
80.0
60.0
40.0
20.0
0.0
0.2
5.2
10.2
15.2
20.2
a/W
P = 3.6
P = 4.3
P = 3.2
Series12

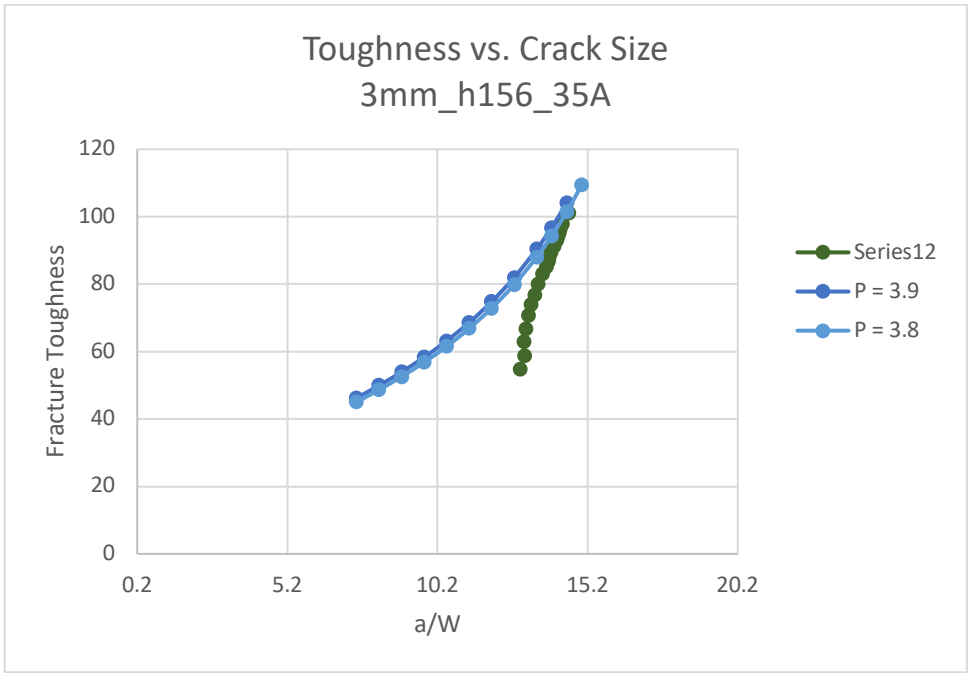
Toughness vs. Crack Size
3mm_h156_35A
Fracture Toughness
120
100
80
60
40
20
0
0.2
5.2
10.2
15.2
20.2
a/W
Series12
P = 3.9
P = 3.8

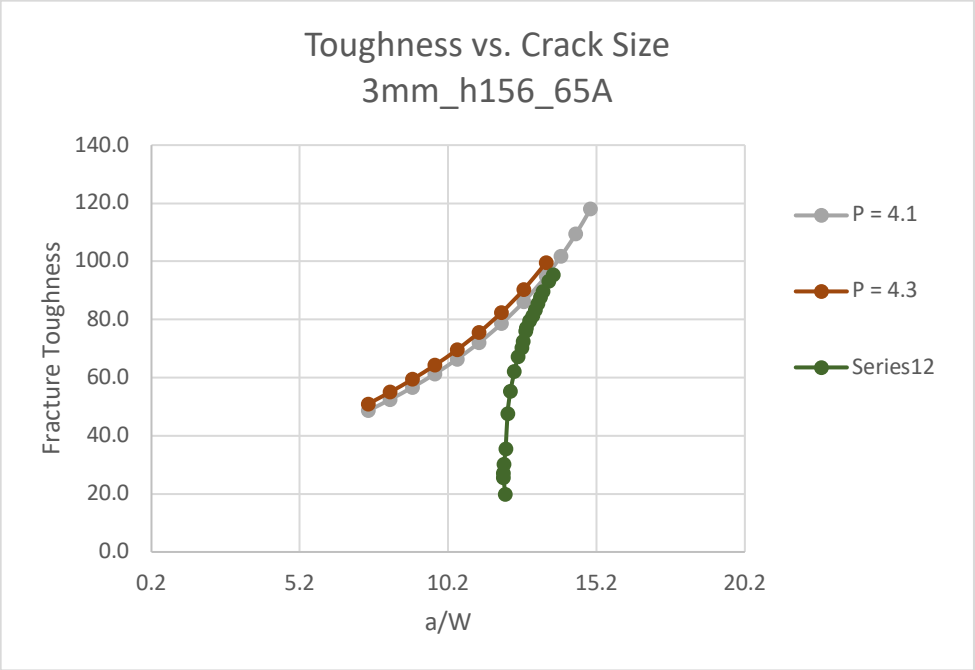
Toughness vs. Crack Size
3mm_h156_65A
Fracture Toughness
140.0
120.0
100.0
80.0
60.0
40.0
20.0
0.0
0.2
5.2
10.2
15.2
20.2
a/W
P = 4.1
P = 4.3
Series12


Toughness vs. Crack Size
3mm_h156_95A
Fracture Toughness
120.0
100.0
80.0
60.0
40.0
20.0
0.0
0.2
5.2
10.2
15.2
20.2
a/W
P = 3.6
Series12
P = 3.7

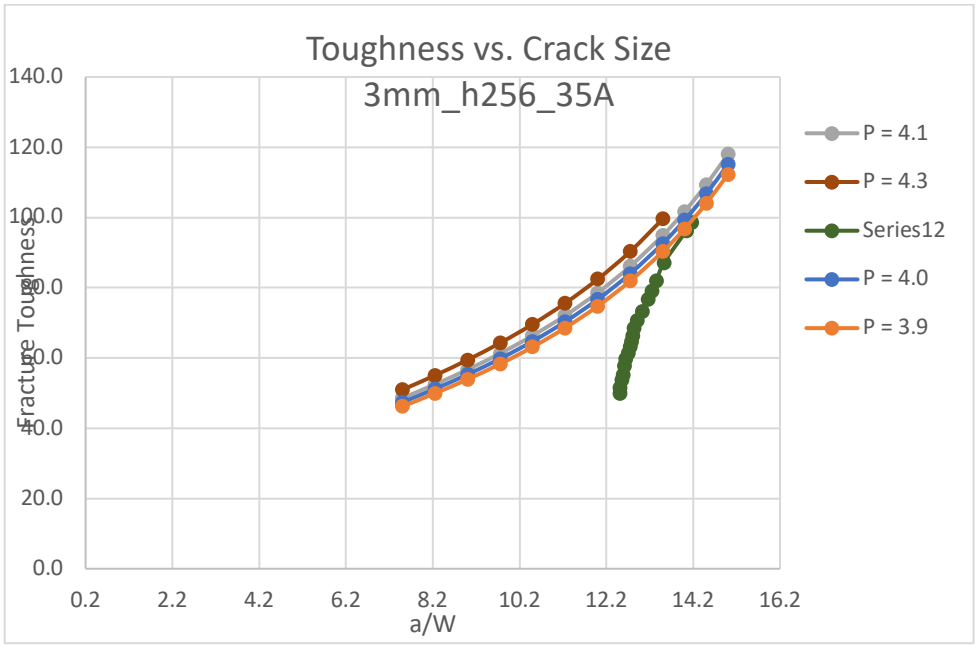
Toughness vs. Crack Size
3mm_h256_35A
Fracture Toughness
a/W
140.0
120.0
100.0
80.0
60.0
40.0
20.0
0.0
0.2
2.2
4.2
6.2
8.2
10.2
12.2
14.2
16.2
P = 4.1
P = 4.3
Series12
P = 4.0
P = 3.9

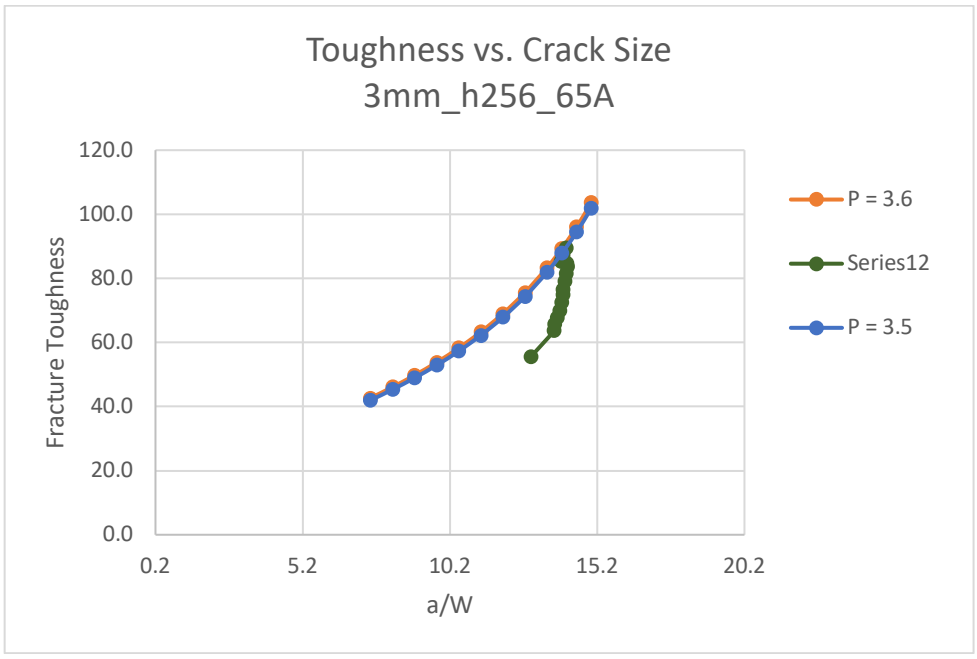
Toughness vs. Crack Size
3mm_h256_65A
Fracture Toughness
a/W
120.0
100.0
80.0
60.0
40.0
20.0
0.0
0.2
5.2
10.2
15.2
20.2
P = 3.6
Series12
P = 3.5

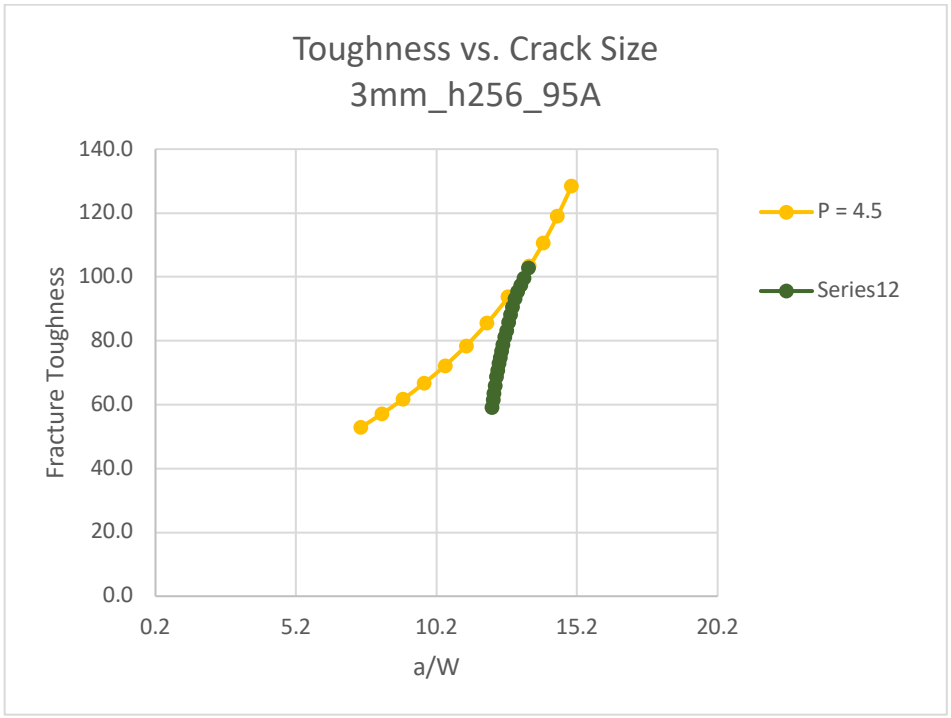
Toughness vs. Crack Size
3mm_h256_95A
140.0
120.0
100.0
80.0
60.0
40.0
20.0
0.0
Fracture Toughness
0.2
5.2
10.2
15.2
20.2
a/W
P = 4.5
Series12

Optical Microscope Fracture Surface Images (Machined+HT)

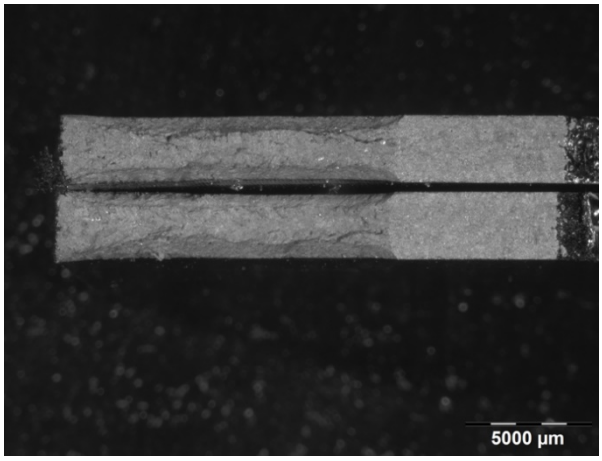

3mm_h56_35A

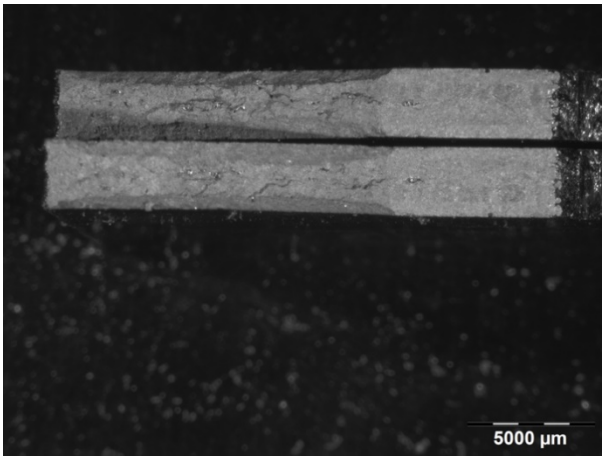

3mm_h56_65A

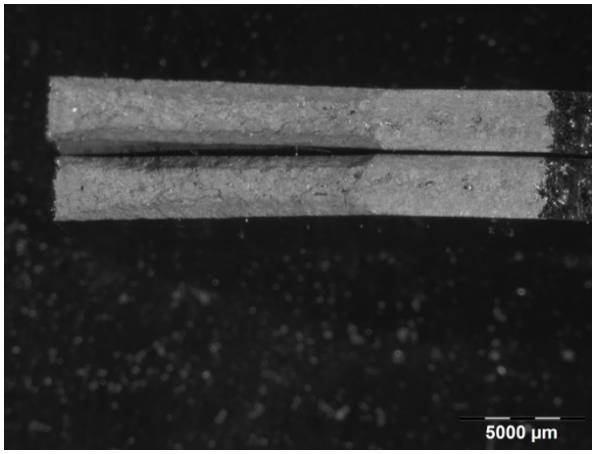

3mm_h56_95A

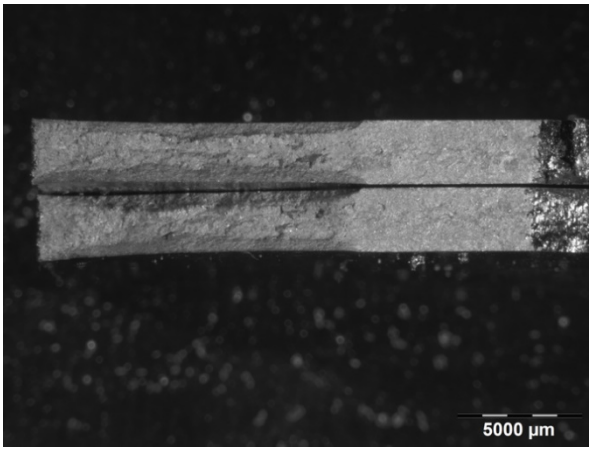

3mm_h156_35A

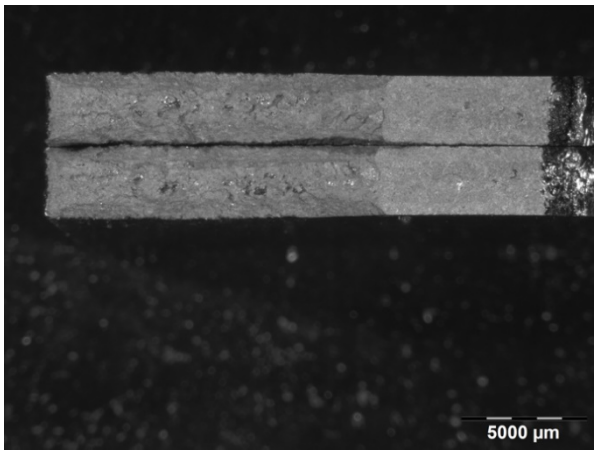

3mm_h156_65A

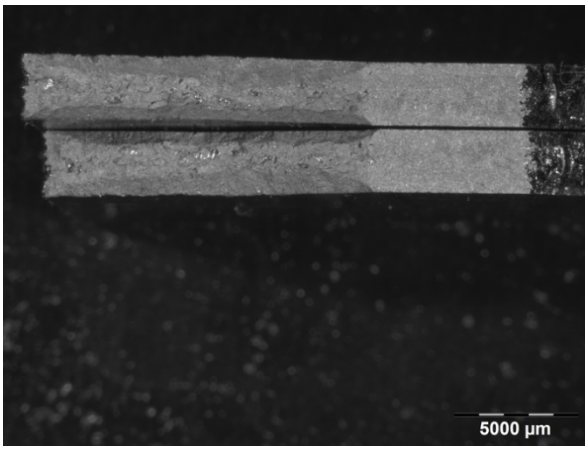

3mm_h156_95A

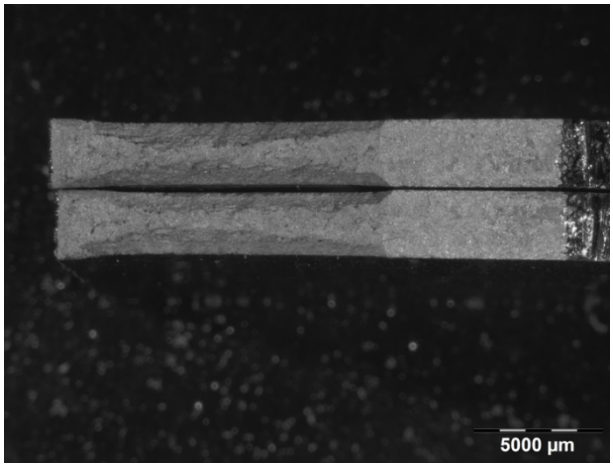

3mm_h256_35A

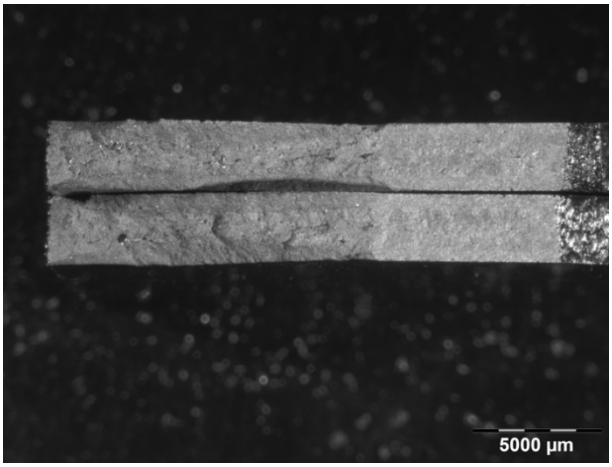

3mm_h256_65A

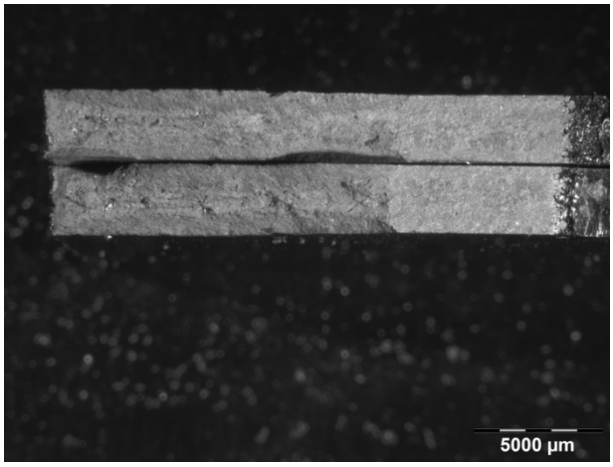

3mm_h256_95A

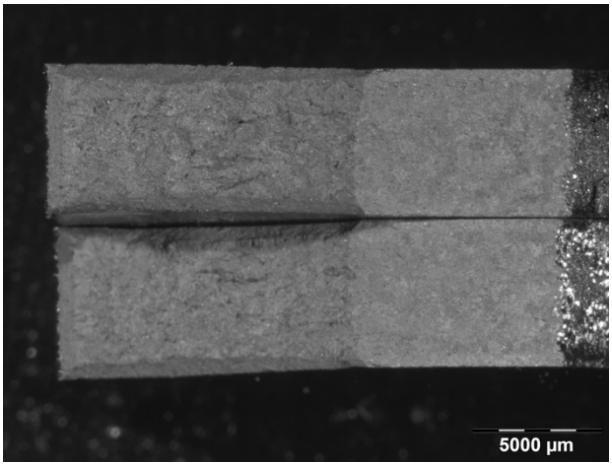

6mm_h56_35A

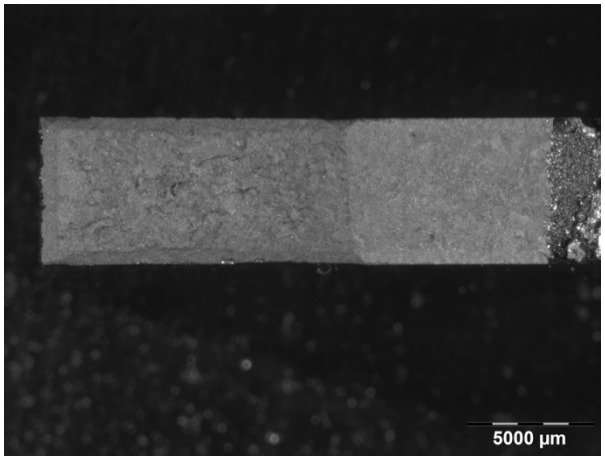

6mm_h56_65A

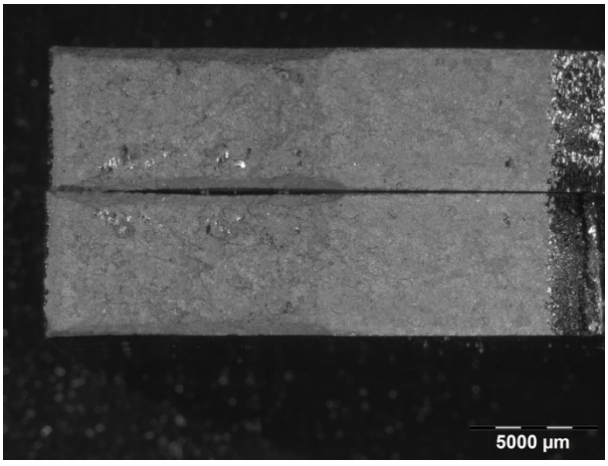

6mm_h56_95A

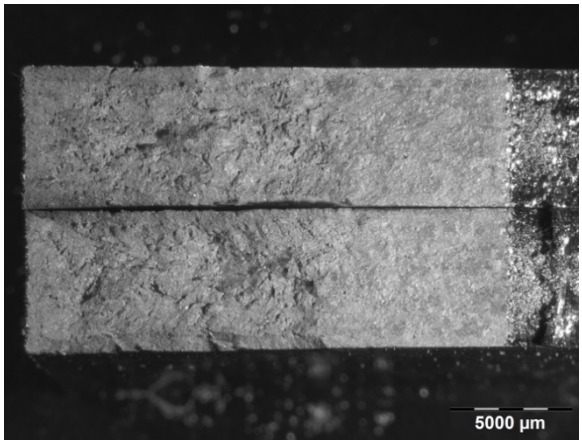

6mm_h156_35A

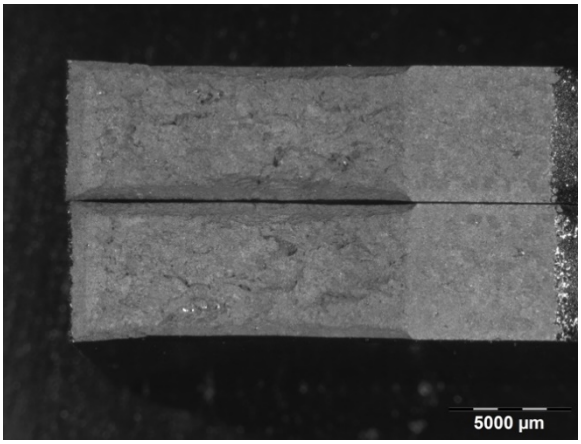

6mm_h156_65A

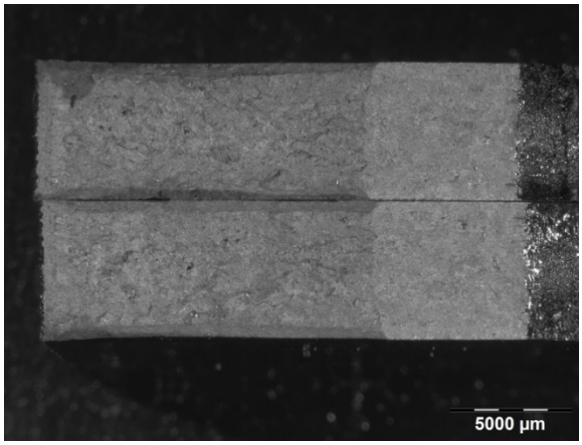

6mm_h156_95A

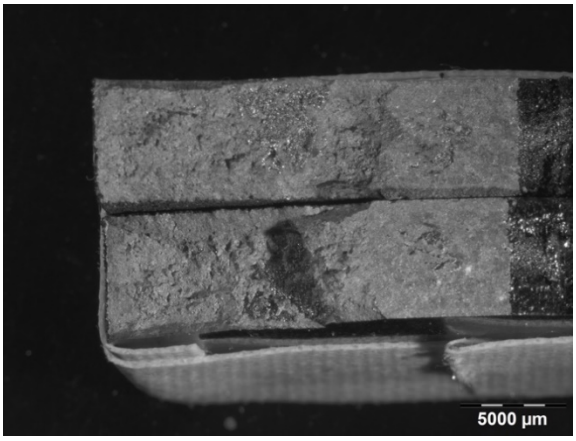

6mm_h256_35A

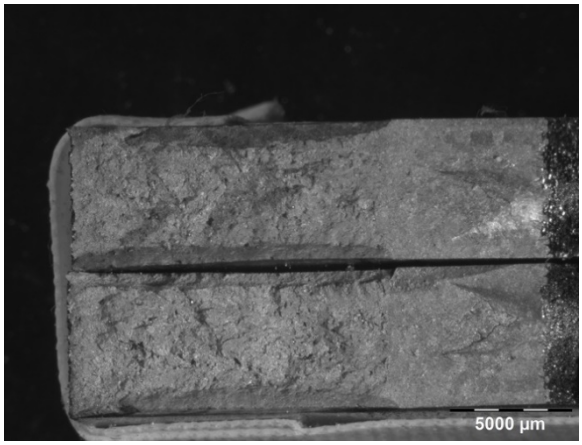

6mm_h256_65A

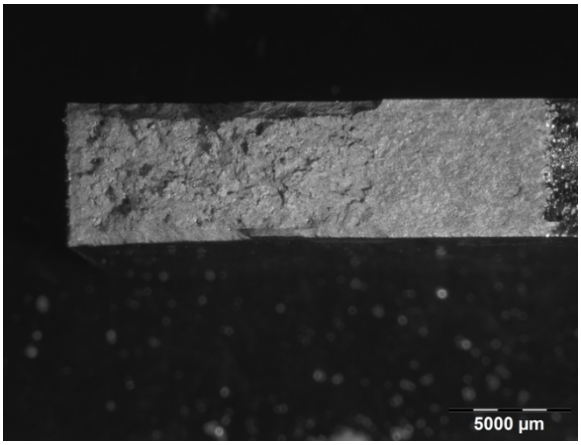

6mm_h256_95A

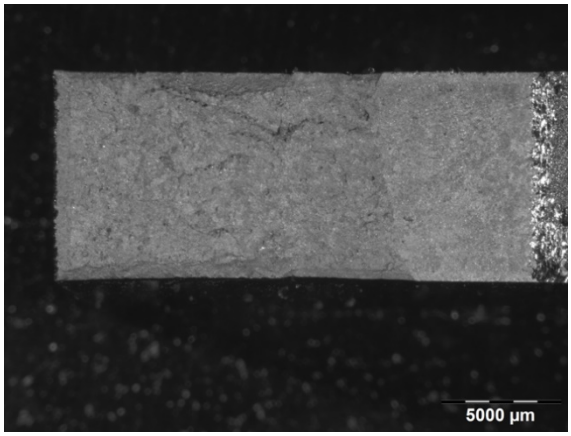

9mm_h56_35A

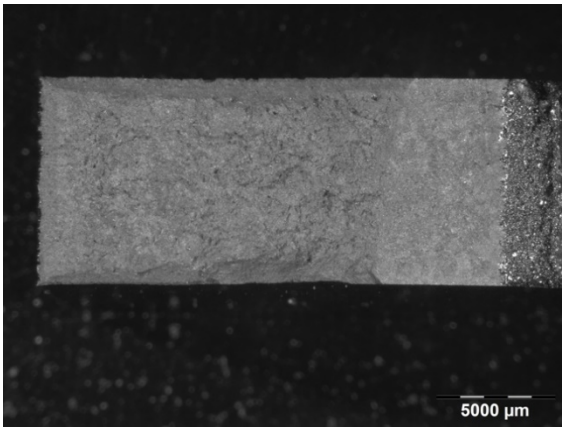

9mm_h56_65A

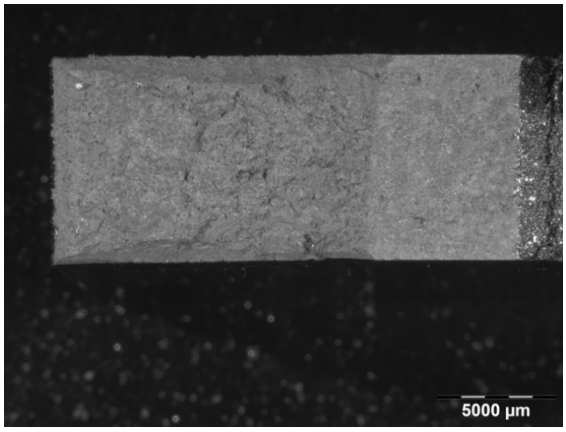

9mm_h56_95A

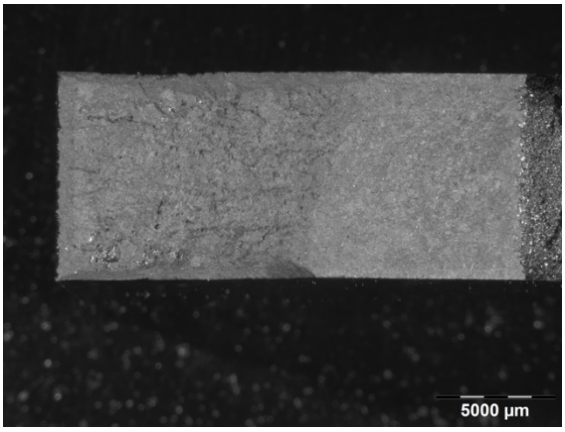

9mm_h156_35A

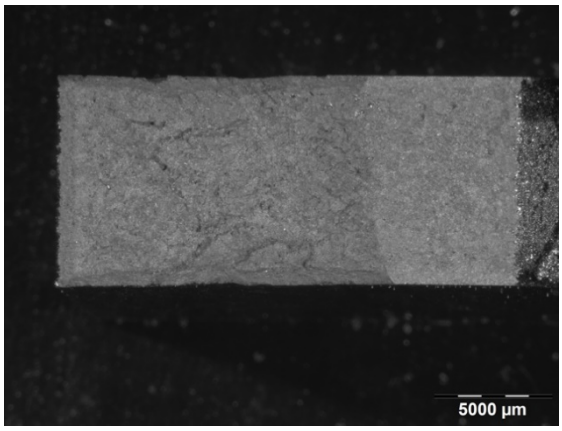

9mm_h156_65A

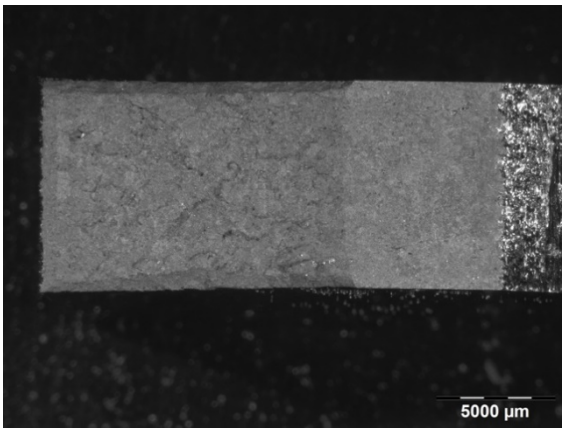

9mm_h156_95A

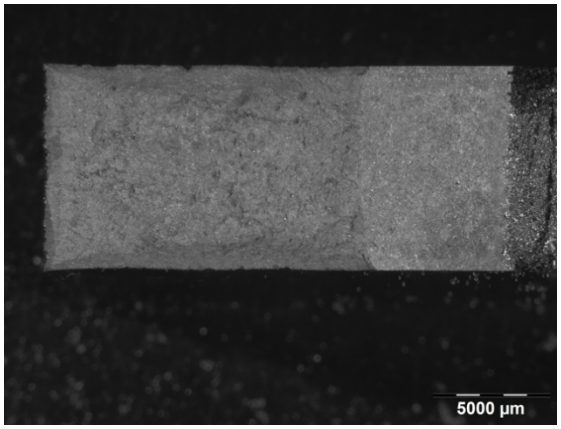

9mm_h256_35A

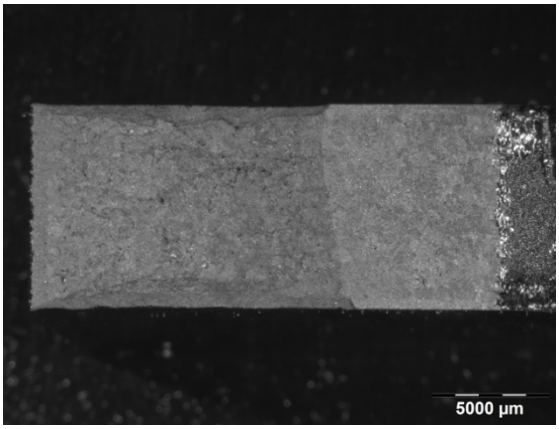

9mm_h256_65A

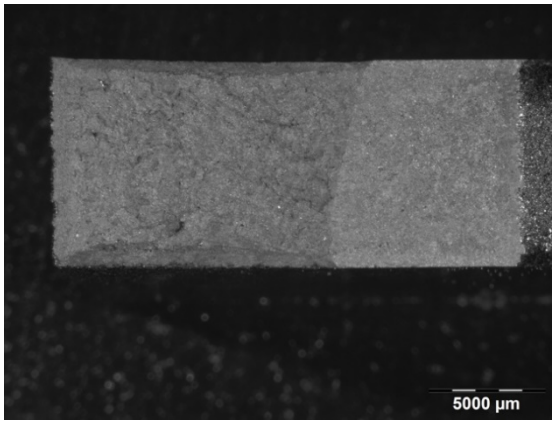

9mm_h256_95

Fracture Toughness Results (Machined+HT)

Specimen (t_h_r)	thickness before machining (mm)	thickness after machining(mm)	radial (mm)	height (mm)	Crack Length (from notch) (mm)	Crack Length from pin (mm)	a/W	Kq (Mpa(m)^0.5)	Kic (Mpa(m)^0.5)	Kc (Mpa(m)^0.5)
3_56_35A	3	2.6	35	56	18.13625731	11.88625731	0.4754503	64.67	-	92.55
3_56_65A	3	2.6	65	56	18.33246347	12.08246347	0.4832985	59.84	-	88.5
3_56_95A	3	2.6	95	56	18.42672414	12.17672414	0.487069	51.03	-	77.58
3_156_35A	3	2.6	35	156	19.21875	12.96875	0.51875	58.55	-	100.98
3_156_65A	3	2.6	65	156	18.38834556	12.13834556	0.4855338	65.57	-	96.8
3_156_95A	3	2.6	95	156	17.94991687	11.69991687	0.4679967	58.55	-	85.4
3_256_35A	3	2.6	35	256	18.76011327	12.51011327	0.5004045	60.01	-	98.57
3_256_65A	3	2.6	65	256	19.20693928	12.95693928	0.5182776	62.16	-	89.55
3_256_95A	3	2.6	95	256	18.43543729	12.18543729	0.4874175	69.25	-	102.7
6_56_35A	6	5.35	35	56	19.25072644	13.00072644	0.5200291	-	56.67	-
6_56_65A	6	5.35	65	56	19.37474184	13.12474184	0.5249897	-	60.24	-
6_56_95A	6	5.35	95	56	20.52238806	14.27238806	0.5708955	-	57.58	-
6_156_35A	6	5.35	35	156	19.21912833	12.96912833	0.5187651	66.45	-	-
6_156_65A	6	5.35	65	156	18.11321701	11.86321701	0.4745287	-	64.35	-
6_156_95A	6	5.35	95	156	18.324674	12.074674	0.482987	-	61.43	-
6_256_35A	6	5.35	35	256	17.45046977	11.20046977	0.4480188	-	71.97	-
6_256_65A	6	5.35	65	256	18.15368357	11.90368357	0.4761473	-	70.19	-
6_256_95A	6	5.35	95	256	18.46999589	12.21999589	0.4887998	-	69.7	-
9_56_35A	9	8.35	35	56	17.61930199	11.36930199	0.4547721	-	63.17	-
9_56_65A	9	8.35	65	56	16.87188387	10.62188387	0.4248754	-	67.16	-
9_56_95A	9	8.35	95	56	17.82786885	11.57786885	0.4631148	-	62.08	-
9_156_35A	9	8.35	35	156	19.1958649	12.9458649	0.5178346	-	61.05	-
9_156_65A	9	8.35	65	156	17.93981481	11.68981481	0.4675926	-	65.8	-
9_156_95A	9	8.35	95	156	18.32115307	12.07115307	0.4828461	-	59.17	-
9_256_35A	9	8.35	35	256	17.71092454	11.46092454	0.458437	74.88	-	-
9_256_65A	9	8.35	65	256	18.6489899	12.3989899	0.4959596	69.73	-	-
9_256_95A	9	8.35	95	256	18.88341544	12.63341544	0.5053366	61.68	-	-

Appendix C: Surface Roughness & MatLab Program

Surface Roughness Results(Machined)

Specimen (t_h_r)	Ra (µm)	Rq (µm)	Rz (µm)	R_Sk (µm)	R_Ku (µm)
3_h56_35B	0.506	0.705	4.051	2.31	19.31
3_h56_65B	1.904	3.806	17.715	-3.54	22.81
3_h56_95B	0.415	0.644	2.524	1.22	7.40
3_h156_35B	0.340	0.502	2.188	0.37	5.30
3_h156_65B	0.497	0.664	2.785	-0.66	4.64
3_h156_95B	0.394	0.542	1.978	0.58	3.89
3_h256_35B	0.487	0.753	3.263	0.56	9.62
3_h256_65B	0.321	0.444	2.300	0.51	5.15
3_h256_95B	0.349	0.489	1.784	1.06	4.71
6_h56_35B	0.251	0.308	1.463	-0.29	2.71
6_h56_65B	0.214	0.278	1.298	-0.08	3.17
6_h56_95B	0.215	0.277	1.256	0.22	3.61
6_h156_35B	0.207	0.263	1.211	0.02	3.45
6_h156_65B	0.171	0.228	1.232	0.28	3.97
6_h156_95B	0.230	0.294	1.409	0.46	3.22
6_h256_35B	0.245	0.375	2.509	-0.86	17.38
6_h256_65B	0.329	0.480	2.272	1.07	7.43
6_h256_95B	0.378	0.470	2.083	0.37	2.87
9_h56_35B	0.267	0.364	2.250	1.88	15.60
9_h56_65B	0.259	0.332	1.508	0.13	2.92
9_h56_95B	0.353	0.468	1.756	0.65	4.35
9_h156_35B	0.237	0.357	2.042	3.11	26.24
9_h156_65B	0.279	0.343	1.499	-0.34	2.61
9_h156_95B	0.239	0.343	1.851	1.68	12.40
9_h256_35B	0.323	0.475	2.127	0.72	5.04
9_h256_65B	0.352	0.450	2.060	0.44	3.69
9_h256_95B	0.318	0.406	1.701	-0.1	3.04

Surface Roughness Measurements (Machined+HT)

Specimen (t_h_r)	Ra (μm)	Rq (μm)	Rz (μm)	R_Sk (μm)	R_Ku (μm)
3_h56_35A	0.332	0.407	2.011	-0.41	2.99
3_h56_65A	0.668	1.333	5.341	-5.26	41.82
3_h56_95A	0.388	0.471	1.997	-0.46	2.45
3_h156_35A	0.196	0.251	1.621	-0.73	4.04
3_h156_65A	1.564	3.981	17.168	-3.77	25.3
3_h156_95A	0.325	0.402	1.855	-0.14	2.65
3_h256_35A	0.364	0.749	3.479	-6.43	67.8
3_h256_65A	0.612	1.641	6.664	-6.12	52.4
3_h256_95A	0.205	0.269	1.844	-1	5.34
6_h56_35A	0.307	0.391	1.8	-0.64	3.36
6_h56_65A	0.326	0.453	1.777	-1.18	5.05
6_h56_95A	0.21	0.272	1.592	-0.43	3.64
6_h156_35A	0.212	0.289	1.697	-0.22	4.21
6_h156_65A	0.215	0.274	1.522	-0.57	3.34
6_h156_95A	0.262	0.342	1.774	-0.89	3.95
6_h256_35A	0.222	0.281	1.623	-0.3	3.17
6_h256_65A	0.24	0.308	1.929	-0.78	4.28
6_h256_95A	0.267	0.332	1.883	-0.52	3.16
9_h56_35A	0.201	0.261	1.701	-0.54	3.67
9_h56_65A	0.2	0.277	1.801	-1.43	8.25
9_h56_95A	0.197	0.256	1.673	-0.68	4.13
9_h156_35A	0.306	0.409	1.984	-0.7	4.1
9_h156_65A	0.169	0.216	1.398	-0.51	3.66
9_h156_95A	0.169	0.222	1.488	-1.01	7.27
9_h256_35A	0.282	0.364	1.811	-0.57	3.49
9_h256_65A	0.183	0.232	1.566	-0.57	3.76
9_h256_95A	0.203	0.255	1.495	-0.34	3.26

Matlab code for fracture toughness calculations

```
clear all, close all, clc
%% Import Data

PV = load('3mm_256_95A.txt');
%PV = table2array(PVData.PracticeData7_6);
title_ = PV(1,1);
%a = PV(1,2); % final crack length m
PV(1,:) = [];
W = 0.025; % specimen width, m (in)
a = 0.01218; % crack size, m (in)%%FINAL CRACK LENGTH
B = 0.00260; % specimen thickness, m (in), standard is W/2
B_N = B; % unless side grooves are used, then B_N is the tickness
%between the roots
Sig_YS = 975000000; % 0.2% offset yield strength in tension, Pa %276000000
P = PV(:,3); %Given in N
V = PV(:,2); %displacement
P = 1.*(P); % Flip the force vector due to machine output
V = (V+.0055)./1000; % Convert mm to m
% create a polynomial fit of the data for follow-on calcuations
[p,~,mu] = polyfit(V,P,6); %[p,S,mu] = polyfit(x,y,n) n is dof,also returns
mu, which is a two-element vector with centering and scaling values.
%mu(1) is mean(x), and mu(2) is std(x). Using these values, polyfit centers x
at zero and scales it to have unit standard deviation,
V1 = linspace(min(V),max(V),1000); %why set up a new displacement and not use
what was experimentally obtained?
V_lin = linspace(0,max(V),1000);
PVcurve = polyval(p,V1,[],mu);
x = V1;
f2 = @(x) p(1)*x.^6 + p(2)*x.^5 + p(3)*x.^4 + p(4)*x.^3 +  p(5)*x.^2 +
p(6)*x.^1 + p(7); %the p are the coefficients and f is the fit polynomial
based on coefficients

%% Find Slope between Lower (P_l) and Upper (P_u) bound Force points
% Identify P_l point as the start of linear region
P1_P = 163.919; % P lower y coordinate
P1_V = 0.0000234; % P lower x coordinate
% Identify P_u point as the upper end of linear regionr%%%as the 1/3 of the
% test
%P2_P = P(round(6*length(PV)/7));%%FIX THIS LATER TO BE MORE ACCURATE, WHAT
DOES THIS MEAN?
P2_P = 455.8391; % P upper y coordinate
%P2_V = V(round(6*length(PV)/7));
P2_V = 0.0000658; % P upper x coordinate
P_V = [P1_V P2_V];
P_P = [P1_P P2_P];
SlopePV = (P_P(2)-P_P(1))/(P_V(2)-P_V(1)); % slope of test data
y_lin=SlopePV*V_lin;
SlopeP_Q = .95*SlopePV; % slope of P_Q = P_5
%y = SlopeP_Q*(V1-P1_V)+P1_P; % equation of 95% secant line for P_Q; adding,
subtracting by zero
y=SlopeP_Q*V_lin;
%% Find P_Q point at the intersection of PV data and 95% Secant line
%using bisection
%LB0 = P1_V;
%UB0 = max(V);
```

```
%LB = LB0;
%UB = UB0;
%i = 0;
%y3 = 1;
%iter1 = 1;
%iter2 = 2;
%tol = 1e-8;
%while abs(iter1-iter2) > tol && i<100
% iter1 = y3;
% xc = (UB+LB)/2;
% y1 = polyval(p,LB,[],mu)-SlopeP_Q*(LB-P1_V)+P1_P;
% y2 = polyval(p,UB,[],mu)-SlopeP_Q*(UB-P1_V)+P1_P;
% y3 = polyval(p,xc,[],mu)-SlopeP_Q*(xc-P1_V)+P1_P;
% iter2 = y3;
% if sign(y1) == sign(y3)
% LB = xc;
% elseif sign(y2) == sign(y3)
% UB = xc;
% else
% disp(['Something went wrong. i = ' num2str(i)])
% end
% i = i+1;
%end
%P_Q = polyval(p,xc,[],mu); % evaluation of P_Q along the polyfit curve
%% Find P_Q point at the intersection of PV data and 95% Secant line
f1 = @(x) SlopeP_Q.*x; %TRY TO MAKE MORE ACCURATE LATER
i = 1;
y1 = 0;
% while f1(V1(i)) < PVcurve(i) %while f1 from min to max of displacement is
less than the fit curve, loops until f1 isnt less than fit curve
%     y1 = PVcurve(i);
%     xc = V1(i);
%     i = i+1;
% end

%so issues with obtaining xc because condition not being met.

%P_Q = y1;
xq=.00305;
P_Q=3064.3976;
%%
% Identify P_max and corresponding index in V vector
[P_max,V_Index] = max(P);
figure(1)
plot(V,P,'+','LineWidth',0.75,'MarkerEdgeColor','k')
hold on
%plot(V1,PVcurve,'b','LineWidth',1.5)
% y2=(3118716*V1+.0695)*.95;
% plot(V1,y2,'--b')
% hold on
% plot(P_V,P_P,'*r','LineWidth',1.5)
% hold on
% plot(P_V,P_P,'-r','LineWidth',1.5)
% hold on
plot(V_lin,y_lin,'-b','LineWidth',1.5)
hold on
plot(V_lin,y,'--m','LineWidth',1.5)
hold on
```

```
% plot(xq,P_Q,'om','LineWidth',1.5)
% hold on
plot(V(V_Index),P_max,'ok','LineWidth',1.5)
hold on
%plot(V1, 2.2166e10^6*V1)

grid on
grid minor
legend('PV Data','Linear Region',...
    '95% Secant (P/V)','P_M_a_x','location','best', 'FontSize', 14) %'PV
polyfit',
xlabel('CMOD (m)',  'FontSize', 15)
ylabel('Load (N)','FontSize', 15)
xlim([0 .001])
ylim([0 15000])
specimen = "Specimen";
%title_ = sprintf('%d',title_);
%title(specimen + ' ' + title_);
title('Load vs. CMOD, 3mm-256-95A', 'FontSize', 16);

%% Test 1 for data validity
test1 = P_max/P_Q
if test1 > 1.1
 test1text = ['P_max/P_Q = ', num2str(test1),...
 ', P_max/P_Q > 1.10, test is not valid, must use elastic plastic fracture
toughness'];
 disp(test1text)
else
 disp('Test 1 is valid')
end
%% Calculation of K_Q
% depends on specimen type
% The following is for Compact Specimen CT
aW = a/W;
W_minus_a = W-a
F_aW = (2+aW)*(0.886+(4.64*aW)-(13.32*aW^2)+(14.72*aW^3)-...
(5.6*aW^4))/((1-aW)^(3/2));
K_Q = (P_Q/(sqrt(B*B_N)*sqrt(W)))*F_aW;
% Test 2 for data validity
test2 = 2.5*(K_Q/Sig_YS)^2
if test2 < W_minus_a
 K_Ic = K_Q;
 test2text1 = ['K_Ic = ', num2str(K_Ic/1000000),' MPa*sqrt(m)'];
 disp('Test 2 is valid')
 disp(test2text1)
else
    test2text2 = ['K_Q = ', num2str(K_Q/1000000),' MPa*sqrt(m)'];
    disp('Test 2 is invalid');
    disp(test2text2)
end
% disp('Kq')
% disp(K_Q)


%% calculate Kq/Kic
```